



## Effect of coordination surroundings of isolated metal sites on electrocatalytic performances

Jingqi Guan

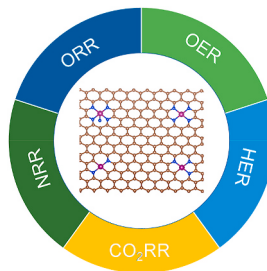
Institute of Physical Chemistry, College of Chemistry, Jilin University, Changchun, 130012, PR China



### HIGHLIGHTS

- Effect of the coordinated environment of SACs on electrochemical performances is discussed.
- The detailed electron structure of isolated metal sites is provided.
- Applications of SACs in HER, OER, ORR, CO<sub>2</sub>RR, and NRR are commented.
- The structure-function relationships of SACs are documented.
- The technical challenges and prospects for the progress of SACs are suggested.

### GRAPHICAL ABSTRACT



### ARTICLE INFO

#### Keywords:

Single-atom catalyst  
Hydrogen evolution reaction  
Oxygen reduction reaction  
CO<sub>2</sub> reduction reaction  
Nitrogen reduction reaction

### ABSTRACT

Due to possessing outstanding catalytic performance and drastically enriching our cognition of reaction mechanisms, single-atom catalysts (SACs) are burgeoning as a novel frontier research field in electrocatalysis. The catalytic performances of SACs are significantly influenced by the electronic and geometric structures of isolated metal sites. In this Review, we focus on discussing the effect of the coordinated surroundings of isolated metal sites on electrochemical performances. How to disclose the detailed electron structure and coordinated environment of isolated metal sites is provided. Several important electrochemical applications (i.e. hydrogen evolution reaction (HER), oxygen evolution reaction (OER), oxygen reduction reaction (ORR), CO<sub>2</sub> reduction reaction (CO<sub>2</sub>RR), and nitrogen reduction reaction (NRR)) and the structure-function relationships are documented. In addition, the technical challenges and prospects for the progress of high-performance SACs are suggested.

### 1. Introduction

Different from conventional metal-based nanocomposites, single-atom catalysts (SACs) possess distinctive traits, such as unsaturated coordination configuration, quantum size effect, and powerful atom-support interaction, which make them a wide range of applications in fine chemicals, energy conversion and storage, environmental remediation, biomedicine, and molecular sensing [1]. Owing to possessing high

catalytic performance, SACs have been widely studied in many important electrochemical redox reactions, such as hydrogen evolution reaction (HER), oxygen evolution reaction (OER), oxygen reduction reaction (ORR), CO<sub>2</sub> reduction reaction (CO<sub>2</sub>RR), and nitrogen reduction reaction (NRR) [2]. The electrochemical performances of SACs are mainly related to the following three aspects: 1) the kind of metal centers, 2) the kind and number of coordinated atoms to the metal center, and 3) the surroundings of the metal-ligands moieties. Generally speaking, the

E-mail address: [guanjq@jlu.edu.cn](mailto:guanjq@jlu.edu.cn).

metal sites play a key role for a specific reaction. The electronic structure of metal site would be regulated by coordinated nonmetal atoms and they would synergistically catalyze a reaction with the metal site in some cases. Therefore, the electrocatalytic performance will be directly affected by different coordination atoms and coordination numbers (Fig. 1a–c). For example, iron oxide and cobalt oxide showed poor ORR activity, while single-atom Fe–N–C and Co–N–C catalysts demonstrated superior ORR performance, indicating that N-coordination is more suitable than O-coordination to the Fe/Co sites for the ORR [3]. For

Fe–N–C catalysts, the Fe–N<sub>4</sub> configuration showed higher OER activity than Fe–N, Fe–N<sub>2</sub>, and Fe–N<sub>3</sub> structures due to lower reaction energy barrier on the Fe–N<sub>4</sub> sites [4]. Additionally, the surroundings of M–N–C moiety also influence the catalytic performance. For instance, Jiang et al. found that the edge-anchored NiN<sub>3</sub> sites exhibited higher electrocatalytic activity than the in-plane NiN<sub>3</sub> and NiN<sub>4</sub> sites for CO<sub>2</sub>RR [5].

Since the electronegativity of oxygen atoms is larger than that of nitrogen atoms, the electron density of metal centers coordinated with oxygen ligands is lower than that coordinated with the same number of

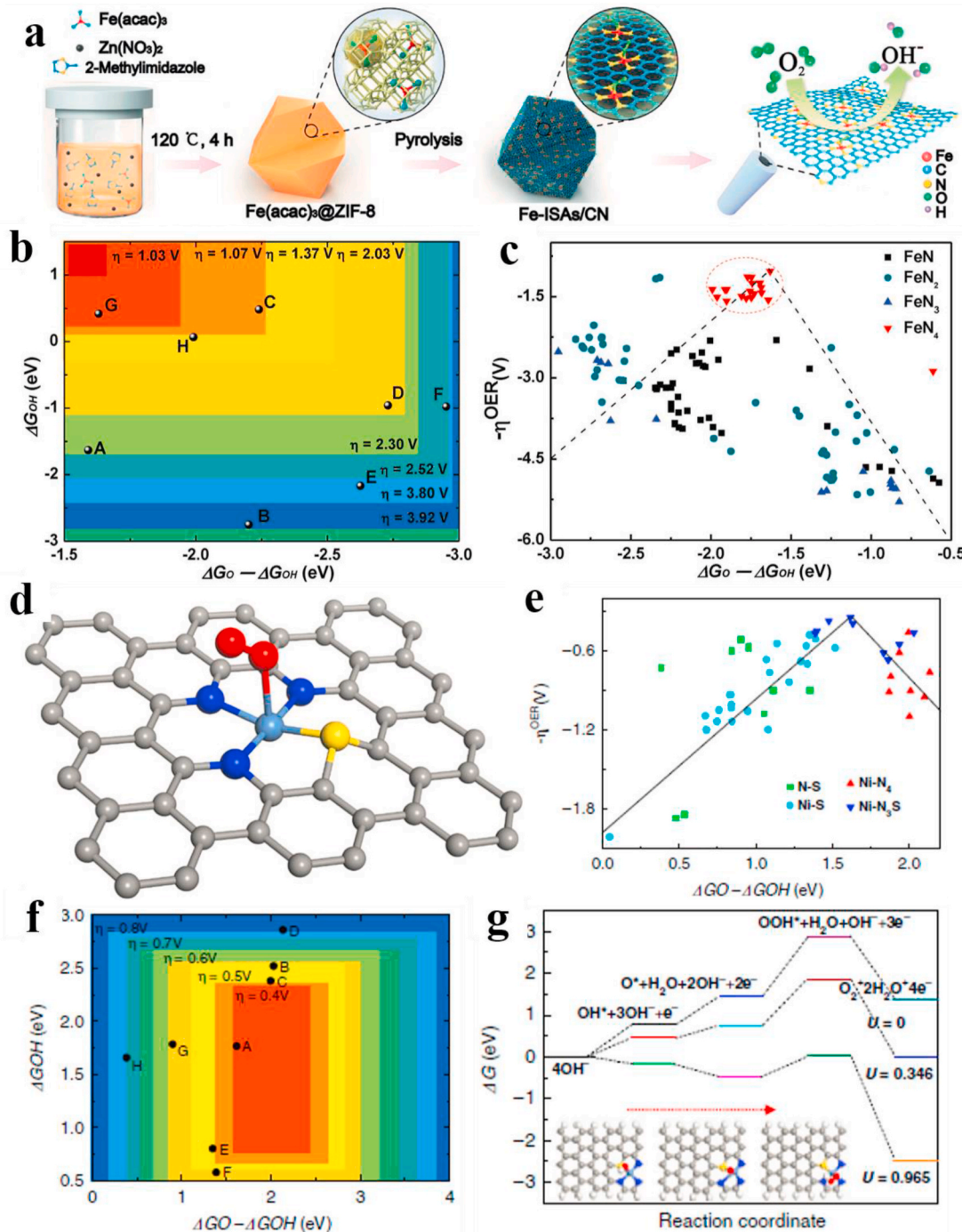


**Fig. 1.** (a) Schematic illustration for the synthesis of single-atom Fe–N–C catalysts. Reproduced with permission [3]. Copyright 2017 Wiley-VCH. (b) Schematic OER volcano plot. (c) Schematic free energy profile. Reproduced with permission [4]. Copyright 2017 Wiley-VCH. (d) Schematic structural model for S|NiN<sub>x</sub>|PC. The steel blue, blue, yellow, gray, and red spheres represent Ni, N, S, C, and O atoms, respectively. (e) OER volcano plot. (f) Adsorption free energy. (g) Schematic free-energy profile for OER on Ni–N<sub>3</sub>S. Reproduced with permission [8]. Copyright 2019 Nature Publishing Group. (For interpretation of the references to colour in this figure legend, the reader is referred to the Web version of this article.)

nitrogen ligands. Due to increased electron density around metal centers, the M–N coordination shows more appropriate adsorption/desorption ability of intermediates than the M–O coordination for many electrocatalytic redox reactions. As is well-known, too strong or too weak adsorption/desorption of intermediates would lead to higher energy barriers and larger overpotentials. For example, Guan et al. found that  $\text{MnN}_3\text{-G}$  and  $\text{MnO}_3\text{-G}$  (G: graphene) sites bonded the  $\text{OH}^*$  intermediate far more strongly than the  $\text{MnN}_4\text{-G}$  site, resulting in higher OER overpotentials on the two sites [6]. In addition, the coordination number of ligands would affect the electronic structure of metal sites due to some participating in coordination bonds and others taking part in chemical bonds. It is generally accepted that the  $\text{M-N}_4\text{C}_x$  ( $\text{M} = \text{Fe, Co, and Mn}$ ) configuration favors a  $4\text{e}^-$  ORR [7].

When two or more kinds of ligands were introduced, the distribution of electron density should be asymmetrical and the hybridization states should be modified due to their different electronegativities, which might be beneficial to increase the adsorption of reactants, thus improving catalytic activity [8,9]. For instance, atomic nickel, nitrogen, and sulfur co-doped porous carbon nanosheets exhibited higher OER activity than S-free samples due to lower reaction energy barrier on the  $\text{Ni-N}_3\text{S}$  site (Fig. 1d–g) [8]. It should be pointed out that it is very difficult to predict optimal structures of isolated metal sites with different ligands for a specific reaction in advance. However, SACs with dual-metal sites might be a good choice for electrocatalytic redox reactions involving multielectron transfer mechanism because the cooperation between different metal sites would lower the reaction barrier [10,11]. In this review, we describe detailedly the effect of coordination environment in SACs on electrochemical HER, OER, ORR,  $\text{CO}_2\text{RR}$ , and NRR.

## 2. Fabrication and identification of single-atom sites

### 2.1. Synthetic strategies

Due to unsaturated coordination and high surface energy of single atoms, migration and agglomeration of single metal ions to form clusters or nanoparticles happens easily [12]. Therefore, confining the isolated metal ions and keeping them from contacting each other is crucial for the synthesis of high-quality SACs. To achieve high dispersion of metal sites, the interactions between metal ions and support should be emphatically concerned. Generally speaking, suitable supports should possess several characteristics: i) high specific surface area to support enough metal species, ii) abundant O/N/S-containing functional groups or vacancies/defects to anchor or trap metal species, iii) good stability under specific reaction conditions.

Up to now, a number of synthetic methods have been developed to fabricate SACs, which can be categorized into low-temperature, middle-temperature and high-temperature strategies. Low-temperature synthetic strategies are usually carried out at temperatures less than  $80^\circ\text{C}$ , which include coprecipitation, impregnation, photochemical reduction, electrodeposition, ball milling method and so on. In 2011, Zhang et al. supported atomically dispersed Pt onto  $\text{FeO}_x$  nanocrystals by a coprecipitation method, which showed high activity for CO oxidation [13]. Luo et al. anchored single-atom Ni onto  $\text{MoS}_2$  supported by multichannel carbon matrix by a wet-impregnation method, which exhibited enhanced HER performance [14]. Zheng et al. adopted a photochemical reduction strategy to immobilize isolated single Pd atoms onto the surface of  $\text{TiO}_2$ , exhibiting high catalytic activity for hydrogenation of aldehydes [15]. Luo et al. fabricated single Pt atoms onto CoP-based nanotubes supported on a Ni foam, showing 3 times of Pt mass activity higher than that of Pt/C in neutral phosphate buffer solutions [16]. Bao et al. fabricated  $\text{FeN}_4$  sites onto graphene matrix by ball milling method, which demonstrated high catalytic activity for the oxidation of benzene to phenol at room temperature [17].

Middle-temperature synthetic strategies are usually performed at temperatures ranged from  $80$  to  $500^\circ\text{C}$ , which include mainly

hydrothermal synthesis, atomic layer deposition (ALD), and chemical vapor deposition (CVD) technique. Huang et al. anchored isolated Ni sites onto  $1\text{T-MoS}_2$  by a hydrothermal synthesis method, showing enhanced HER activity [18]. Wei et al. synthesized a monolayer Co– $\text{MoS}_2$  through CVD method, showing superior HER activity [19]. ALD is a powerful technique to obtain atomically dispersed catalysts [20]. The self-limiting reactions in ALD process favor controlling the size or thickness of the deposited species at the atomic level.

High-temperature synthetic strategies are those that operate at temperatures above  $500^\circ\text{C}$ , which include mainly pyrolysis method, which is widely adopted for fabricating carbon-based SACs. For high-temperature pyrolysis, specific precursors containing metal species, and N/S and C sources are annealed at appropriate temperature (e.g.  $500$ – $1000^\circ\text{C}$ ) under a non-oxidizing atmosphere (i.e.  $\text{N}_2$ , Ar, or  $\text{NH}_3$ ). The precursors mainly contain: 1) metal-salt-containing mixtures, 2) metal organic frameworks (MOFs), and 3) template-containing mixtures (i.e. silica-based or hydroxide-based hard template) [21]. The catalysts synthesized by pyrolysis method usually contain metal nanoparticles, which should be removed by acid leaching. To prevent metal agglomeration, one of the most efficient strategies is using Zn-based MOFs as the precursors. Under high-temperature annealing conditions ( $> 900^\circ\text{C}$ ), the  $\text{Zn}^{2+}$  ions can be reduced by the carbon source and the generated metal Zn will volatilize since its boiling point is  $907^\circ\text{C}$ . The desired metal ions can be well isolated by abundant  $\text{Zn}^{2+}$  ions, and SACs with various metal sites (e.g. Cr, Mn, Fe, Co, Ni, Cu, Ru, and Ir) have been obtained after the removal of Zn species [1,22].

Each synthetic method has its advantages and disadvantages. Low-temperature synthesis (e.g. coprecipitation, impregnation, photochemical reduction, and electrodeposition) is easy to operate, which can be applied in many laboratories and factories. However, for rigid carriers, the doped metal species are usually supported on the surfaces, which can hardly be incorporated into the lattices since large energy barriers need be overcome. The isolated metal atoms in the obtained SACs might be migrated and reunited or leached under harsh reaction conditions. For middle/high-temperature synthesis, some special devices are needed, and some of them (e.g. ALD apparatus) are expensive. Relatively high temperatures can provide energy to overcome reaction barriers for incorporating metal ions into the lattices of supports and forming metal-ligands coordination.

### 2.2. Characterization of SACs

Since the spatial resolution and energy resolution on an advanced transmission electron microscopy (TEM) can be as high as  $0.05\text{ nm}$  and  $7\text{ meV}$ , respectively, isolated metal atoms can be intuitively detected by aberration corrected scanning transmission electron microscopy (AC-STEM) [23]. If the atomic number of supported metal atoms is larger than those of supports, the bright dots in the high-angle annular dark-field scanning transmission electron microscopy (HAADF-STEM) should be due to the supported metal atoms. For instance, for M-N-C materials, the isolated metal atoms can be well identified in the HAADF-STEM image because the atomic number of the isolated metal atoms is much higher than those of carbon and nitrogen atoms, and the bright dots should be ascribed to the isolated metal atoms. However, if the atomic number of doped metals is close to that in the support or doping two or more different metals into the support, them cannot be directly differentiated. On these occasions, we can magnify Z-contrast HAADF-STEM image to compare the signal intensity along the direction of a selected line. For example, Song and co-workers used this method to identify atomic dual-metal Fe–Ni on graphitic carbon nitride nanosheets [24]. The dispersion of isolated metal atoms can be analyzed by energy dispersive X-ray spectroscopy (EDX) or electron energy loss spectroscopy (EELS). For analysis of heavy elements, EDX is sensitive, while EELS is more sensitive for distinguishing light elements (e.g. C, O, N). In addition, catalytic reactions happened within  $1\text{ ms}$  can be monitored by in-situ TEM, which can provide useful information for revealing reaction

mechanisms on isolated metal sites [25–27].

The valence state of metal species can be analyzed by X-ray photoelectron spectroscopy (XPS), electron paramagnetic resonance (EPR) spectroscopy, and X-ray absorption near edge structure (XANES) spectroscopy. XPS is a powerful and easily available technique to reveal the chemical valence of surface metal species, while EPR and XANES techniques are sensitive to detect the valence state of bulk metal species. Moreover, different valence states of a metal element with paramagnetism in the catalyst can be separately detected by EPR. However, for non-paramagnetic metals, there is no EPR signal. For XANES, standard samples are required to compare the position of white lines for identifying the chemical valence of the metal to be measured. For example, to obtain the chemical valence of Fe in Fe–N–C materials, the white lines in XANES spectra of metal Fe and ultrapure  $\text{Fe}_2\text{O}_3$  are usually needed to compare with those of Fe–N–C to reveal the average valence state of Fe in the samples.

The local structural information of metal sites can be disclosed by extended X-ray absorption fine structure (EXAFS) spectroscopy and complementary theoretical simulations. By fitting EXAFS spectra, the average metal coordination environment (e.g. bond length and coordination number) consisting of different shells of atoms (e.g. O, N and C) in the support can be obtained [6]. In typical EXAFS spectra of SACs, the peak due to M–M path is absent. In addition, scanning electron microscope (SEM), X-ray diffraction (XRD), Fourier transform infrared spectroscopy (FTIR), Raman spectroscopy, and nuclear magnetic resonance (NMR) can offer additional information for the characterization of SACs. Moreover, for Fe-based SACs, Mössbauer spectrum is an ingenious and potent technique to analyze the structure of Fe sites [28].

### 3. Electrode–electrolyte interfaces and electrode potential effects

Electrocatalytic reactions happen at electrode–electrolyte interfaces, where reaction intermediates are adsorbed and converted into target products. In alkaline media, the catalytic activity is influenced by covalent interactions between adsorbates and catalyst surfaces and non-covalent interactions between hydrated alkali metal cations and adsorbed OH species [29]. The ORR activity decreases as the hydration energy of the cations in the electrolyte increases and the trend of ORR activity in alkaline media decreases as follows:  $\text{Cs}^+ > \text{K}^+ > \text{Na}^+ \gg \text{Li}^+$ . Huang and Chen found that as noncovalent interactions, electrical double-layer (EDL) effects can regulate covalent interactions by influencing the interfacial solvent reorganization energy ( $\lambda$ ) and transfer coefficient [30, 31]. By theoretical studies, they proposed that high-performance catalysts should possess a d band crossing the Fermi level.

The optimum binding energy might shift by changing the driving force [32]. For example, Shao and co-workers found that a Rh/Si catalyst showed lower activity than Pt/C for HER at low overpotentials but became more active at higher overpotentials [33]. Xu et al. found that the HER activity of Pd/ $\text{Fe}_3\text{O}_4$  core/shell NPs significantly increased with larger overpotentials due to the balance between water dissociation and hydrogen formation [34]. Huang and co-workers constructed a potential-dependent volcano plot for ORR using a mean-field theoretical model. They found that the electrode potential can influence the intrinsic activity of an electrocatalyst and change the volcano peak.

### 4. Effect of coordination surroundings in SACs for electrocatalytic applications

#### 4.1. M–N coordination

The Pauling electronegativity of N is 3.066, which is higher than that of C (2.544) and S (2.589), but lower than that of O (3.61) [35]. In addition, the electronegativity of transition metals is relatively low. For instance, the electronegativity of Mn, Fe, Co, Ni, Cu, Ru, Rh, Pd, Ir, and Pt is 1.75, 1.80, 1.84, 1.88, 1.85, 1.54, 1.56, 1.58, 1.68, and 1.72,

respectively. Therefore, the d-band electron structure of transition metals can be modulated by changing the coordinated atoms and numbers. Compared with O-coordination, the outer layer valence electron density of metal ions with N-coordination is higher. An upshift in d-band center will increase the energy level of antibonding d-orbitals and decrease their electron occupancy, resulting in a stronger binding. The reverse is also true. For M–N–C electrocatalysts, the current research focuses mainly on two aspects: (i) enhancing the intrinsic activity of active sites. For an ideal electrocatalyst, the active sites should possess moderate adsorption strength for reaction intermediates according to the Sabatier principle [36]. The adsorption behavior of active sites is principally regulated by the electronic properties. Reasonably modulating the electronic structure of isolated metal atoms is an effective approach to improve the intrinsic activity of SACs [37]. To achieve this goal, we should synthesize atomic M–N–C catalysts with highly purified and uniformed M–N<sub>x</sub> configurations. (ii) Increasing the mass density of M–N<sub>x</sub> moieties. It is preferred to select precursors with confined metal centers and abundant nitrogen coordination to synthesize M–N–C catalysts with high density of M–N<sub>x</sub> sites.

##### 4.1.1. M–N<sub>5</sub> configuration

**4.1.1.1. Fe–N<sub>5</sub> configuration.** In the last few years, SACs have gained a lively interest and increasing attention. Thereinto, the nitrogen coordination strategy is widely adopted for stabilizing the isolated metal atoms due to stable M–N bonds [38]. Due to electron donating effect of nitrogen atoms, the electronic density of the metal sites is much higher than those coordinated with oxygen atoms, which makes them active in many redox reactions, e.g. HER, OER, ORR,  $\text{CO}_2\text{RR}$ , and NRR [39–44]. It is well-known that atomically dispersed Fe–N–C materials exhibited superior ORR activity in alkaline media [45]. For instance, Shen et al. synthesized an atomic Fe–N–C catalyst (Fe–N–C900), which exhibited bifunctional OER and ORR performance with  $\Delta E (E_f = 10 - E_{1/2})$  of 0.70 V in alkaline electrolytes and 0.86 V in acidic electrolytes [46]. By EXAFS analysis, they identified that the main structure of Fe species for the Fe–N–C900 catalyst was Fe–N<sub>5</sub>. Chen and coworkers anchored isolated Fe atoms onto N-doped carbon materials (Fe SAC/N–C) by pyrolysis and acid leaching strategy, which displayed superior ORR activity with a  $E_{1/2}$  of 0.89 V vs RHE [47]. DFT simulations uncovered that the Fe–4pN-py sited displayed higher ORR activity than Fe–4pN and Fe–4pN-OH since the fifth pyridinic nitrogen atom on the Fe-p4N can weaken the further binding of oxygen-containing intermediates.

**4.1.1.2. W–N<sub>5</sub> configuration.** Pristine tungsten metal binds oxygen atoms too strongly, resulting in poor ORR activity. However, the d-band electron structure of W atoms can be modulated by carbonizing or nitriding treatment, and the formed WC<sub>x</sub> and WN<sub>x</sub> possessed desired density of states near the Fermi level, favoring the ORR electrocatalysis [48,49]. By regulating W–N coordination numbers, Zhao et al. obtained an atomic W–N–C catalyst, which demonstrated superior ORR activity with  $E_{1/2}$  of 0.88 V vs. RHE in 0.1 M KOH [50]. Since the third step of the ORR on W–N<sub>3</sub> was endothermic, the ORR on the W–N<sub>3</sub> site is a  $2e^-$  route with the formation of H<sub>2</sub>O<sub>2</sub>. Compared with the energy barrier on the W–N<sub>4</sub> site (0.58 eV) and Pt catalyst (0.45 eV), the W–N<sub>5</sub> site showed lowered energy barrier (0.38 eV), suggesting that it should be the active site for ORR. The Bader charge analysis demonstrated that charges of 0.79, 0.69, 0.74, 0.55, 0.59, and 0.58 electrons were transferred to OH\* for the metallic W, WN, WC, WN<sub>3</sub>, WN<sub>4</sub>, and WN<sub>5</sub>, respectively, indicating N-coordination effect on the electronegativity of metal ions.

##### 4.1.2. M–N<sub>4</sub> configuration

**4.1.2.1. Co–N<sub>4</sub> configuration.** Due to good redox ability of cobalt ions, Co-based catalysts showed extensive applications in heterogeneous catalysis [12,51,52]. The d-band electron structure of Co atoms can be

regulated by nitriding treatment, and the obtained  $\text{CoN}_x$  structures showed higher catalytic activities than  $\text{Co}-\text{O}$  coordination configuration in many reduction reactions. For instance, theoretical calculation results predicted that the  $\text{Co}-\text{N}_4\text{C}_4$  moiety shows higher HER activity than other  $\text{M}-\text{N}_4\text{C}_4$  moieties and other  $\text{Co}-\text{N}_x\text{C}_y$  moieties [53]. From Fig. 2a-f, the Co-SAC showed excellent HER performance. Theoretical calculations revealed that the Co-SAC exhibited low Gibbs free energy ( $\Delta G_{\text{H}^*}$ ) of 0.13 eV and higher HER activity than other SACs, e.g. Mn-SAC, Fe-SAC, Ni-SAC, Pd-SAC, Re-SAC, Mo-SAC, Ti-SAC, W-SAC, and Ta-SAC (Fig. 2j-g). Too weak or too strong interactions between the active sites and adsorbed hydrogen would lead to high overpotentials for HER [54]. Combining XAS analysis, experimental results, and theoretical calculations, they disclosed the structure of HER active site, which is one cobalt atom coordinated to four nitrogen atoms in graphene. In addition,  $\text{Co}-\text{N}_4$  embedded onto porous carbon materials demonstrated high HER activity with turnover frequency of  $3.8 \text{ s}^{-1}$  at an overpotential of 200 mV [40]. Compared with high  $|\Delta G_{\text{H}^*}|$  (0.20 eV) value of Co nanoparticles, the Co-SAC catalyst showed much smaller  $\Delta G_{\text{H}^*}$  (0.08 eV) with favorable hydrogen adsorption-desorption property, thus promoting H adsorption and facilitating H-H formation.

$\text{Co}-\text{N}_4$  embedded onto porous carbon materials not only exhibited excellent HER performance, but also displayed superior ORR activity [40]. As early as in 1964 [55], Jasinski reported that cobalt phthalocyanine with  $\text{Co}-\text{N}_4$  site exhibited better ORR performance than copper, nickel and platinum phthalocyanines in alkaline media. In 2008, Wu et al. found that polyaniline-derived FeCo-based catalysts showed onset ( $E_{\text{onset}}$ ) and half-wave potential ( $E_{1/2}$ ) of 0.9 and 0.77 V in 0.5 M  $\text{H}_2\text{SO}_4$  for ORR, respectively [56]. In 2009, Jaouen et al. revealed that Fe/ $\text{Co}-\text{N}-\text{C}$  catalysts obtained by heat-treatment method exhibited good ORR activity and the  $\text{Co}-\text{N}-\text{C}$  was more stable than the  $\text{Fe}-\text{N}-\text{C}$  under PEMFC operating condition [57]. In 2011, Liu et al. investigated the ORR performance on  $\text{Co}-\text{N}-\text{C}$  catalysts derived from a cobalt imidazolate framework under different pyrolysis temperatures and found that the optimal pyrolysis temperature should be ca. 750 °C [58]. They proposed  $\text{Co}-\text{N}_4$  sites as the active center for ORR.

With the help of AC-STEM and XAS, the structure of active sites in SACs has been disclosed, and the investigation of SACs in ORR has been greatly developed in recent few years. Most single-atom  $\text{Co}-\text{N}-\text{C}$  catalysts were fabricated by pyrolysis method. For instance, a Co-SAC

catalyst can be synthesized by pyrolyzing the mixture of cobalt salt, silica colloidal crystal, triblock copolymer Pluronic F127, resol, dicyandiamide, and vitamin, and subsequent HF leaching [40]. The Co-SAC exhibited a positive half-wave potential ( $E_{1/2}$ ) of 0.892 V vs. RHE in alkaline medium. Density functional theory (DFT) simulations uncovered that the Co-SAC showed lower theoretical overpotential for ORR than Co nanoparticles supported on carbon. To change macroscopic morphology of catalysts, electrospinning technique was frequently used for the fabrication of nanowires [59]. By carbonization, a Co-SAC catalyst ( $\text{Co}@\text{MCM}$ ) can be obtained. The  $\text{Co}@\text{MCM}$  showed a smaller ORR barrier of 3.36 eV than MCM (4.5 eV), on which the reduction of  $\text{O}_2^*$  to  $\text{OOH}^*$  was the rate-determining step. Single-atom  $\text{Co}-\text{N}-\text{C}$  catalysts with high Co content can be directly obtained by pyrolysis of bimetallic Zn/Co metal-organic frameworks [60]. The coordination surroundings of Co atoms could be tuned by changing pyrolysis temperature.  $\text{Co}-\text{N}_4$  and  $\text{Co}-\text{N}_2$  was mainly formed at 800 and 900 °C, respectively. DFT simulations revealed that the  $\text{Co}-\text{N}_2$  site showed stronger interaction with  $\text{H}_2\text{O}_2$  than the  $\text{Co}-\text{N}_4$  site. Moreover, several research groups prepared Co-SACs by pyrolyzing MOF precursors for efficient ORR in recent years. Pennycook et al. obtained porous  $\text{Co}-\text{N}-\text{C}$  catalysts by pyrolyzing a Co-MOF supported on carbon cloth and subsequently acid leaching, which exhibited good cycling stability as the air cathode in a solid-state Zn-air battery [61]. Deng et al. isolated cobalt species by modulating the Zn content in bimetallic Zn/Co zeolitic imidazole frameworks and obtained nanoparticles, clusters, and single atoms of Co species on N-doped porous carbon [62]. They found that atomic  $\text{Co}-\text{N}-\text{C}$  showed better ORR activity than Co-based nanoparticles and clusters. Wu et al. found that the pressure difference between inside and outside of MOFs promoted the breakage of carbon layers and generation of mesopores [63]. They transformed 3D MOFs into 3D graphene frameworks by a negative pressure pyrolysis method, which exhibited a positive  $E_{1/2}$  of 0.901 V vs. RHE in 0.1 M KOH due to abundant accessible  $\text{Co}-\text{N}_4$  sites.

Although Co-SACs showed excellent ORR activity in basic media, they exhibited moderate ORR performance in acidic media [41,64]. To enhance the acidic ORR activity of Co-SACs, a common strategy is aggrandizing the density of active cobalt sites. For instance, Wu et al. found that the  $E_{1/2}$  can be positively shifted by increasing the Co content from 0.07 at% for 1Co-NC-1100 to 0.34 at% for 20Co-NC-1100 [65].

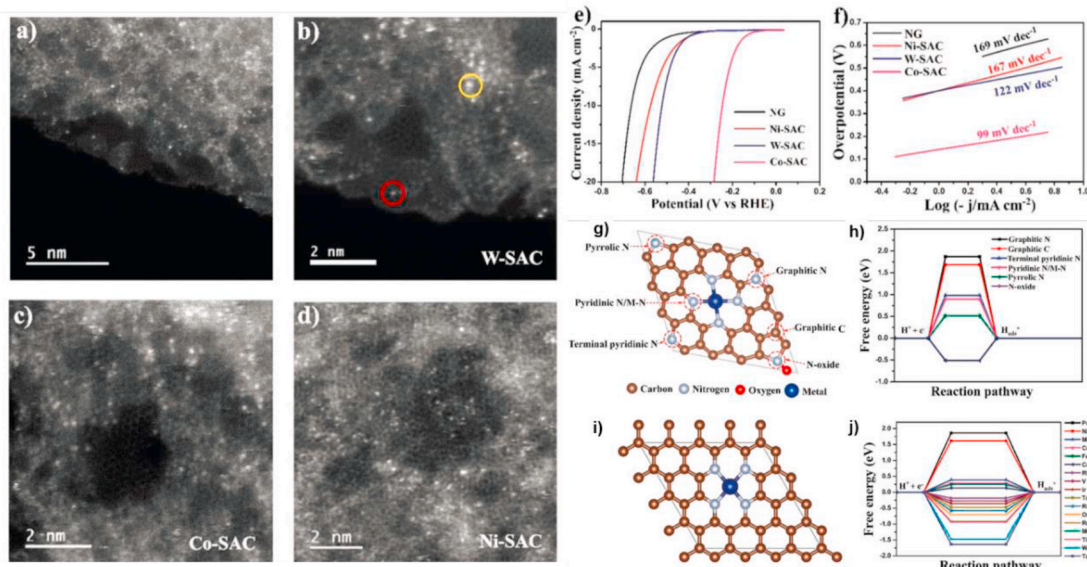


**Fig. 2.** (a-b) STEM images of W-SAC, (c) STEM image of Co-SAC, and (d) STEM image of Ni-SAC. (e) LSV curves of SACs in 0.5 M  $\text{H}_2\text{SO}_4$ . (f) Corresponding Tafel plots. (g) Nonmetallic sites for hydrogen adsorption in the metal functionalized N-doped graphene sheet. (h) Gibbs free energies ( $\Delta G_{\text{H}^*}$ ). (i) Metal active site coordinated with four nitrogen atoms in graphene sheet. (j) Gibbs free energy diagram for hydrogen adsorption reaction (Volmer reaction). Reproduced with permission [53]. Copyright 2019 Wiley-VCH.

Soon afterwards, they synthesized a Co–N–C@F127 with 1.0 at% Co content by a thermal treatment of Co-ZIF-8 precursor, which exhibited a positive  $E_{1/2}$  of 0.84 V vs. RHE in acidic media [66]. The fuel cell assembled with Co–N–C@F127 as the cathode showed a power density of 0.87 W cm<sup>-2</sup>. Theoretical calculations predicted that higher activation energy should be overcome on the CoN<sub>4</sub> site than that on the CoN<sub>2+2</sub> site for the OOH dissociation reaction, suggesting that CoN<sub>2+2</sub> can more efficiently catalyze the ORR via a 4e<sup>-</sup> pathway. In addition, Li

and coworkers fabricated a Co–N<sub>4</sub>/C catalyst with Co content of 2.2 wt %, which showed an onset potential of 0.68 V vs. RHE in neutral media for 4e<sup>-</sup> ORR, on which the rate-determining step was the formation of bound O<sub>2</sub><sup>\*</sup> [67]. Very recently, Shao et al. revealed the degradation mechanisms of Co–N–C catalysts during ORR [68]. Firstly, they prepared a single-atom Co–N–C catalyst by pyrolysis of Co(mIm)<sub>4</sub>@ZIF-8 precursor, which exhibited excellent ORR performance with positive  $E_{1/2}$  of 0.82 V in 0.5 M H<sub>2</sub>SO<sub>4</sub> and hydrogen fuel cell performance with

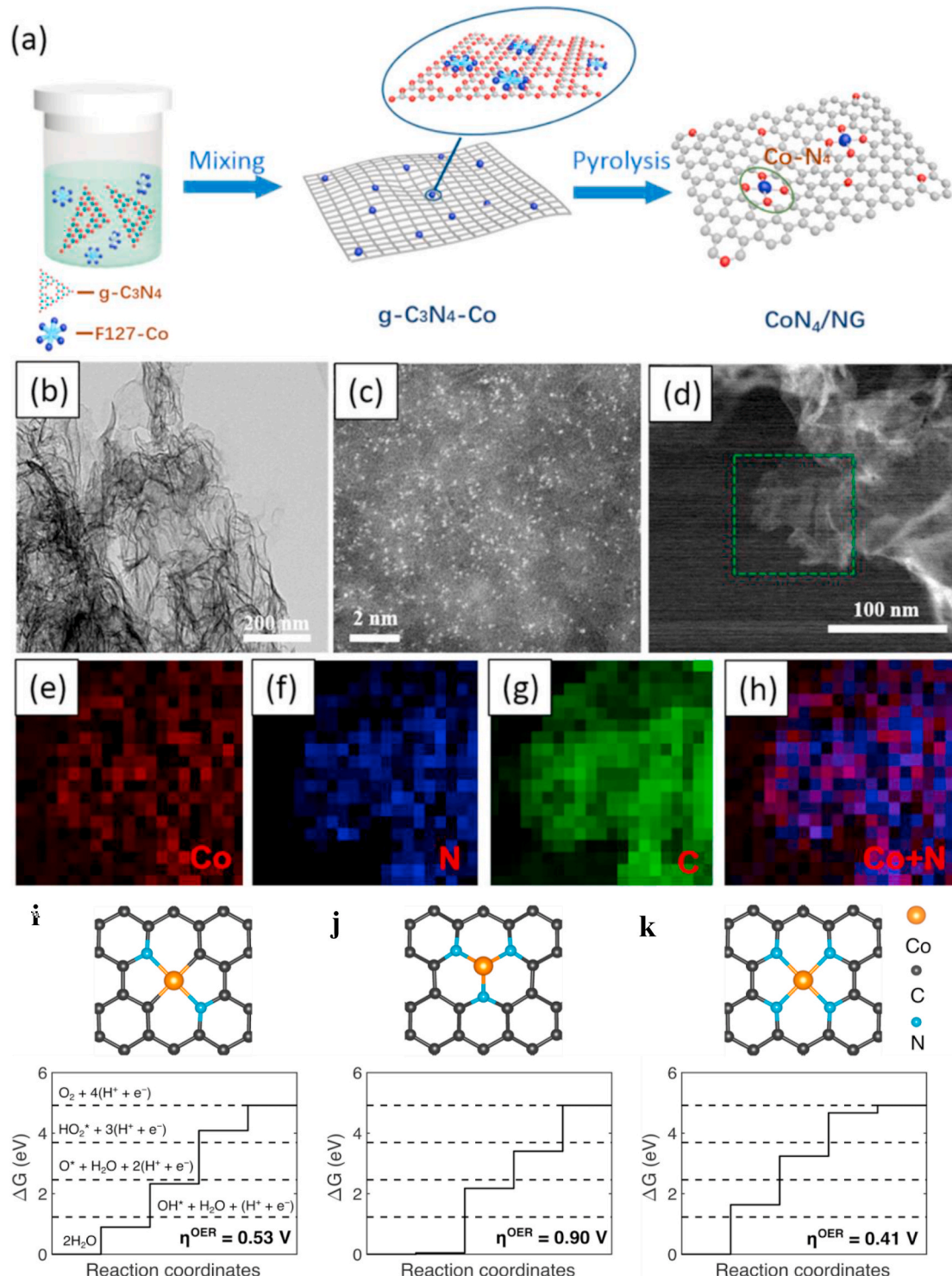


**Fig. 3.** (a) Schematic illustration of the synthesis of single-atom CoN<sub>4</sub>/NG catalyst. (b) TEM image. (c) HAADF STEM image. (d) TEM image. (e–h) EELS mapping of cobalt, nitrogen, carbon and superimposed cobalt and nitrogen for the CoN<sub>4</sub>/NG sample. Reproduced with permission [70]. Copyright 2018 Elsevier. Free energy diagram for the OER on (i) Co–N<sub>2</sub>C<sub>2</sub>, (j) Co–N<sub>3</sub>, and (k) Co–N<sub>4</sub> sites. Reproduced with permission [72]. Copyright 2019 Royal Society of Chemistry.

peak power density of  $0.64 \text{ W cm}^{-2}$ . Then, they used XAS, Mössbauer spectroscopy, pore distribution analysis, and theoretical simulations to explore the structure of active sites and demetallation process. They found that Co–N–C exhibited higher resistance to demetallation than Fe–N–C due to lower activity of Co sites for Fenton reactions. Liu et al. found that a Co SAC was highly active for the  $2 e^-$  ORR pathway, on which the kinetic current reached  $1 \text{ mA cm}^{-2}_{\text{disk}}$  at  $0.6 \text{ V}$  vs. RHE in  $0.1 \text{ M HClO}_4$  with  $\text{H}_2\text{O}_2$  faraday efficiency larger than 90% [69]. The  $\text{CoN}_4$  site was proposed to be the active center, on which the rate-determining step was the first electron transfer.

Single-atom Co–N–C catalysts not only exhibit superior HER and ORR performance, but also display good OER activity. Cao et al. synthesized a  $\text{CoN}_4/\text{NG}$  catalyst by pyrolysis and acid-leaching strategy (Fig. 3a–h), which showed an overpotential ( $\eta_{10}$ ) of  $0.38 \text{ V}$  at  $10 \text{ mA cm}^{-2}$  for OER [70]. Han and coworkers synthesized a single-atom cobalt-based electrocatalyst with urchin-like nano-tube hierarchical structure (UNT Co SAs/N–C) by a sacrificed-template method for efficient OER [71]. By DFT calculations, they predicted that the OER activity decreased in the sequence of  $\text{Co–N}_4 > \text{Co–N}_3 > \text{Co–N}_2 > \text{Co–N}_1$ . Moreover, Guan et al. found that the theoretical overpotentials on  $\text{Co–N}_4$ ,  $\text{Co–N}_3$ , and  $\text{Co–N}_2\text{C}_2$  sites were  $0.41$ ,  $0.9$ , and  $0.53 \text{ V}$ , respectively (Fig. 3i–k), indicating that the  $\text{Co–N}_4$  site should be the most active center for efficient OER [72]. Due to bifunctional OER/ORR performance, the Co–N–C catalyst can be employed into a Zn-air battery, showing comparable power density with that of Pt/C-based device [73].

**4.1.2.2.  $\text{Fe–N}_4$  configuration.**  $\text{FeN}_4$  moiety embedded onto carbon frameworks have been considered as the most active catalyst for alkaline ORR [74–82]. As early as in 2009, Lefèvre et al. found that Fe–N–C catalysts with iron atom coordinated with four pyridinic nitrogen atoms can be obtained by two-step pyrolysis method, which showed comparable ORR activity with Pt [83]. In 2011, Wu et al. used polymerized  $\text{Fe}^{3+}$ -containing aniline to form  $\text{Fe}^{3+}$ -incorporating polyaniline, which was pyrolysed to obtain Fe–N–C materials, showing good ORR activity [82]. However, Fe-based nanoparticles existed in the obtained PANI-Fe-C catalysts, and the active sites for ORR were proposed to be  $\text{FeN}_4$ -type configurations in Fe macrocycles. In 2015, Zitolo et al. used Mössbauer spectra and XAS technique to reveal the active sites of single-atom Fe–N–C catalysts for ORR [84]. They ascribed the enhanced ORR performance on  $\text{NH}_3$ -pyrolysed Fe–N–C catalysts compared with Ar-pyrolysed ones to the formation of formation of  $\text{FeN}_4\text{C}_{12}$  moieties. In 2017, Zelenay et al. reported that hierarchical porous single-atom Fe–N–C catalysts exhibited comparable  $\text{H}_2$ -air fuel cell performance with Pt cathode catalysts [74]. By atomic-resolution HAADF-STEM technique, they observed directly the structure of active sites, which should be  $\text{FeN}_4$  sites. In addition, by theoretical calculations, they found that edge-hosted and bulk-hosted  $\text{FeN}_4$  followed different ORR reaction pathways and edge-hosted  $\text{FeN}_4$  showed higher ORR activity than bulk-hosted  $\text{FeN}_4$ . In alkaline media, Fe-SACs demonstrated better ORR activity than commercial Pt/C, while in acidic media, they usually showed inferior ORR performance than Pt/C. Theoretical simulations predicted that the Fe-pyrrolic-N species showed better electrocatalytic performance ( $\text{U}^{\text{onset}}$ ,  $\Delta G_{\text{max}}$ , and  $\Delta G_{\text{H}_2\text{O}_2}$ ) than Pt/C [81].

Due to high ORR activity of single-atom Fe–N–C catalysts, they have attracted a lot of attention in recent years [85–88]. Fe–N–C catalysts were usually synthesized by pyrolysis method. For instance, Xu et al. synthesized a single-atom Fe–N–C catalyst by pyrolyzing a Fe-tpphz compound, which showed a positive  $E_{1/2}$  of  $0.863 \text{ V}$  vs. RHE in a  $0.1 \text{ M KOH}$  [89]. The Zn-air cell assembled with the Fe–N–C as the cathodic catalyst provided an open circuit voltage of  $1.53 \text{ V}$  and power density of  $947 \text{ W h kg}^{-1}$ . Shao et al. constructed a single-atom Fe–N–C catalyst by pyrolyzing a zeolitic imidazolate framework (ZIF-8), which exhibited good ORR activity with half-wave potentials of  $0.81$  and  $0.90 \text{ V}$  in  $0.1 \text{ M HClO}_4$  and  $0.1 \text{ M KOH}$ , respectively [90]. Dai et al. immobilized atomically dispersed Fe onto on hierarchically structured porous carbon by

pyrolysis of the mixture of phthalocyanine and iron phthalocyanine, which displayed a positive  $E_{1/2}$  of  $0.89 \text{ V}$  vs. RHE and large diffusion limited current density of  $5.4 \text{ mA cm}^{-2}$  in a  $0.1 \text{ M KOH}$  [91]. Feng et al. constructed high-density  $\text{Fe–N}_x$  moieties onto hierarchically porous carbon by a Zn-mediated template synthesis strategy, which exhibited high ORR activity with a positive  $E_{1/2}$  of  $0.93 \text{ V}$  vs. RHE in a  $0.1 \text{ M KOH}$  [92]. The SA-Fe-NHPC-based Zn-air battery exhibited an open-circuit voltage of  $1.5165 \text{ V}$  and a maximum power density of  $266.4 \text{ mW cm}^{-2}$ . Wang and coworkers found that edge-hosted  $\text{Fe–N}_4$  moieties can be constructed by hierarchical pores triggered cleavage of the C–N bond adjacent to Fe center, which demonstrated a positive  $E_{1/2}$  of  $0.915 \text{ V}$  vs. RHE in a  $0.1 \text{ M KOH}$  [93]. By theoretical simulations, they found that edge-hosted  $\text{Fe–N}_4$  moieties exhibited lower overall reaction energy barrier of  $0.32 \text{ eV}$  than other configurations.

In addition, single-atom Fe–N–C catalysts have been investigated in acidic ORR and applied in proton exchange membrane fuel cell (PEMFC) [94–99]. Wang et al. obtained  $\text{FeN}_4$ -doped hierarchical ordered porous carbon by pyrolyzing Fe-doped ZIF-8, showing a positive  $E_{1/2}$  of  $0.8 \text{ V}$  in  $0.5 \text{ M H}_2\text{SO}_4$  [100]. The PEMFC with  $\text{FeN}_4/\text{HOPCc-1000}$  as the cathodic catalyst derived a current density of  $0.42 \text{ W cm}^{-2}$  at  $0.57 \text{ V}$  under 1 bar  $\text{H}_2$ -air. Wu et al. found that the critical temperature for generating new bonds related to N, C, and Fe was around  $800 \text{ }^\circ\text{C}$  for the pyrolysis of Fe-ZIF networks [101]. The number of active sites can be modulated by altering the particle size of Fe-ZIF nanocrystal precursors. The Fe–N–C catalyst with  $50 \text{ nm}$  exhibited the best ORR performance with a positive  $E_{1/2}$  of  $0.85 \text{ V}$  vs RHE in  $0.5 \text{ M H}_2\text{SO}_4$ . Zhao et al. prepared MOF-derived three-dimensional carbon materials with atomic  $\text{Fe–N}_4$  sites for efficient acidic ORR with an onset potential of  $0.906 \text{ V}$  [102]. The PEMFC assembled with the Fe–N–C as the cathodic catalyst showed a 20% current drop after stability test for  $20 \text{ h}$  at  $0.5 \text{ V}$ . Li et al. prepared a porous single-atom Fe SAs/N–C catalyst with  $3.5 \text{ wt\%}$  Fe content and high BET surface area of  $1097 \text{ m}^2 \text{ g}^{-1}$ , which showed high ORR activity and stability in both acidic and basic media [77]. The Fe SAs/N–C based Zn–air battery exhibited a maximum power density of  $225 \text{ mW cm}^{-2}$ , and the maximum power density of Fe SAs/N–C based  $\text{H}_2/\text{O}_2$  PEMFC reached  $0.68 \text{ W cm}^{-2}$  under back pressure of  $0.1 \text{ MPa}$ . Shui et al. synthesized a concave-shaped Fe–N–C SAC by coating a layer of  $\text{SiO}_2$  and then leaching strategy, which showed increased external surface area and density of  $\text{Fe–N}_4$  sites [79]. The single-atom Fe–N–C catalysts displayed high performance in PEMFCs, providing a power density of  $1.18 \text{ W cm}^{-2}$  under  $2.5 \text{ bar H}_2\text{–O}_2$ . They found that the current density of PEMFCs was predominantly determined by the density of active  $\text{Fe–N}_4$  sites. Surendranath et al. found that a molecular pyridinic hexaazacyclophane macrocycle ( $\text{phen}_2\text{N}_2\text{Fe}$ ) showed better ORR performance than the pyrrolic macrocycles, but inferior ORR activity than typical Fe–N–C catalysts, indicating that the chemical surroundings of active sites would influence the catalytic performance [99].

It has been controversial whether individual Fe sites can be acted as efficient active sites for OER on Fe-based (oxy)hydroxides because Co or Ni sites were experimentally distinguished to be active, while theoretical calculations predicted low energy barrier at Fe sites [103–105]. Guan et al. found that atomic  $\text{Fe–N}_4$  sites showed ultralow overpotentials of  $194$  and  $275 \text{ mV}$  at  $10 \text{ mA cm}^{-2}$  in  $1 \text{ M KOH}$  and  $0.1 \text{ M KOH}$ , respectively [106]. The theoretical OER overpotential on the  $\text{Fe–N}_4$  site is  $0.38 \text{ V}$ , far lower than those on  $\text{FeOOH}$  (010) ( $0.72 \text{ V}$ ),  $\text{IrO}_2$  (110) ( $0.47 \text{ V}$ ), and  $\text{Fe–N}_3$  site ( $1.2 \text{ V}$ ), which was consistent with the experimental results, indicating efficient active sites of Fe centers on theory and experiment. The formation of  $\text{OOH}^*$  species should be the rate-determining step on the single-atom  $\text{Fe–N}_4$  site for OER. Zhi et al. found that  $\text{Fe–N}_x$  moieties embedded on porous N-doped carbon showed an  $E_{1/2}$  of  $0.86 \text{ V}$  vs. RHE for ORR and an overpotential of  $390 \text{ mV}$  at  $10 \text{ mA cm}^{-2}$  for OER in  $0.1 \text{ M KOH}$  [104]. The assembled rechargeable Zn-air battery provided a power density of  $118 \text{ mW cm}^{-2}$ .

Electrocatalytic  $\text{CO}_2$  reduction reaction ( $\text{CO}_2\text{RR}$ ) has gained increasing interest due to moderate reaction conditions and steerable high-value-added products [107–111]. However, due to the competition

of HER, a poor selectivity of target products, e.g. HCOOH, HCHO, CH<sub>3</sub>OH, CH<sub>4</sub>, and CO, was generally observed with low Faraday efficiency (FE) [112]. The unique structure of SACs with tunable electronic property of metal centers is beneficial to speed up reaction rates, tune selectivity, and comprehend the structure-function relations at the atomic scale. Tour et al. found that a Fe/NG catalyst with Fe–N<sub>4</sub> sites exhibited 80% Faradic efficiency at a low overpotential in 0.1 M KHCO<sub>3</sub> for electrocatalytic CO<sub>2</sub> reduction to CO (Fig. 4a–d) [113]. Fontecave et al. reported that Fe–N–C catalysts with isolated FeN<sub>4</sub> sites displayed 90% CO Faradic efficiency for electrochemical CO<sub>2</sub>RR at a low overpotential of 190 mV in 0.5 M NaHCO<sub>3</sub> [114]. CO desorption was the rate-determining step at −0.5 V vs. RHE [115], and the Fe–N<sub>4</sub> sites favored CO<sub>2</sub> adsorption and activation [113]. Theoretical calculations predicted that CO<sub>2</sub>, CO, and CH<sub>2</sub>O were only converted into methane on Fe–N<sub>x</sub> sites, and CH<sub>3</sub>OH should be an end product (Fig. 4e) [116]. Wu et al. found that the intrinsic CO<sub>2</sub>RR activity of FeN<sub>4</sub> sites depended on the length of the Fe–N bonds and the local strains, which can be modulated by altering thermal treatment temperature during the synthetic process [117]. The Fe–N bonds can be formed at relatively low temperatures (e.g. 400 °C), and the Fe–N bond's local contraction strain happened with raising temperatures. The CO<sub>2</sub>RR activity of the Fe–N–C catalysts can be gradually increased with increasing the annealing temperature up to 1100 °C, above which the thermal decomposition of FeN<sub>4</sub> sites would happen.

Due to inherent nature of the N≡N triple bond, hydrogenation of nitrogen to produce ammonia is mainly through the Haber–Bosch method under rigorous reaction conditions (400–600 °C, 20–40 MPa), which results in high energy input and vast carbon dioxygen emissions [118]. There is growing concern about electrochemical nitrogen reduction reaction (NRR) since it can be carried out at atmospheric pressure and moderate temperature. Due to the competition of HER with two-electron transfer, most electrocatalysts suffered from slow reaction kinetics and low Faradaic efficiency for the electroreduction of N<sub>2</sub> to NH<sub>3</sub>. Seeking electrocatalysts with wide potential gap between NRR and HER and high activity to boost the NRR kinetics at low overpotentials is the current main research interests. Due to poor HER performance, the Fe–N<sub>4</sub> site is favorable for N<sub>2</sub> activation [119]. A single-atom Fe-based catalyst (ISAS-Fe/NC) exhibited 18.6% faradaic efficiency of ammonia and a yield rate of 62.9 μg h<sup>−1</sup> mg<sub>cat</sub><sup>−1</sup> at −0.4 V vs. RHE in neutral solutions. During NRR, the electrons were shifted from 3 d orbit of Fe to 2p orbit of N, thus activating \*N<sub>2</sub> for succent hydrogenation. The enzymatic mechanism (N<sub>2</sub> molecule adsorbs via side-on coordination) was proposed on the Fe–N<sub>4</sub> sites. Yan et al. found that 56.55% Faradaic efficiency can be obtained on a single-atom catalyst Fe<sub>SA</sub>–N–C in 0.1 M KOH [120]. The binding energy of \*N<sub>2</sub> on the Fe–N<sub>4</sub> site was −0.28 eV, indicating an exothermic process and enhanced absorbability of nitrogen. Different from the first hydrogenation step as the rate-determining step on noble metal catalysts, the last step (\*OH–NH<sub>3</sub> + NH<sub>3</sub> + H<sup>+</sup> + e<sup>−</sup> → \*OH + 2NH<sub>3</sub>) should be the reaction bottleneck over the Fe–N<sub>4</sub> site with a small energy barrier of 2.38 kJ mol<sup>−1</sup>.

**4.1.2.3. Ni–N<sub>4</sub> configuration.** Since single-atom Ni–N–C catalysts exhibited high electrocatalytic activity and CO FE for CO<sub>2</sub>RR, they got a lot of attention in recent years [121]. Xie reported a single-atom Ni-based catalyst with Ni–N<sub>4</sub> structure, which exhibited superior performance for electrochemical reduction of carbon dioxide to carbon monoxide with high current density of 28.6 mA cm<sup>−2</sup> and superhigh faradaic efficiency of 99% at −0.81 V vs. RHE [122]. The potential limiting step of CO<sub>2</sub>RR on the Ni–N<sub>4</sub> site should be the formation of adsorbed intermediate COOH\* species. Compared with Ni-free N–C sites, the Ni–N<sub>4</sub> sites can lower the formation energy of COOH\*, thus accelerating the reaction. Liu et al. found that the monovalent Ni<sup>+</sup> with a d<sup>9</sup> electronic configuration should be the active center for CO<sub>2</sub>RR [123]. The charge transfer from A-Ni-NG to CO<sub>2</sub> and the generation of CO<sub>2</sub><sup>δ−</sup> species would lead to the reduction of the valence state of Ni sites. Hou

et al. synthesized Ni–N<sub>4</sub> moieties embedded onto carbon matrix by an axial traction strategy for electrochemical CO<sub>2</sub>RR, which exhibited 99.2%CO FE at −0.9 V and above 90% FE at potentials ranged from −0.5 to −1.1 V [124]. One axial O atom on the Ni–N<sub>4</sub> site could adjust the electronic structure of Ni–N<sub>4</sub> moiety, increase charge polarization, and decrease the CO<sub>2</sub>RR barrier, thus enhancing CO<sub>2</sub>RR performance. Cao et al. found that Ni–N<sub>4</sub> moieties embedded onto hollow mesoporous carbon spheres exhibited CO FE of 95% at potentials ranged from −0.7 to −1.1 V vs. RHE for electrochemical CO<sub>2</sub>RR, and high turnover frequency of 15608 h<sup>−1</sup> [125]. Liu et al. adopted operando XAS technique to reveal that Ni<sup>+</sup> in the Ni–N–C was active for CO<sub>2</sub> activation, over which the potential-determining step was the step of \*CO<sub>2</sub><sup>−</sup> + H<sup>+</sup> → \*COOH [126].

Since nickel oxide is the best OER electrocatalyst among non-noble metal oxides, development of single-atom Ni-based electrocatalysts is fascinating. Huang et al. found that the NiN<sub>4</sub>C<sub>4</sub> site exhibited higher OER activity than CoN<sub>4</sub>C<sub>4</sub> and FeN<sub>4</sub>C<sub>4</sub> [127]. According to theoretical simulations, both Ni and C in the NiN<sub>4</sub>C<sub>4</sub> moiety were possible absorption sites for the oxygen intermediates. The O\* and OH\* intermediates were readily adsorbed on the carbon site, whereas the OOH\* intermediate was preferentially generated on the Ni site. The formation of OOH\* was the rate-determining step on the NiN<sub>4</sub>C<sub>4</sub> site with dual-site mechanism. Vegge et al. and Du et al. also found that four nitrogen-coordinated Ni atoms showed excellent OER performance [128,129]. Lou et al. found that the electronic coupling effect of Ni–N coordination could lower the Fermi level and reduce the adsorption energy of OH\* and OOH\* species, thus facilitating OER kinetics [130].

**4.1.2.4. Mn–N<sub>4</sub> configuration.** Although Fe–N–C catalysts show high ORR activity, there has been a great challenge for their stability since the Fe–N bond would be broken by the attack of generated H<sub>2</sub>O<sub>2</sub> [131]. According to our previous calculations, the formation energy of the FeN<sub>4</sub> configuration is −2.1 eV, which is 0.5 eV larger than that of MnN<sub>4</sub> configuration, indicating worse stability of FeN<sub>4</sub> than MnN<sub>4</sub> [106]. Therefore, from a practical standpoint, single-atom Mn–N–C catalysts are more appropriate for ORR than Fe–N–C materials [132,133]. Wu et al. reported that a Mn–N–C catalyst with atomic MnN<sub>4</sub> sites showed a E<sub>1/2</sub> of 0.80 V vs. RHE and excellent stability in acidic media [131]. Theoretical simulations uncovered that the MnN<sub>2</sub>C<sub>12</sub> and MnN<sub>3</sub>C<sub>9</sub> sites with few coordinated N atoms bonded H<sub>2</sub>O too strongly to be efficient active sites, while MnN<sub>3</sub>C<sub>11</sub>, MnN<sub>4</sub>C<sub>8</sub>, and Mn<sub>2</sub>N<sub>5</sub>C<sub>12</sub> sites bonded the intermediate OH too strongly to be effective active sites. Combined with EXAFS analysis, the MnN<sub>4</sub>C<sub>12</sub> sites were considered to be efficient active sites for the 4e<sup>−</sup> ORR, which was confirmed by several research groups [132,134,135]. Liu and coworkers found a Mn-SAS/CN catalyst showing a high E<sub>1/2</sub> of 0.91 V vs. RHE in alkaline media and adopted operando XAS technique to monitor the change of Mn valence states during ORR (Fig. 5a–f) [135]. They found that more Mn sites would be reduced to lower valence states as increasing overpotential and low-valence Mn<sup>L+</sup>–N<sub>4</sub> was the active site for ORR. Guan et al. found that MnN<sub>4</sub> moieties embedded into N-doped graphene exhibited excellent ORR performance in alkaline media [132]. Theoretical calculations further revealed that the ORR overpotential on Mn–N<sub>4</sub>-G site was 0.63 V, c than that on graphitic-N (1.18 V), pyridinic-N (1.58 V), MnN<sub>3</sub>-G (1.48 V), and MnN<sub>3</sub>O-G (2.33 V). Xu et al. predicted that the ORR thermodynamic limiting overpotential on the MnN<sub>4</sub>/C site was 0.71 V, larger than that (0.44 V) on the FeN<sub>4</sub>/C site [136]. In addition, the ORR rate-determining step on the MnN<sub>4</sub>/C site was the formation of OOH\*, different from that (formation of the second H<sub>2</sub>O molecule) on the FeN<sub>4</sub>/C.

Due to slow kinetics of OER involving multi-proton-coupled electron-transfer steps, catalysts should possess excellent charge transfer ability to perform this reaction. The natural oxygen-evolving center CaMn<sub>4</sub>O<sub>5</sub> can fleetly catalyze water oxidation due to the synergetic action between two adjacent Mn ions in the multinuclear manganese cluster [11]. Very recently, Guan et al. found that a single-site manganese with Mn–N<sub>4</sub>

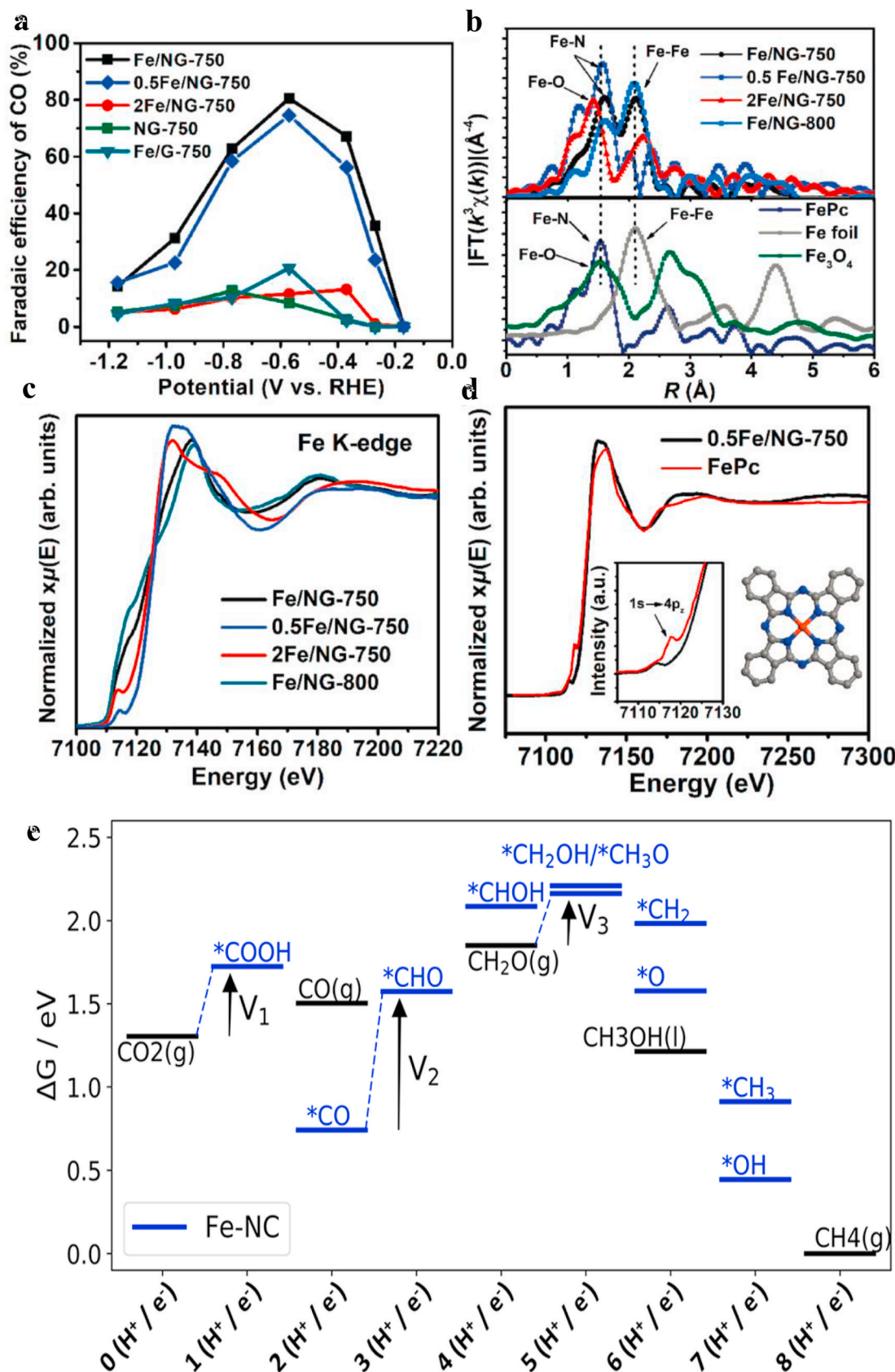


**Fig. 4.** (a) FE of CO for electrochemical  $\text{CO}_2$  reduction on Fe/NG. (b) Fe K-edge FT-EXAFS spectra of Fe/NG. (c-d) Normalized Fe K-edge XANES spectra of Fe/NG. Reproduced with permission [113]. Copyright 2018 Wiley-VCH. (e) Free energy diagrams toward  $\text{CH}_4$  starting from  $\text{CO}_2$ ,  $\text{CO}$  and  $\text{CH}_2\text{O}$  on Fe–N–C catalysts at 0  $V_{\text{RHE}}$  and with reference to  $\text{CH}_4$ . Reproduced with permission [116]. Copyright 2019 American Chemical Society.

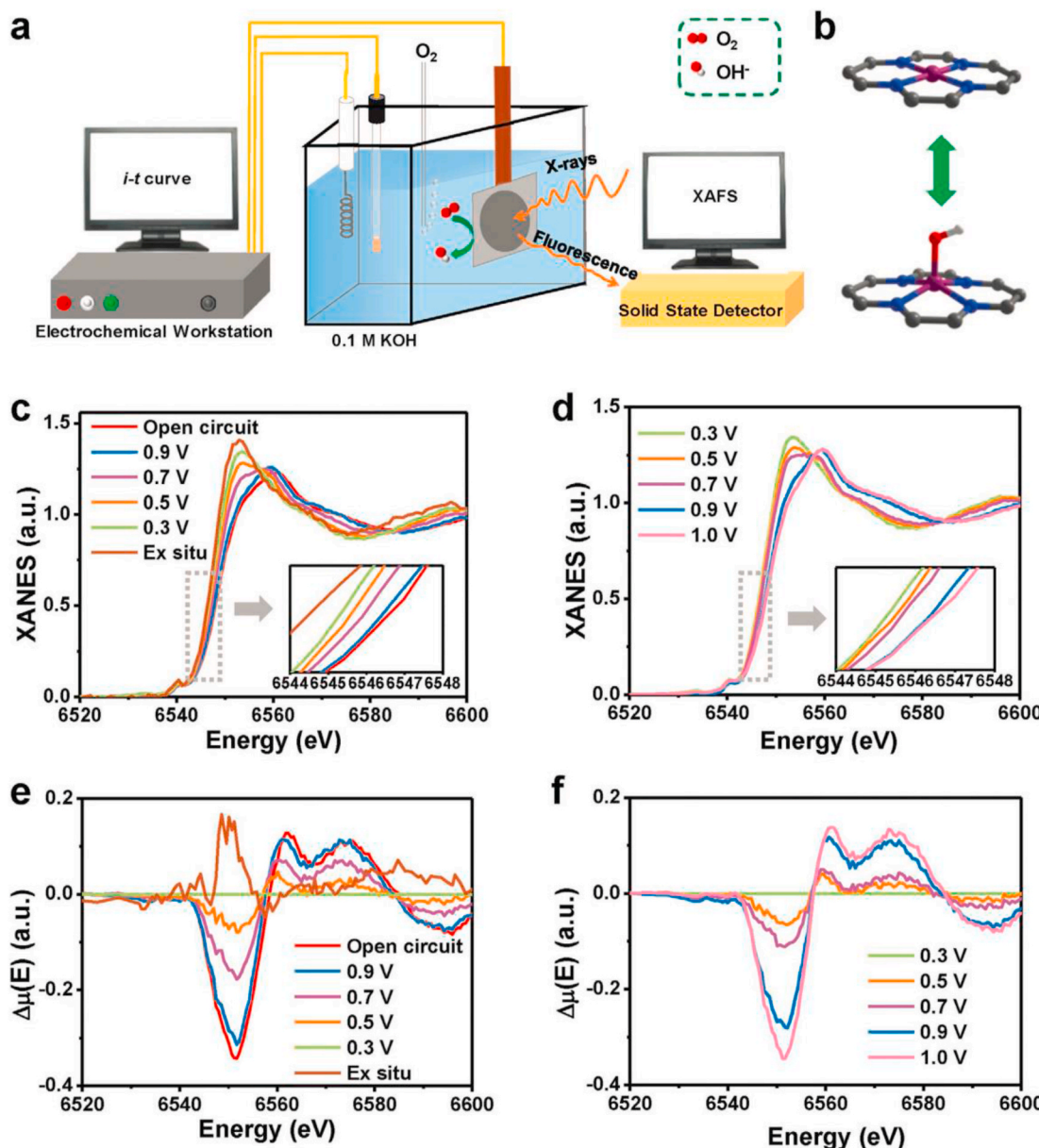


**Fig. 5.** (a) Experimental setup of operando X-ray absorption spectra device. (b) The structural model with/without OH<sub>ads</sub> of Mn-SAS/CN. (c,d) Operando XANES and (e,f)  $\Delta\mu$ -XANES ( $\mu_E - \mu_{0.3V}$ ) of Mn-SAS/CN catalyst collected ex situ and (c,e) at the open circuit from 0.9 to 0.3 V and (d,f) from 0.3 to 0.9 V in O<sub>2</sub>-saturated KOH. Reproduced with permission [135]. Copyright 2020 Wiley-VCH.

moieties embedded into graphene matrix (Mn-NG) can catalyze water oxidation with TOF up to  $214\text{ s}^{-1}$ , comparable to that of photosystem II [6]. The Mn-NG showed a low overpotential of 337 mV at  $10\text{ mA cm}^{-2}$  and superior stability in alkaline media. Theoretical simulations uncovered that the oxidation of OH\* to O\* was the overpotential-determining step of OER on the Mn-N<sub>4</sub> site, which is different from the O-O coupling step on catalysts with multinuclear Mn sites. Furthermore, Rossmeisl et al. predicted theoretically that MnN<sub>4</sub>-moiety embedded in graphene could show bifunctional ORR/OER activity [137]. Zeng et al. predicted that Mn-pyridine-N<sub>4</sub> moiety surrounded by five B atoms on graphene could show relatively low theoretical overpotential of 0.43 V for OER [138].

**4.1.2.5. Cu-N<sub>4</sub> configuration.** Li et al. used a gas-migration method to convert bulk copper into atomic copper by emitting and trapping of Cu atoms [139]. The valence state of copper species in Cu-SAs/N-C was between 0 and + 2, and the Cu-N<sub>4</sub> coordination was formed. The

Cu-SAs/N-C demonstrated higher acidic ORR activity than commercial Pt/C catalyst in term of half-wave potential. Xiang et al. found that the transformation of OOH\* to O\* was the rate determining step on the Cu-N<sub>4</sub> sites, whose free energy change ( $|\Delta G|$ ) is 0.30 eV, slightly lower than that (0.33 eV) on the Pt (111) surface [140].

Zheng et al. investigated the electrocatalytic CO<sub>2</sub>RR performance over atomic Cu-N<sub>x</sub> sites embedded on the N-doped carbon and found that Cu-N-C-800 exhibited a FE of 24.8% for C<sub>2</sub>H<sub>4</sub> production at  $-1.4\text{ V}$  vs RHE, while Cu-N-C-900 displayed a FE of 38.6% and a current density of  $14.8\text{ mA cm}^{-2}$  for CH<sub>4</sub> production at  $-1.6\text{ V}$  vs RHE. By theoretical simulations, they proposed that CH<sub>4</sub> would be preferably produced on isolated Cu-N<sub>4</sub>, neighboring Cu-N<sub>4</sub>, and isolated Cu-N<sub>2</sub> sites, while C<sub>2</sub>H<sub>4</sub> can be manufactured on two adjacent Cu-N<sub>2</sub> sites [141].

**4.1.2.6. Cr-N<sub>4</sub> configuration.** Xing et al. fabricated an atomic Cr-N-C catalyst by pyrolysis and acid leaching method, which demonstrated

high ORR activity with a  $E_{1/2}$  of 0.773 V vs. RHE in 0.1 M HClO<sub>4</sub> [142]. By XAS analysis, they identified that the main structure of Cr should be Cr–N<sub>4</sub> coordination. Different from two-electron ORR pathway on a molecular complex chromium(V)–oxo tris(pentafluorophenyl)corrole [143], the Cr–N–C showed a main 4e<sup>-</sup> ORR mechanism.

**4.1.2.7. Zn–N<sub>4</sub> configuration.** Xu et al. found that an atomic ZnN<sub>x</sub>/C catalyst exhibited high catalytic activity (TOF: 9969 h<sup>-1</sup>), high CO selectivity (Faradaic efficiency of 95% at -0.43 V vs. RHE), and outstanding stability for CO<sub>2</sub>RR [5]. Theoretical simulations revealed that the Zn–N<sub>4</sub> site showed lower free energy barrier (0.662 eV) than N<sub>4</sub>–C (1.754 eV) and Zn–C (2.07 eV) for the formation of \*COOH. Moreover, the desorption free energy of CO on the Zn–N<sub>4</sub> was more negative than that on N<sub>4</sub>–C and Zn–C.

Moreover, atomically dispersed Zn–N<sub>4</sub> sites demonstrated comparable ORR activity with Pt/C in alkaline electrolytes [144,145]. The maximal power density for the Zn–N–C-1 based Zn–O<sub>2</sub> battery can reach 179 mWcm<sup>-2</sup>. Compared with Fe–N<sub>4</sub> sites, Zn–N<sub>4</sub> structure was more electrochemically stable for ORR by theoretical simulations.

**4.1.2.8. Ru–N<sub>4</sub> configuration.** Guan et al. found that a 0.4-Ru@NG-750 catalyst showed low HER overpotentials of only 40 and 90 mV at 10 mA cm<sup>-2</sup> in 1.0 M KOH and 0.5 M H<sub>2</sub>SO<sub>4</sub>, respectively [146]. Combining theoretical calculations, they found that the Ru–N<sub>4</sub>C<sub>x</sub> was the active site for HER, over which the theoretical overpotential is 0.2 V, similar to Pt (111). Additionally, the RuN<sub>4</sub>C<sub>x</sub> structure would transform to RuN<sub>4</sub>(O)C<sub>x</sub> during OER since the RuN<sub>4</sub>(O)C<sub>x</sub> was more stable than RuN<sub>4</sub>C<sub>x</sub>. The theoretical overpotential on the RuN<sub>4</sub>(O)C<sub>x</sub> was 0.6 V, smaller than that (0.65 V) on the state-of-the-art catalyst RuO<sub>2</sub>, indicating high activity of RuN<sub>4</sub>(O)C<sub>x</sub> for OER.

In addition, for the RuN<sub>4</sub> site, it will bind a –OH group under ORR condition [146–148]. The reaction barrier on Ru-oxo-N<sub>4</sub> site was ~0.76 eV at 1.23 V vs. RHE, close to that on the Fe–N<sub>4</sub> site (0.94 eV). The theoretical ORR overpotential on RuN<sub>4</sub>(OH)C<sub>x</sub> was predicted to be 0.7 V, slightly higher than that on Pt(111).

**4.1.2.9. Ir–N<sub>4</sub> configuration.** Guan et al. reported that Ir–N<sub>4</sub>C<sub>x</sub> moiety embedded into N-doped graphene displayed superior HER performance with low overpotential of only 25 mV at 10 mA cm<sup>-2</sup> in 0.5 M H<sub>2</sub>SO<sub>4</sub> [149]. The theoretical HER overpotential on Ir–N<sub>4</sub>C<sub>x</sub> is 0.17 V, slightly smaller than that (0.2 V) on Pt(111). In addition, the Ir–N<sub>4</sub> sites embedded into N-doped graphene showed excellent OER activity with overpotentials of 273, 340, and 371 mV at 10 mA cm<sup>-2</sup>, in 1 M KOH, 0.1 M KOH, and 0.5 M H<sub>2</sub>SO<sub>4</sub>, respectively [149]. The theoretically predicted overpotentials on the Ir–N<sub>4</sub> site were 0.35 and 0.28 V at pH = 1 and pH = 13, respectively, lower than those on IrO<sub>2</sub>(110), suggesting that the Ir–N<sub>4</sub> site is active for OER.

The Ir-SAC displayed high ORR activity with a turnover frequency (TOF) of 24.3 e<sup>-</sup> site<sup>-1</sup> s<sup>-1</sup> at 0.85 V vs. RHE and a mass activity of 12.2 Amg<sup>-1</sup>Ir in acidic media [150]. In alkaline media, the Ir-SAC displayed outstanding ORR activity with a  $E_{1/2}$  of 0.865 V vs. RHE [149]. When it was assembled into a Zn-air battery, it exhibited a maximal power density of 56.8 mW cm<sup>-2</sup>. For the IrN<sub>4</sub> site, the density of states (DOS) was calculated to be -2.89 eV [150], and the predicted ORR overpotentials were 0.41 V and 0.33 V at pH = 1 and pH = 13, respectively [149].

**4.1.2.10. Other M–N<sub>4</sub> configurations.** Li and coworkers found that 97% CO Faradaic efficiency and high turnover frequency (5535 h<sup>-1</sup>) at an overpotential of 0.39 V can be achieved on the Bi–N<sub>4</sub> site [151]. The Bi–N<sub>4</sub>/C structure exhibited a more positive difference (-0.02 V) between limiting potentials (U<sub>L</sub>(CO<sub>2</sub>)–UL(H<sub>2</sub>)) than that of Bi(110) (-0.1 V) and BiC<sub>4</sub> (-0.2 V), implying higher selectivity to CO on the Bi–N<sub>4</sub> site.

Noble metal Rh–N<sub>4</sub> sites showed superior ORR activity, comparable

to Pt (111) [152]. DFT calculations predicted that the theoretical ORR overpotential of RhN<sub>4</sub> was 0.59 V, which is slightly larger than that of Pt (111) (0.53 V), but much smaller than that of RhN<sub>3</sub> (1.23 V) [153]. Experimental results manifested that the RhN<sub>4</sub> site demonstrated higher ORR activity than commercial Pt/C in alkaline electrolytes, but worse ORR activity in acidic media.

Wang and coworkers synthesized a Pt<sub>1</sub>/NPC catalyst by photochemical reduction of PtCl<sub>6</sub><sup>2-</sup> ions [154]. The Pt<sub>1</sub>/NPC with 3.8 wt% Pt loading exhibited mass activity of 2.86 A mg<sup>-1</sup> Pt in 0.1 M HClO<sub>4</sub>, which is 24 times higher than commercial Pt/C. Due to electron transfer from isolated Pt atoms to adjacent N atoms and abundant unoccupied 5d orbitals of isolated Pt atoms, the H 1s orbitals can interact with them to form electron pairing and hydride, contributing the H coverage on the Pt surface and thus boosting HER kinetics.

#### 4.1.3. M–N<sub>3</sub> configuration

Li et al. proposed that high-spin polarization of Fe–N<sub>3</sub> moiety embedded into graphene was the possible active-site for NRR through first-principles calculations [155]. They also predicted that Sc, V, and Mn with a high-spin polarization embedded at the defect of graphene could be active for N<sub>2</sub>-fixation.

Jiang et al. found that the electrocatalytic reduction of carbon dioxide to carbon monoxide occurred more likely on the edge-anchored unsaturated NiN<sub>3</sub> sites [5]. Theoretical simulations uncovered that the edge-anchored NiN<sub>3</sub> structure are more stable than low coordinated NiN<sub>2</sub> and NiN<sub>2</sub>(NH<sub>2</sub>) structures under N-rich conditions. Compared with the in-plane NiN<sub>4</sub> (2.03 eV, CO<sub>2</sub>→\*COOH) and edge-anchored NiN<sub>2</sub>(NH<sub>2</sub>) (1.02 eV), edge-anchored unsaturated NiN<sub>3</sub> exhibited lower energy for CO<sub>2</sub> activation (0.7 eV).

Bai et al. found that the structure of active sites can be modulated by tuning pyrolysis temperature for Cu-doped ZIF-8, and isolated Cu–N<sub>3</sub> sites would be formed at the annealing temperature of 900 °C, which showed higher ORR activity than Cu–N<sub>4</sub> moieties embedded onto carbon [156]. DFT calculations revealed that the O<sub>2</sub> adsorption upslope for CuN<sub>3</sub> was only 0.17 eV, smaller than that for CuN<sub>4</sub> (0.87 eV), NC (2.1 eV), and Pt (111) (0.65 eV), implying favorable adsorption of O<sub>2</sub> on the CuN<sub>3</sub> site.

By DFT calculations, Song et al. disclosed that the Mo–N<sub>3</sub> site exhibited the highest NRR activity with a theoretical overpotential of 0.02 V among a series of isolated molybdenum atoms supported on N-doped black phosphorus [157]. Compared with the enzymatic and alternating mechanisms, the associative distal mechanism should be preferred on the Mo–N<sub>3</sub> site. In addition, higher selectivity to NRR than the competing HER can be achieved on the Mo–N<sub>3</sub> site.

Zeng and coworkers found that atomic Ru dispersed on nitrogen-doped carbon exhibited a Faradaic efficiency of 29.6% for NH<sub>3</sub> production [158]. By theoretical simulations, they proposed that the NRR on the Ru–N<sub>3</sub> sites followed the distal pathway and the ΔG for N<sub>2</sub> dissociation (rate-limiting step) on Ru–N<sub>3</sub> was 0.73 eV, smaller than that on Ru (101) (0.91 eV) and Ru–N<sub>4</sub> (0.77 eV).

#### 4.1.4. M–N<sub>2</sub> configuration

**4.1.4.1. Co–N<sub>2</sub> configuration.** The metal ion in the M–N<sub>2</sub> structure is flexible, which tends to anchor other ligands (e.g. O or C atoms) to increase the stability. Combining operando XAS measurements and DFT calculations, Wei et al. found that a high-valence HO–Co–N<sub>2</sub> moiety was formed by binding one OH<sup>-</sup> group to the Co atom in an end-on configuration of isolated Co–N<sub>4</sub> sites during HER [39]. The HO–Co–N<sub>2</sub> site exhibits an energy barrier of 0.52 eV for one H<sub>2</sub>O molecule dissociation step, lower than Pt(111) (0.81 eV). Moreover, the H adsorption energy on the HO–Co–N<sub>2</sub> site is 0.36 eV, lower than that (0.48 eV) on Pt (111), suggesting comparable HER activity of the HO–Co–N<sub>2</sub> site with Pt.

Wu et al. investigated atomically dispersed Co catalysts for CO<sub>2</sub>RR,

and found that 94% CO formation Faradaic efficiency and a current density of  $18.1 \text{ mA cm}^{-2}$  at an overpotential of 0.52 V was achieved on Co–N<sub>2</sub> sites, which is far higher than that on Co–N<sub>3</sub> sites (Faradaic efficiency of 63%), Co–N<sub>4</sub> sites (<5%), and Co NPs (<7%) (Fig. 6a-h) [159]. DFT simulations uncovered small endergonic formation of CO<sub>2</sub><sup>\*\*</sup> on Co–N<sub>2</sub>, resulting in high CO Faradaic efficiency. Bao et al. synthesized a single-atom Ni–N–C catalyst, which exhibited a CO Faradaic efficiency of 92–98% at potentials from –0.53 to –1.03 V vs. RHE [160]. DFT simulations uncovered that the free energy of \*COOH (0.62 eV) on the Ni<sub>2</sub>V<sub>2</sub> site was smaller than the free energy of \*H (0.69 eV), suggesting high selectivity to CO.

**4.1.4.2. Other M–N<sub>2</sub> configurations.** The FeN<sub>2</sub> site was found to be more active for ORR than FeN<sub>4</sub> site in both basic and acidic electrolytes [161, 162]. Xu and coworkers found that the alkaline ORR activity order among different sites was followed: Fe–N<sub>4/2</sub>–C > Fe<sub>4</sub>–N–C > N–C > Fe<sub>4</sub>–C ≥ C [161]. Hu et al. synthesized atomic Fe species onto N-doped mesoporous carbon for efficient ORR [163]. Combining HAADF-STEM, XAS, Mößbauer spectroscopy analysis, and DFT calculations, they identified that the Fe–N<sub>2</sub> site was the active center for ORR and the catalytic activity was linearly related to the concentration of FeN<sub>2</sub> sites. Compared with FeN<sub>4</sub> sites, the FeN<sub>2</sub> sites exhibited lower ORR overpotential due to a weaker interaction with \*O<sub>2</sub> and \*OH intermediates and improved electron transfer. Lin et al. also found that hierarchically porous single-atom Fe–N–C electrocatalysts with Fe–N<sub>2</sub> sites showed superior electrocatalytic ORR activity with a  $E_{1/2}$  of 0.927 V vs RHE in 0.1 M KOH [164]. DFT simulations uncovered that the Fe–N<sub>2</sub> site exhibited higher ORR activity than the Co–N<sub>2</sub> site due to smaller reaction energy barriers.

Bao et al. synthesized a single-atom Cu-based catalyst (Cu–N<sub>0</sub>C) with 8.5 wt% Cu loading and Cu(I)–N<sub>2</sub> active sites by annealing the mixture of CuPc and dicyandiamide in an inert atmosphere [165]. The Cu–N<sub>0</sub>C exhibited high ORR activity via a main 4e<sup>−</sup> pathway. DFT simulations uncovered that the Cu–N<sub>2</sub> site exhibited higher ORR activity than Cu–N<sub>3</sub>, Cu–N<sub>4</sub> and CuPc due to good adsorption and desorption abilities of O species. The removal of \*OH was the rate-determining step on the Cu–N<sub>2</sub> site, on which a barrier of 0.83 eV should be overcome. Baek et al. anchored atomic Cu onto an ultrathin N-doped carbon (Cu–N–C) with 20.9 wt% Cu content [166]. The Cu–N–C showed higher kinetic current density than Pt/C and N–C. DFT simulations uncovered that the Cu–N<sub>2</sub> site exhibited larger O<sub>2</sub> and OOH adsorption energies than Pt(111). Yao et al. [167] and Wang et al. [168] also reported that the Cu(I)–N<sub>2</sub> active site exhibited excellent ORR performance via a 4e<sup>−</sup>

pathway.

Pennycook et al. reported that an atomic Cu–N–C catalyst exhibited high NH<sub>3</sub> yield rate (53.3 and 49.3  $\mu\text{g}_{\text{NH}_3} \text{ h}^{-1} \text{ mg}_{\text{cat}}^{-1}$  in 0.1 M KOH and 0.1 M HCl, respectively) and Faradaic efficiency (>11%) for electrocatalytic NRR (Fig. 7a-7m) [169]. By calculations, they proposed that the Cu–N<sub>3</sub> and Cu–N<sub>4</sub> sites failed to activate nitrogen, and the Cu–N<sub>2</sub> was the active center for the NRR. The hydrogenation of adsorbed N<sub>2</sub><sup>\*</sup> was the rate-determining step on the Cu–N<sub>2</sub> site with an energy barrier of 1.573 eV via the distal and alternating pathways.

Baek et al. obtained an atomic Zn-based catalyst (ZnNC) by pyrolysis method, which displayed good ORR activity via a main 4e<sup>−</sup> pathway [170]. The O<sub>2</sub> adsorption energy on Zn–N<sub>2</sub> sites is –1.53 eV, which is more negative than that (–0.93 eV) on Pt(111), implying more favorable ORR on the Zn–N<sub>2</sub> sites. The theoretical ORR overpotential on the Zn–N<sub>2</sub> sites was predicted to be 0.4 V.

Guan et al. synthesized an atomically dispersed Sc on N-doped graphene for efficient ORR [171]. During the reaction, O or OH ligands would be coordinated to the Sc–N<sub>x</sub> sites to form Sc–N–O/OH structures because they are more stable and active. DFT simulations uncovered that ScN<sub>2</sub>O and ScN<sub>3</sub>O sites showed much lower ORR overpotential than ScN<sub>4</sub> and ScN<sub>4</sub>OH sites.

#### 4.1.5. M–N<sub>1</sub> configuration

Sun et al. found that atomic Ru on N-doped porous carbon showed outstanding NRR performance with an NH<sub>3</sub> formation rate of 3.665  $\text{mg}_{\text{NH}_3} \text{ h}^{-1} \text{ mg}^{-1}$  Ru at –0.21 V vs. RHE [172]. Theoretical simulations uncovered that the free-energy change at the potential-determining step ( $\Delta G_{\text{PDS}}$ ) of Ru–NC<sub>2</sub> (0.42 eV) was obviously smaller than that of Ru–C<sub>3</sub> (1.28 eV) and Ru–C<sub>4</sub> (1.13 eV). Moreover, the Ru–NC<sub>2</sub> site showed lower free energy for NRR than other Ru–N<sub>x</sub>C<sub>y</sub> sites, i.e. Ru–N<sub>2</sub>C, Ru–N<sub>3</sub>, Ru–NC<sub>3</sub>, Ru–N<sub>2</sub>C<sub>2</sub>, Ru–N<sub>2</sub>C<sub>2</sub>, Ru–N<sub>3</sub>C, and Ru–N<sub>4</sub>, implying that the Ru–NC<sub>2</sub> site was the main active center for NRR.

In addition, Du et al. predicted that the W–N<sub>1</sub> structure exhibited lower theoretical onset potential (0.29 V) than the W–N<sub>2</sub> and W–N<sub>3</sub> structures, suggesting that W/N-codoped graphyne could be active for NRR [173].

## 4.2. M–N<sub>x</sub>S<sub>y</sub> coordination

#### 4.2.1. Ni–N<sub>3</sub>S configuration

Hou et al. found that isolated nickel coordinated with nitrogen and sulfur atoms embedded in porous carbon nanosheets exhibited excellent OER activity with a low overpotential of 0.28 V at 10  $\text{mA cm}^{-2}$  in an

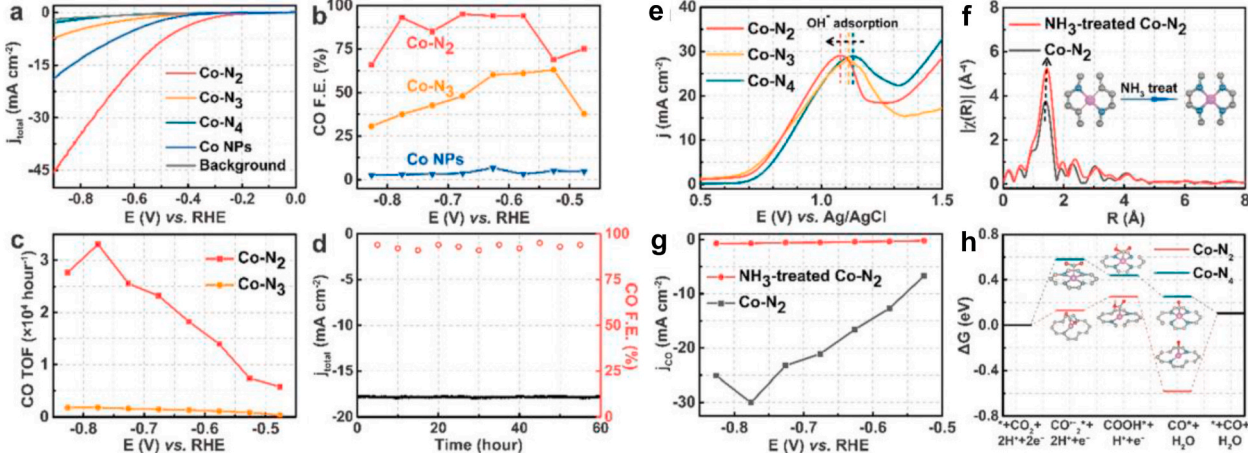


**Fig. 6.** (a) LSV of Co–N<sub>2</sub>, Co–N<sub>3</sub>, Co–N<sub>4</sub>, and Co NPs and pure carbon paper as background. (b) CO Faradaic efficiencies at different applied potentials and (c) corresponding CO TOF for different catalysts. (d) Catalytic stability test at –0.63 V. (e) Single oxidative LSV scans in N<sub>2</sub>-saturated 0.5 M NaOH for different catalysts. (f) EXAFS and (g) CO specific current density for Co–N<sub>2</sub> and NH<sub>3</sub>-treated Co–N<sub>2</sub>. (h) Calculated Gibbs free energy diagrams for CO<sub>2</sub> electroreduction to CO on Co–N<sub>2</sub> and Co–N<sub>4</sub>. Reproduced with permission [159]. Copyright 2018 Wiley-VCH.

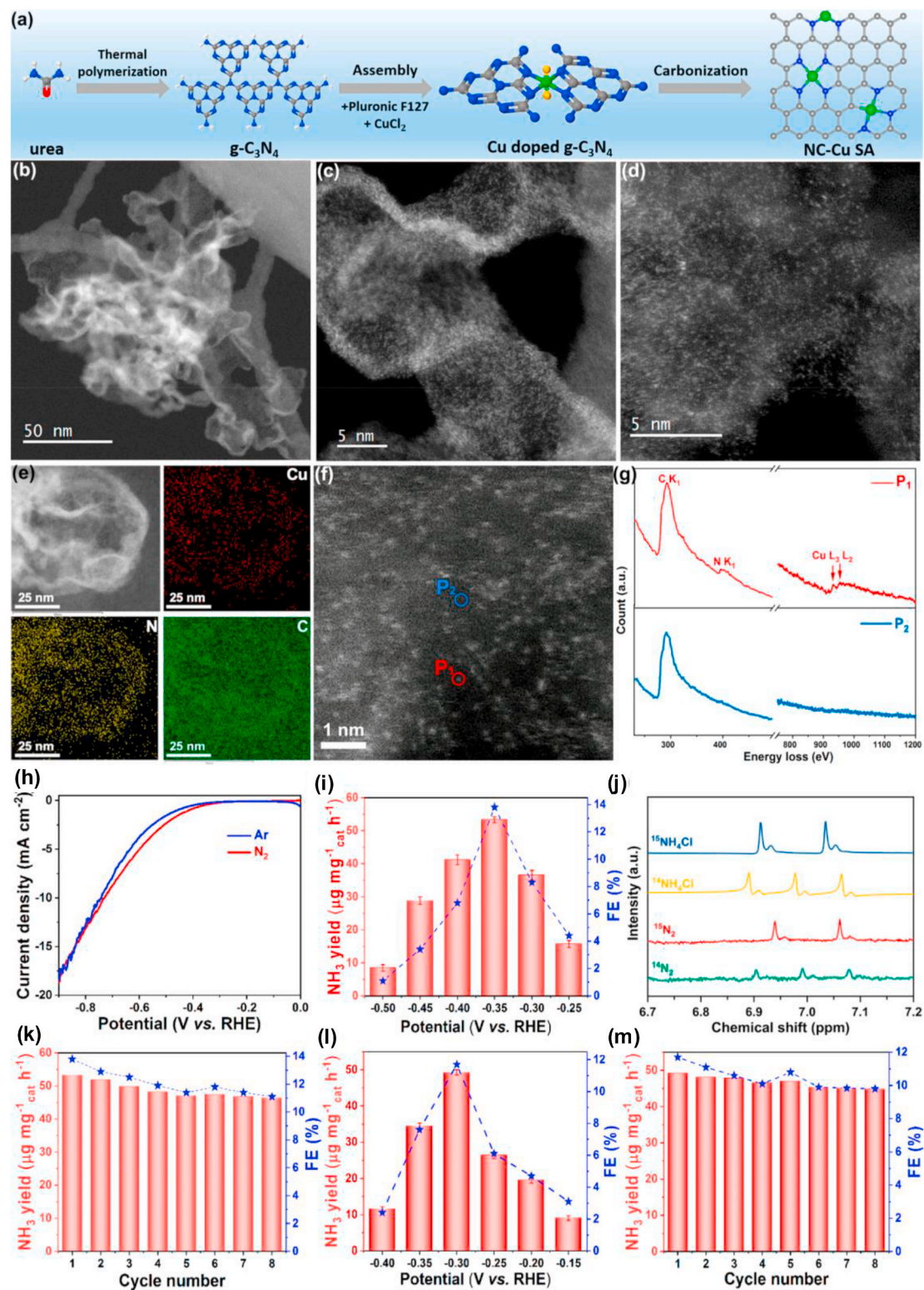


**Fig. 7.** (a) Schematic illustration of the fabrication process of NC-Cu SA. (b–d) HAADF-STEM images. (e) STEM-EDS mappings. (f) Atomic-level HAADF-STEM image and (g) corresponding EEL spectra. (h) LSV curves in 0.1 M KOH. (i) NH<sub>3</sub> yield rate and FE at different potentials. (j) <sup>1</sup>H NMR spectra of the electrode after 12 h of electrochemical reduction using <sup>15</sup>N<sub>2</sub> as the feed gas. (k) NH<sub>3</sub> yield rates with increasing cycle numbers. (l) NH<sub>3</sub> yield rate and FE at different potentials in 0.1 M HCl. (m) NH<sub>3</sub> yield rates with increasing cycle numbers in 0.1 M HCl. Reproduced with permission [169]. Copyright 2019 American Chemical Society.

alkaline medium [8]. By DFT calculations, they found that the theoretical OER overpotential on the Ni–N<sub>3</sub>S, Ni–N<sub>4</sub>, Ni–S, and N–S sites were 0.346, 0.461, 0.478, and 0.516 V, respectively, indicating that the Ni–N<sub>3</sub>S structure was the efficient active site for OER. Since N atoms are more electronegative than S atoms. Compared to the Ni–N<sub>4</sub> structure,

the S atom in the Ni–N<sub>3</sub>S structure can increase the electronic density of the Ni atom, thereby modulating the hybridization states between Ni and linked N atoms.

#### 4.2.2. Fe-N<sub>4</sub>S<sub>2</sub> configuration

Li et al. synthesized different single metal atoms immobilized on porous N,S-codoped carbon matrix and found that the Fe-SAs/NSC catalyst displayed higher ORR activity than Co-SAs/NSC and Ni-SAs/NSC [174]. They found that the FeN<sub>4</sub>S<sub>2</sub> site was formed in Fe-SAs/NSC catalyst where the S atoms were bonded with the N atoms, while CoN<sub>3</sub>S<sub>1</sub> and NiN<sub>3</sub>S<sub>1</sub> sites were generated in Co-SAs/NSC and Ni-SAs/NSC, respectively, where metal–S bonds were formed. DFT simulations uncovered that the FeN<sub>4</sub>S<sub>2</sub> site showed higher ORR activity than the CoN<sub>3</sub>S<sub>1</sub> and NiN<sub>3</sub>S<sub>1</sub> sites owing to larger charge density and smaller energy barriers.

#### 4.3. M–S coordination

Metal-sulfur complexes have been extensively investigated in organic synthesis, since they can cooperatively activate E-H bond (E = H, Si, and B) [175]. In addition, metal-sulfur batteries (e.g. Li-S and Na-S batteries) showed high theoretical energy density, low cost, rechargeability, and environmental friendliness [176]. Transition metal sulfides exhibited catalytic activity for many electrochemical reactions, e.g. HER [177], OER [178,179], ORR [180–182], NRR [183], and CO<sub>2</sub>RR [184]. However, the research on single-site catalysts with metal-sulfur coordination is in its infancy. Choi et al. reported that an atomically dispersed Pt on sulfur-doped carbon exhibited superior ORR performance with a two-electron pathway ( $n = 2.1$ ) for producing H<sub>2</sub>O<sub>2</sub> [185]. The Pt/HSC showed an onset potential of 0.71 V vs. RHE and 96% selectivity to H<sub>2</sub>O<sub>2</sub>. Theoretical simulations uncovered that the Pt<sup>2+</sup> center in the Pt–S<sub>4</sub> site can interact with two water molecules due to strong Lewis basicity of the oxygen lone pairs. The theoretical potential for ORR on the Pt–S<sub>4</sub> site was 0.64 V vs. RHE, which matched with the experimental value approximately, suggesting that the possible active site for 2e<sup>−</sup> ORR should be the Pt–S<sub>4</sub> site. Chen et al. anchored single Cu atoms onto S-doped graphene by an underpotential deposition strategy for efficient alkaline ORR electrocatalysis [186]. The EXAFS and theoretical calculations showed that Cu–O<sub>3</sub>SG configuration was the active structure for ORR, on which a barrier of 0.12 and 0.98 eV needed to be overcome at electrode potential 0 and 0.86 V, respectively.

#### 4.4. M–C coordination

The M–C coordination is usually unstable under harsh oxidation conditions due to the oxidation and breakage of the M–C bonds. Therefore, catalysts with M–C structure can usually be used in reduction reactions. For example, Wu et al. synthesized porous molybdenum carbide octahedral nanoparticles, which showed excellent HER activity in both acidic and alkaline media with overpotentials ( $\eta_{10}$ ) of 142 and 151 mV, respectively [187]. Wang and co-workers supported molybdenum carbide nanodots onto ultrathin carbon nanosheets, on which a moderate NH<sub>3</sub> yield rate (11.3 µg h<sup>−1</sup> mg<sup>−1</sup><sub>Mo2C</sub>) and Faradic efficiency (7.8%) can be achieved in 0.5 M Li<sub>2</sub>SO<sub>4</sub> (pH = 2) for NRR [188]. However, there are seldom reports about experimental results of SACs with M–C coordination for electrocatalytic applications. Wang et al. predicted theoretically that atomically dispersed W onto graphene demonstrated good NRR performance with a low onset potential of 0.25 V [189]. Compared with Nb–C<sub>3</sub>, Re–C<sub>3</sub>, V–C<sub>2</sub>N<sub>1</sub>, Zr–C<sub>2</sub>N<sub>1</sub>, Nb–C<sub>2</sub>N<sub>1</sub>, Mo–C<sub>2</sub>N<sub>1</sub>, Ru–C<sub>2</sub>N<sub>1</sub>, V–C<sub>1</sub>N<sub>3</sub>, and V–N<sub>4</sub>, the W–C<sub>3</sub> structure exhibited lower onset potential for NRR. In addition, the NRR was more selective on the W–C<sub>3</sub> site than the competing HER.

#### 4.5. M–O coordination

Zheng and coworkers demonstrated that atomic Cu substituted CeO<sub>2</sub> exhibited a methane faradaic efficiency of ~58% at −1.8 V vs RHE for electrochemical CO<sub>2</sub>RR [190]. Theoretical simulations uncovered that isolate Cu site with three oxygen vacancies was the active center for CO<sub>2</sub> adsorption and activation. However, the catalyst showed relatively low

current density due to poor electrical conductivity of the CeO<sub>2</sub> support. Zhao et al. used DFT simulations to study the CO<sub>2</sub>RR performance on isolated-Rh/TiO<sub>2</sub> [191]. They found that CO<sub>2</sub> and H<sub>2</sub> co-adsorbed on the Rh site can react with each other to generate CO and prevent further H<sub>2</sub> adsorption for hydrogenation of CO.

Zhao et al. anchored isolated Fe onto nitrogen-free lignocellulose-derived carbon with Fe-(O-C<sub>2</sub>)<sub>4</sub> coordination configuration, which exhibited a NH<sub>3</sub> yield rate of 307.7 µg h<sup>−1</sup> mg<sup>−1</sup><sub>cat</sub> and a high faradaic efficiency of 51.0% for electrocatalytic NRR [192]. Theoretical calculations revealed that the Gibbs free energy for N<sub>2</sub> adsorption on the Fe-(O-C<sub>2</sub>)<sub>4</sub> site via the end-on and side-on routes was −0.79 and −0.78 eV, respectively, implying that the two adsorption modes were thermodynamically feasible. For N<sub>2</sub> adsorption, the electrons were transferred from Fe to N<sub>2</sub> via a back-donation mechanism.

Xu et al. anchored isolated Pt onto the defects of reducible MoO<sub>3-x</sub> by a plasmon resonance, which showed comparable HER activity with commercial Pt/C [193]. The bond length of Pt–O coordination is 0.2 nm. Wang et al. prepared in-situ atomic CoO<sub>x</sub> by plasma treatment of a metal-organic framework ZIF-67 with enhanced OER activity [194]. The large surface area and pores of ZIF-67 favored mass transport during the reaction. Zhang and coworkers synthesized Co-TiO<sub>2</sub> nanorods with isolated single-site Co, which showed an overpotential of 332 mV at 10 mA cm<sup>−2</sup> in 1 M KOH for OER [195]. Moreover, Co-TiO<sub>2</sub> exhibited higher OER activity than Ni-TiO<sub>2</sub>, Fe-TiO<sub>2</sub>, Cu-TiO<sub>2</sub>, and Mn-TiO<sub>2</sub>.

#### 4.6. Dual-metal sites

##### 4.6.1. Fe–Fe dual-metal sites

By precisely adjusting the number of Fe atoms in clusters anchored on N-doped carbon, Xiong et al. found that Fe<sub>2</sub> clusters on N-doped carbon exhibited good ORR activity with an E<sub>1/2</sub> of 0.78 V vs. RHE in 0.5 M H<sub>2</sub>SO<sub>4</sub> [196]. After cycling for 20000 times, the half-wave potential shifted negatively of 20 mV. By theoretical simulations, they revealed that oxygen molecule was adsorbed on Fe<sub>1</sub>–N–C via a superoxo-like mode, while it was adsorbed on Fe<sub>2</sub>–N–C and Fe<sub>3</sub>–N–C via a peroxy-like mode due to shorter atom distance than the Fe<sub>1</sub>–N–C site. The adsorption energy for oxygen molecule on Fe<sub>1</sub>–N–C, Fe<sub>2</sub>–N–C, and Fe<sub>3</sub>–N–C was 1.38, 3.10, and 3.17 eV, respectively, implying that oxygen molecule was favorably adsorbed on Fe<sub>2</sub>–N–C and Fe<sub>3</sub>–N–C. Compared with Fe<sub>3</sub>–N–C, Fe<sub>2</sub>–N–C could afford more catalytic sites for ORR, thus showing higher ORR activity.

##### 4.6.2. Fe–Co dual-metal sites

In nature, the oxygen-evolving center (a Mn<sub>4</sub>CaO<sub>5</sub> cluster) and heme–copper oxidases are responsible for the oxidation of H<sub>2</sub>O to O<sub>2</sub> and reduction of O<sub>2</sub> to H<sub>2</sub>O, respectively [197,198]. Inspired by these binuclear active centers, different types of dual-metal–N<sub>x</sub> active sites incorporated within carbon materials were synthesized for electrocatalytic reactions. Hu et al. adopted operando X-ray absorption spectroscopy to investigate the structure change of a single-atom catalyst Co–N–C during OER in alkaline media with and without Fe<sup>3+</sup> [10]. They found that the OER activity increased after activation in the presence of Fe<sup>3+</sup> and a dimeric Co–Fe moiety would be formed, which should be the active site for OER.

Li et al. fabricated Fe–Co dual sites onto N-doped porous carbon, showing outstanding ORR activity with a positive E<sub>1/2</sub> of 0.863 V vs. RHE in acidic media (Fig. 8a–j) [28]. The H<sub>2</sub>/O<sub>2</sub> fuel cell with (Fe, Co)/N–C as cathodic catalyst can afford maximum power densities of ~0.85 and 0.98 Wcm<sup>−2</sup> at back pressures of 0.1 and 0.2 MPa, respectively. According to DFT calculations, the cleavage barrier of O–O bond can be decreased on the Fe/Co-dual-metal sites, thus accelerating ORR kinetics (Fig. 8k). In addition, Sun and coworkers found that an atomic Fe/Co–N–C catalyst exhibited higher ORR activity in both basic and acidic media than commercial 20 wt% Pt/C [199].

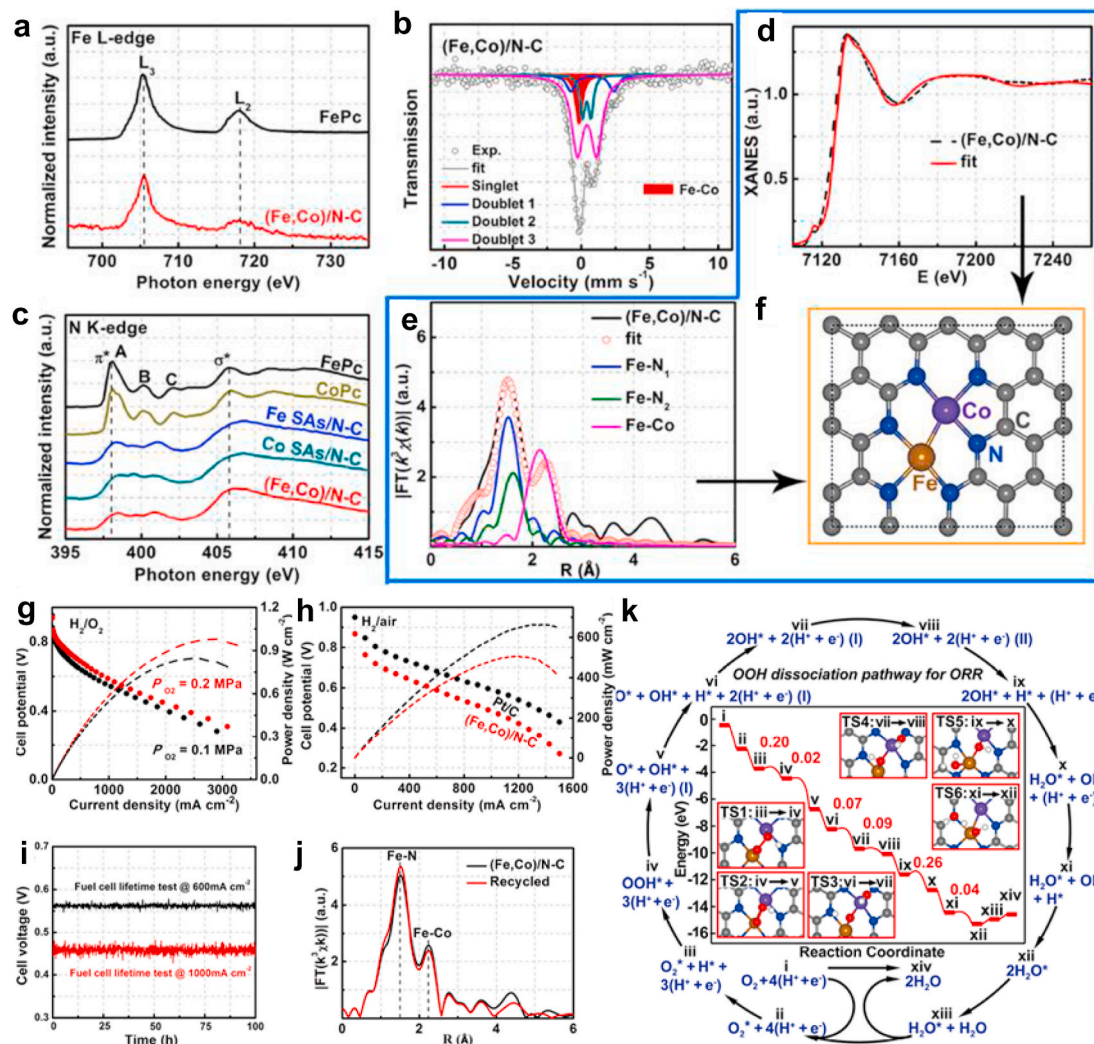


**Fig. 8.** (a) Fe L-edge XANES spectra of (Fe,Co)/N-C and FePc. (b) <sup>57</sup>Fe Mössbauer transmission spectra. (c) N K-edge XAS spectra. (d) Fe K-edge XANES spectra. (e) Fe K-edge EXAFS. (f) Proposed architectures of Fe-Co dual sites. (g) H<sub>2</sub>/O<sub>2</sub> fuel cell polarization plots. (h) H<sub>2</sub>/air fuel cell polarization plots. (i) Stability of (Fe,Co)/N-C in a H<sub>2</sub>/air fuel cell measured at 600 mA cm<sup>-2</sup> and 1000 mA cm<sup>-2</sup>. (j) Fe K-edge EXAFS fitting curves of (Fe,Co)/N-C and (Fe,Co)/N-C after stability test. (k) Energies of intermediates and transition states in mechanism of ORR at (Fe,Co)/N-C from DFT. Reproduced with permission [28]. Copyright 2019 American Chemical Society.

#### 4.6.3. Fe–Ni dual-metal sites

Sun et al. immobilized atomic Ni–Fe dual-metal sites onto polymeric carbon nitride, which displayed a low overpotential of 310 mV at 10 mA cm<sup>-2</sup> for alkaline OER. A cooperation mechanism between Fe and adjacent Ni site contributed to a low energy barrier (0.1 eV at a potential of 1.58 V). Specifically speaking, the first and second steps (adsorption of OH<sup>\*</sup> and O<sup>\*</sup>) of OER should occur on the Fe site, while the third step (formation of OOH<sup>\*</sup>) would take place on the Ni site, leading to a low energy barrier [200]. In addition, by theoretical calculations, Pei et al. disclosed that the ORR activity of atomic dual-metal Fe–Ni catalysts can be improved by the modification with hydroxyl groups [201]. Moreover, due to excellent ORR performance on Fe–N<sub>4</sub> sites and superior OER activity on Ni–N<sub>4</sub> sites, Ma et al. constructed Ni–N<sub>4</sub>/GHSs/Fe–N<sub>4</sub> Janus catalyst for bifunctional OER/ORR electrocatalysis [202]. The assembled rechargeable Zn–air battery showed large specific capacity of 777.6 Ah Kg<sub>Zn</sub><sup>-1</sup>, high energy density of 970.4 Wh kg<sub>Zn</sub><sup>-1</sup>, and good cycling stability.

#### 4.6.4. Fe–Mn dual-metal sites

Chen et al. fabricated dual-metal Fe–Mn sites onto N-doped porous carbon, which exhibited superior ORR performance with a positive E<sub>1/2</sub>

of 0.904 V vs. RHE and high kinetic current density of 33.33 mA cm<sup>-2</sup> in 0.1 M KOH [198]. DFT simulations uncovered that the potential-determining step of ORR on the Fe, Mn–N/C was the protonation of O<sup>\*</sup> with an energy barrier of 0.22 eV, much smaller than that on Fe–N/C (0.36 eV) and the energy barrier for O<sub>2</sub> hydrogenation to OOH<sup>\*</sup> on Mn–N/C (0.50 eV), suggesting a synergistic action between Mn and Fe–N/C for enhanced ORR performance. Dey et al. anchored Fe–Mn dual-metal sites onto N-doped fish gill derived carbon (Fe,Mn,N-FGC) by high-temperature pyrolysis of the mixture of FeCl<sub>3</sub>, MnCl<sub>2</sub>, melamine, and crushed fish gill, and subsequent acid leaching [203]. The bond length of Fe–Mn path was 0.225 nm, slightly shorter than that (0.230 nm) of Fe–Fe path as revealed by XAS analysis. The valence states of Fe and Mn in the Fe,Mn,N-FGC were both +2 and the coordination configuration was N<sub>3</sub>Fe–MnN<sub>3</sub>. The Fe,Mn,N-FGC showed a positive E<sub>1/2</sub> of 0.89 V in 0.1 M KOH, 0.74 V in 0.5 M H<sub>2</sub>SO<sub>4</sub>, and 0.86 V in 0.1 M PBS for ORR. When Mn<sup>2+</sup> was coupled with Fe<sup>2+</sup>, the π–interaction for Mn<sup>2+</sup> would be reinforced owing to the π–π repulsion, which stabilized the 3C-2e bond and facilitated O<sub>2</sub> adsorption on the Fe–Mn sites.

#### 4.6.5. Fe–Cu dual-metal sites

Chen et al. anchored Fe–Cu dual atomic sites onto porous N-doped

carbon for efficient  $4e^-$  ORR with an  $E_{1/2}$  of 0.86 V in 0.1 M KOH [204]. The local electron density of the Fe–N<sub>4</sub> sites can be increased by electron transfer from Cu–N<sub>4</sub> sites, thus facilitating ORR kinetics.

Liang et al. annealed the mixture of FeCl<sub>2</sub>, CuCl<sub>2</sub>, dicyandiamide, and multiwalled carbon nanotubes to obtain a dual-metal site catalyst CNT@C<sub>3</sub>N<sub>4</sub>–Fe&Cu with 34% Faradic efficiency for electrocatalytic NRR [205]. There were two kinds of existence state for the Fe/Cu species, i.e. metal clusters and single atoms as revealed by STEM and XAS analysis. Theoretical calculations revealed that reveal that the coordination between Cu and Fe favored the adsorption and activation of N<sub>2</sub> with a low energy barrier, thus facilitating NRR.

#### 4.6.6. Fe–Rh dual-metal sites

Wang et al. found that a Fe–Rh interbond can be formed by capturing mobile Rh on the FeN<sub>4</sub> structure [206]. The atomic Rh–Fe catalyst displayed overpotential of 36 mV at 10 mA cm<sup>-2</sup> for acidic HER. The atomically dispersed Fe cannot serve as the active site, but modulate the charge distribution of the Fe–Rh catalyst. By DFT simulations, Zhao et al. predicted that dual atomic FeRh immobilized into N-doped graphene showed lower overpotential (0.22 V) than atomic Fe–Fe, Fe–Co, Fe–Ni, Fe–Cu, Fe–Rh, Fe–Ru, Fe–Pd, Fe–Mo, Mo–Co, Mo–Cu, Mo–Ru, and Mo–Mo immobilized into N-doped graphene for electrocatalytic NRR [207].

#### 4.6.7. Co–Ni dual-metal sites

Zhang et al. anchored atomic Co/Ni dual-metal sites onto N-doped porous carbon for bifunctional oxygen electrocatalysis [208]. The atomic Co/Ni–N–C catalyst exhibited half-wave potentials of 0.84 and 0.73 V for ORR in alkaline and acidic media, respectively, and an overpotential of 0.36 V at 10 mA cm<sup>-2</sup> for alkaline OER. Compared with atomic Co–N–C system, the N-atoms in the Co/Ni–N–C system gained more electrons, indicating that the Ni–N bonds have covalent character and the electrocatalytic activity of N atoms can be improved.

#### 4.6.8. Co–Pt dual-metal sites

Yao et al. fabricated atomic Pt–Co dual sites on N-doped carbon by electrochemical deposition of Pt<sup>2+</sup> onto the Co–NC, which exhibited a  $4e^-$  ORR, different from  $2e^-$  pathway on atomic Pt catalysts [9]. The most energetically favorable configuration is a(Co–Pt)@N8V4 (N8: the number of nitrogen atoms, V4: the number of vacant carbon atoms), which exhibited an ORR overpotential of 0.30 V, much lower than a (Pt–Pt)@N8V4 (1.07 V). The asymmetric electron distribution around the Pt/Co sites led to strong binding effect between a(Co–Pt)@N8V4 and O<sub>2</sub>.

#### 4.6.9. Pt–Pt dual-metal sites

Lu et al. fabricated Pt<sub>2</sub><sup>δ+</sup> dimers on graphene by atomic layer deposition, which exhibited a specific rate of 2800 mol<sub>H2</sub> mol<sub>Pt</sub><sup>-1</sup> min<sup>-1</sup> for HER, much better than single Pt atoms and nanoparticles supported on graphene [209]. DFT simulations uncovered that H<sub>2</sub> was dissociatively adsorbed on Pt<sub>1</sub>/graphene-R, while molecularly on Pt<sub>2</sub>/graphene-R with a moderate adsorption energy, favoring H<sub>2</sub> desorption.

### 5. Perspectives about SACs for HER, ORR, OER, CO<sub>2</sub>RR, and NRR

The electrocatalytic HER performance on various SACs is listed in Table 1. Single-atom Fe-, Co-, Ni-, Mo-, W-, Ru-, Ir-, and Pt-based catalysts exhibit good HER activity. The optimal configuration for HER on Fe-based, Co-based, Ir-based, and Pt-based SACs might be M–N<sub>4</sub> structure, while the optimal configuration for Mo-based SACs and W-based SACs might be Mo–N<sub>1</sub>C<sub>2</sub> and W–N<sub>1</sub>C<sub>3</sub>, respectively. The electrocatalytic OER performance on various SACs is summarized in Table 2. Co-, Ni-, Mn-, Ru-, Ir-, and Au-based SACs can efficiently catalyze OER and the M–N<sub>4</sub> configuration is the favorable structure for most SACs to lower reaction barriers. Table 3 shows the ORR performance on various SACs. It can be found that most SACs with the M–N<sub>4</sub> moiety are active for

**Table 1**

Electrocatalytic performance of SACs towards HER.

Catalyst	Active site	Electrolyte	$\eta @ 10$ mA cm <sup>-2</sup> (mV)	Tafel slope (mV dec <sup>-1</sup> )	Ref.
Fe–N <sub>4</sub> SAs/NPC	Fe–N <sub>4</sub>	1 M KOH	202	123	[210]
Co@NG	Co–N <sub>x</sub>	0.1 M KOH	172	42.5	[41]
Co@NG	Co–N <sub>x</sub>	0.5 M H <sub>2</sub> SO <sub>4</sub>	182	49.3	[41]
Co-SAS/ HOPNC	Co–N <sub>4</sub>	0.5 M H <sub>2</sub> SO <sub>4</sub>	137	52	[40]
CoSAs/ PTF-600	Co–N <sub>4</sub>	0.5 M H <sub>2</sub> SO <sub>4</sub>	94	50	[44]
Co-SAC	Co–N <sub>4</sub>	0.5 M H <sub>2</sub> SO <sub>4</sub>	230	99	[53]
Ni-SAC	Ni–N <sub>4</sub>	0.5 M H <sub>2</sub> SO <sub>4</sub>	590	167	[53]
Ru@NG- 750	Ru–N <sub>4</sub>	1 M KOH	40	35.9	[211]
Ru@NG- 750	Ru–N <sub>4</sub>	0.5 M H <sub>2</sub> SO <sub>4</sub>	90	–	[211]
Ru-NC-700	Ru–C <sub>2</sub> N <sub>2</sub>	1 M KOH	12	–	[212]
Ru-NC-700	Ru–C <sub>2</sub> N <sub>2</sub>	0.1 M KOH	47	14	[212]
Ru-NC-700	Ru–C <sub>2</sub> N <sub>2</sub>	0.5 M H <sub>2</sub> SO <sub>4</sub>	29	28	[212]
Ir@NG- 750	Ir–N <sub>4</sub>	0.5 M H <sub>2</sub> SO <sub>4</sub>	25	15	[149]
Mo <sub>1</sub> N <sub>1</sub> C <sub>2</sub>	Mo–N <sub>1</sub> C <sub>2</sub>	0.1 M KOH	132	90	[213]
Mo <sub>1</sub> N <sub>1</sub> C <sub>2</sub>	Mo–N <sub>1</sub> C <sub>2</sub>	0.5 M H <sub>2</sub> SO <sub>4</sub>	154	–	[213]
W-SAC	W–N <sub>1</sub> C <sub>3</sub>	0.1 M KOH	85	53	[214]
W-SAC	W–N <sub>1</sub> C <sub>3</sub>	0.5 M H <sub>2</sub> SO <sub>4</sub>	105	58	[214]
W-SAC	W–N <sub>4</sub>	0.5 M H <sub>2</sub> SO <sub>4</sub>	530	122	[53]
Pt <sub>1</sub> /NPC	Pt–N <sub>4</sub>	0.5 M H <sub>2</sub> SO <sub>4</sub>	25	28	[154]
Pt <sub>1</sub> /MC	Pt–N <sub>x</sub>	0.5 M H <sub>2</sub> SO <sub>4</sub>	–	26	[215]
FR-NCS	FeN <sub>4</sub> –RhN <sub>1</sub> C <sub>2</sub>	0.5 M H <sub>2</sub> SO <sub>4</sub>	~24	26	[206]

**Table 2**

Electrocatalytic performance of SACs towards OER.

Catalyst	Active site	Electrolyte	$\eta @ 10$ mA cm <sup>-2</sup> (mV)	Tafel slope (mV dec <sup>-1</sup> )	Ref.
Fe–N <sub>4</sub> SAs/NPC	Fe–N <sub>4</sub>	1 M KOH	430	95	[210]
Fe@NG-750	Fe–N <sub>4</sub>	1 M KOH	194	63	[106]
FeN <sub>x</sub> -embedded PNC	Fe–N <sub>x</sub>	0.1 M KOH	395	80	[104]
Fe-NSDC	Fe–N <sub>3</sub> S	0.1 M KOH	410	59	[216]
Co@NG-750	Co–N <sub>4</sub>	1 M KOH	386	73	[72]
UNT Co SAs/N-C	Co–N <sub>4</sub>	1 M KOH	380	70	[71]
CoSAs@CNTs	Co–N <sub>4</sub>	1 M KOH	410	85	[217]
CoN <sub>4</sub> /NG	Co–N <sub>4</sub>	0.1 M KOH	380	81	[70]
SCoNC	Co–N <sub>4</sub>	0.1 M KOH	310	74	[73]
S NiN <sub>x</sub> -PC/EG	S Ni–N <sub>x</sub>	1 M KOH	280	45	[8]
Ni-NHGF	Ni–N <sub>4</sub>	1 M KOH	331	63	[127]
Mn-NG	Mn–N <sub>4</sub>	1 M KOH	337	55	[6]
Ru@NG-750	Ru–N <sub>4</sub>	1 M KOH	372	68	[211]
Ir@NG-750	Ir–N <sub>4</sub>	1 M KOH	273	64	[149]
Au <sub>1</sub> N <sub>x</sub> /C <sub>3</sub> N <sub>4</sub>	Au–N <sub>x</sub>	0.1 M KOH	450	112	[218]
Ni <sub>0.65</sub> Fe <sub>0.35</sub> @PCN	NiFe–N <sub>x</sub>	1 M KOH	310	38	[200]
Co–Fe–N–C	CoFe	1 M KOH	309	37	[10]

electrocatalytic ORR, while for Cu-SACs, and W-SACs, the Cu–N<sub>2</sub> configuration and W–N<sub>5</sub> configuration could be better. For electrochemical NRR, M–N<sub>2</sub> or M–N<sub>3</sub> structures might be more active than the M–N<sub>4</sub> structure (Table 4). For electrocatalytic CO<sub>2</sub>RR, Fe-based and Ni-based SACs with M–N<sub>4</sub> configuration are active and selective to form

**Table 3**  
Electrocatalytic performance of SACs towards ORR.

Catalyst	Active site	Electrolyte	E <sub>onset</sub> (V vs. RHE)	E <sub>1/2</sub> (V vs. RHE)	Ref.
Fe-NCC	Fe-N <sub>x</sub>	0.1 M KOH	0.93	0.82	[219]
Fe–N–C HNSs	Fe–N <sub>4</sub>	0.1 M KOH	1.046	0.87	[220]
C-FeHZ8@g-C <sub>3</sub> N <sub>4</sub>	Fe–N <sub>4</sub>	0.1 M HClO <sub>4</sub>	–	0.78	[78]
C-FeHZ8@g-C <sub>3</sub> N <sub>4</sub>	Fe–N <sub>4</sub>	0.1 M KOH	–	0.845	[78]
FeN <sub>4</sub> /HOPC	Fe–N <sub>4</sub>	0.5 M H <sub>2</sub> SO <sub>4</sub>	–	0.80	[221]
Fe SAs/N–C	Fe–N <sub>4</sub>	0.1 M KOH	–	0.91	[77]
Fe–N <sub>x</sub> ISAs/GHSS	Fe–N <sub>x</sub>	0.1 M KOH	1.05	0.87	[85]
Fe–N–C–900	Fe–N <sub>2</sub>	0.1 M KOH	0.99	0.927	[164]
Fe-NSDC	Fe–N <sub>3</sub>  S	0.1 M KOH	0.96	0.84	[216]
Fe–N–C900	Fe–N <sub>x</sub>	0.1 M KOH	1.09	0.908	[46]
Fe–N–C900	Fe–N <sub>x</sub>	0.5 M H <sub>2</sub> SO <sub>4</sub>	0.962	0.795	[46]
FeN <sub>x</sub> -embedded PNC	Fe–N <sub>x</sub>	0.1 M KOH	0.997	0.86	[104]
Fe SAC/N–C	Fe–N <sub>5</sub>	0.1 M KOH	–	0.809	[47]
C-FePc(CN) <sub>8</sub> /ZIF-8	Fe–N <sub>x</sub>	0.1 M HClO <sub>4</sub>	–	0.811	[222]
C-FePc(CN) <sub>8</sub> /ZIF-8	Fe–N <sub>x</sub>	0.1 M KOH	–	0.91	[222]
Fe–N–BCNT#BP	Fe–N <sub>x</sub>	0.1 M KOH	1.03	0.90	[223]
Fe–N <sub>4</sub> SAs/NPC	Fe–N <sub>4</sub>	0.1 M KOH	0.972	0.885	[210]
Co SAs/N–C (900)	Co–N <sub>x</sub>	0.1 M KOH	0.982	0.881	[60]
20Co-NC-1100	Co–N <sub>4</sub>	0.5 M H <sub>2</sub> SO <sub>4</sub>	0.93	0.80	[65]
Co–N–C@F127	Co–N <sub>4</sub>	0.5 M H <sub>2</sub> SO <sub>4</sub>	0.93	0.84	[66]
CoSAs@CNTs	Co–N <sub>4</sub>	0.1 M KOH	0.99	0.86	[217]
Co <sub>3</sub> N <sub>4</sub> /NG	Co–N <sub>4</sub>	0.1 M KOH	0.98	0.87	[70]
Co-SAs/HOPNC	Co–N <sub>4</sub>	0.1 M KOH	–	0.89	[40]
CoSAs/PTF	Co–N <sub>4</sub>	0.1 M KOH	–	0.808	[44]
Co@NG-750	Co–N <sub>x</sub>	0.1 M KOH	0.97	0.87	[41]
Co@NG-750	Co–N <sub>x</sub>	0.5 M H <sub>2</sub> SO <sub>4</sub>	0.79	0.69	[41]
UNT Co SAs/N–C	Co–N <sub>4</sub>	0.1 M KOH	0.97	0.89	[71]
SCoNC	Co–N <sub>4</sub>	0.1 M KOH	–	0.91	[73]
20Mn-NC-second	Mn–N <sub>4</sub>	0.5 M H <sub>2</sub> SO <sub>4</sub>	–	0.80	[131]
Mn@NG	Mn–N <sub>4</sub>	0.1 M KOH	0.95	0.82	[132]
Cu SAC	Cu <sup>+</sup> –N <sub>4</sub>	0.1 M KOH	0.97	0.81	[140]
Cu@NG-750	Cu–N <sub>x</sub>	0.1 M KOH	0.94	0.84	[224]
Cu–C–N	Cu–N <sub>2</sub>	0.1 M KOH	0.96	0.869	[166]
Zn–N–C	Zn–N <sub>4</sub>	0.1 M HClO <sub>4</sub>	–	0.746	[145]
Zn–N–C	Zn–N <sub>4</sub>	0.1 M KOH	–	0.873	[145]
ZnNCs	Zn–N <sub>2</sub>	0.1 M KOH	–	0.857	[170]
Cr/N/C SACs	Cr–N <sub>4</sub>	0.1 M HClO <sub>4</sub>	–	0.773	[225]
Sc@NG-750	Sc–N <sub>2</sub> O	0.1 M KOH	0.99	0.89	[171]
SW-N-C	W–N <sub>5</sub>	0.1 M HClO <sub>4</sub>	0.87	0.77	[50]
SW-N-C	W–N <sub>5</sub>	0.1 M KOH	1.01	0.88	[50]
Ir–SAC	Ir–N <sub>4</sub>	0.1 M HClO <sub>4</sub>	0.97	0.864	[226]
Ru–SSC	Ru–N <sub>4</sub>	0.1 M HClO <sub>4</sub>	0.92	0.824	[148]
Ru@NG-750	Ru–N <sub>4</sub>	0.1 M HClO <sub>4</sub>	0.893	0.723	[211]
Ru@NG-750	Ru–N <sub>4</sub>	0.1 M KOH	0.945	0.826	[211]
Au <sub>1</sub> N <sub>x</sub> /C <sub>3</sub> N <sub>4</sub>	Au–N <sub>x</sub>	0.1 M KOH	–	0.76	[218]
f-FeCoNC900	FeN <sub>3</sub> –CoN <sub>3</sub>	0.1 M KOH	1.05	0.89	[199]
FeCoN <sub>x</sub> /C	FeCoN <sub>5</sub> –OH	0.1 M HClO <sub>4</sub>	1.02	0.86	[227]
(Fe,Co)/N–C	FeN <sub>3</sub> –CoN <sub>3</sub>	0.1 M HClO <sub>4</sub>	1.06	0.863	[28]
Fe,Mn,N-FGC	FeN <sub>3</sub> –MnN <sub>3</sub>	0.1 M HClO <sub>4</sub>	1.03	0.89	[203]
Fe, Mn–N/C-900	Fe–N <sub>x</sub> , Mn–N <sub>x</sub>	0.1 M KOH	–	0.904	[198]
A-CoPt-NC	PtCo–N <sub>8</sub> V <sub>4</sub>	0.1 M KOH	–	0.96	[9]

**Table 4**  
Electrocatalytic performance of SACs towards NRR.

Catalyst	Active site	Electrolyte	FE (%)	NH <sub>3</sub> Yield rate (μg NH <sub>3</sub> mg <sup>-1</sup> h <sup>-1</sup> )	Partial current density (mA cm <sup>-2</sup> )	Ref.
Ru SAs/N–C	Ru–N <sub>3</sub>	0.05 M H <sub>2</sub> SO <sub>4</sub>	29.6	120.9	0.13	[158]
Ru <sub>1</sub> /N–C	Ru–N <sub>x</sub>	0.1 M HCl	~7.5	3.665	0.15	[172]
Fe <sub>5</sub> A–N–C	Fe–N <sub>x</sub>	0.1 M KOH	56.55	~7.5	–	[120]
Fe <sub>1</sub> /N–C	Fe–N <sub>x</sub>	0.1 M HCl	4.51	1.56 × 10 <sup>-11</sup>	–	[228]
Fe–N/C–CNTs	Fe–N <sub>3</sub>	0.1 M KOH	9.28	34.83	~0.07	[229]
NC–Cu SA	Cu–N <sub>2</sub>	0.1 M KOH	13.8	~53.3	~0.083	[169]
NC–Cu SA	Cu–N <sub>2</sub>	0.1 M HCl	11.7	~49.3	~0.076	[169]

CO, while Co-based SACs with M–N<sub>4</sub> configuration selective to produce CH<sub>3</sub>OH (Table 5). For Cu-based SACs, the Cu–N<sub>2</sub> configuration might be more selective to generate CO than Cu–N<sub>4</sub> structure.

## 6. Summary and outlook

The geometric and electronic structures of atomically dispersed catalysts can be modulated by different coordination strategies. Unlike flexible sites of homogeneous molecular complexes, the metal sites in SACs are partially restricted by the support, which endows them better stability but higher geometric restriction for macromolecular reactions. Therefore, SACs have been frequently investigated in catalytic reactions with small molecules, especially in electrochemical HER, ORR, OER, CO<sub>2</sub>RR, and NRR. Owing to moderate adsorption-desorption capacity of reaction intermediates on isolated metal sites coordinated with nitrogen atoms, single-atom M–N–C catalysts demonstrate lower energy barrier and higher catalytic activity than metal nanoparticles supported on carbon materials for many reactions, especially for electrocatalytic ORR. The electrocatalytic activity and chemoselectivity can be modulated by tuning coordination atoms and their number. For instance, the M–N<sub>4</sub>C<sub>x</sub> (M = Fe, Co, Mn, etc.) structures show a 4e<sup>–</sup> ORR mechanism, while the Pt–S<sub>4</sub>C<sub>x</sub> structure exhibits a 2e<sup>–</sup> ORR pathway. For electrochemical CO<sub>2</sub>RR and NRR, it is crucial to restrain competitive HER and improve the selectivity to target product. SACs with consistent coordination environment show excellent selectivity and promising applications in these important reactions.

Although great progress has been made in the development of SACs for electrochemical redox reactions, there are some important issues to be addressed for further applications. The uppermost problem is the unsatisfactory stability of SACs during harsh electrocatalytic redox conditions. Although SACs demonstrate unexpected thermostability due to the strong interaction with support without Ostwald ripening phenomenon, such a situation could be changed during the electrocatalytic processes because the metal-ligand bonds can be weakened and even broken after adsorption and desorption of intermediates, especially attack by O-containing species. Two strategies can be considered for addressing this issue. One efficient way is fabrication of more stable metal-ligand bonds to avoid the breakage. For instance, single-atom Mn–N–C catalysts are more stable than Fe–N–C and Co–N–C catalysts for ORR because the Mn–N bond is more resistant to the attack of H<sub>2</sub>O<sub>2</sub> than the Fe–N and Co–N bonds. Another effective way is to synthesize SACs with dual-metal sites since the cooperative effect between two metal sites can reduce the attack and destruction of metal-ligand bonds during electrocatalysis process.

In addition, the controllable synthesis of SACs is still a great challenge, although many synthetic methods of SACs have been developed.

**Table 5**Electrocatalytic performance of SACs towards CO<sub>2</sub>RR.

Catalyst	Active site	Electrolyte	Product	FE (%)	Overpotential (V)	Current density (mA cm <sup>-2</sup> )	Ref.
Mn–N–C	Mn–N <sub>x</sub>	0.1 M KHCO <sub>3</sub>	CO	~80	0.45	~3	[230]
Fe–N–C	Fe–N <sub>x</sub>	0.1 M KHCO <sub>3</sub>	CO	~80	0.5	~4	[230]
Fe/NG-750	Fe–N <sub>4</sub>	0.1 M KHCO <sub>3</sub>	CO	80	0.47	~2.7	[113]
Fe–N <sub>4</sub> /CF-1000	Fe–N <sub>4</sub>	0.5 M KHCO <sub>3</sub>	CO	94.9	0.4	~3	[231]
Fe <sup>3+</sup> –N–C	Fe–N <sub>4</sub>	0.5 M KHCO <sub>3</sub>	CO	>90	0.34	~104	[232]
Fe–N–C	Fe–N <sub>4</sub>	0.5 M KHCO <sub>3</sub>	CO	93.5	0.4	~6	[233]
FeN <sub>5</sub> SAC	Fe–N <sub>5</sub>	0.1 M KHCO <sub>3</sub>	CO	97	0.35	~5	[234]
Co–N <sub>5</sub> /HNPCSSs	Co–N <sub>5</sub>	0.2 M NaHCO <sub>3</sub>	CO	>99	0.63	6.2	[235]
CoPPc/CNT	Co–N <sub>x</sub>	0.5 M NaHCO <sub>3</sub>	CO	90	0.45	>10	[236]
CoPc/CNT	Co–N <sub>4</sub>	0.1 M KHCO <sub>3</sub>	CH <sub>3</sub> OH	44	0.97	10.6	[237]
CoPc-MWCNT	Co–N <sub>4</sub>	0.5 M KHCO <sub>3</sub>	CH <sub>3</sub> OH	0.3	0.91	11.25	[238]
Ni-CTF	Ni–N <sub>3</sub>	0.1 M KHCO <sub>3</sub>	CO	>90	0.7	~2	[239]
Ni–N <sub>4</sub> –C	Ni–N <sub>4</sub>	0.5 M KHCO <sub>3</sub>	CO	99	0.71	28.6	[122]
Ni–NG	Ni–N <sub>x</sub>	0.5 M KHCO <sub>3</sub>	CO	>95	0.55	>50	[240]
Ni–NCB	Ni–N <sub>x</sub>	0.5 M KHCO <sub>3</sub>	CO	99	0.58	100	[241]
Cu–N <sub>2</sub> /GN	Cu–N <sub>2</sub>	0.1 M KHCO <sub>3</sub>	CO	81	0.4	<5	[242]
CuSAs/TCNFs	Cu–N <sub>4</sub>	0.1 M KHCO <sub>3</sub>	CO	56	0.8	93	[243]
Zn–N–G	Zn–N <sub>x</sub>	0.5 M KHCO <sub>3</sub>	CO	90.8	0.4	~5	[160]
FeMn–N–C	FeMn–N <sub>x</sub>	0.1 M KHCO <sub>3</sub>	CO	~85	0.4	~2	[230]
f-FeCoNC	FeN <sub>3</sub> –CoN <sub>3</sub>	0.1 M KHCO <sub>3</sub>	CO	~80	0.6	~4.5	[199]

The first challenge is how to anchor high-density single metal atoms on the support. An effective approach is introducing volatile metal ions (e.g. Zn) into the precursors. Since the targeted metal species were surrounded by a good deal of Zn ions, after high temperature annealing, the formed metal Zn would evaporate and isolated metal sites are remained in the catalyst with high concentration. For instance, pyrolysis of targeted-metal-containing Zn-MOFs looks promising to obtain SACs with high-density single atoms, but some problems exist, e.g. high synthesis cost, energy-extensive consumption, environmental pollution, etc. The second challenge is how to precisely regulate the coordination environment of isolated metal atoms in the support matrix. Since various vacancies and surface reconstructions for supports would be generated during the synthesis process, multitudinous sites with different configurations might be formed, which causes difficulties to analyze and comprehend the actual active site. To obtain SACs with uniform coordination environment, it is crucial to control the annealing conditions (e.g. temperature, heating rate, etc.). For instance, Co–N<sub>4</sub> configuration is stable at 800 °C, while Co–N<sub>2</sub> configuration would be formed at 900 °C. A Zn–N–C catalyst with a high Zn loading of 9.33 wt% and Zn–N<sub>4</sub> configuration can be obtained by annealing a Zn-containing precursor at 800 °C with a heating rate of 1° min<sup>-1</sup>.

Different active sites were reported to exhibit the best electrochemical performance, for instance, FeN<sub>2</sub>, FeN<sub>4</sub>, and FeN<sub>5</sub> structures have been proposed to be responsible for efficient ORR. There are three main reasons for this phenomenon. (i) The circumstances around the metal-ligand moieties have influence on the electrocatalytic performance, which leads to different catalytic performances of the same active site on different supports. (ii) The fine structures of active sites are mainly disclosed by EXAFS. It is well-known that an average value of coordination number can be obtained by the EXAFS. If an atomically dispersed catalyst contains diverse sites, sometimes low-density configurations are main contributing active sites, which causes wrong understanding by regarding the major structure as the active centers. Therefore, it is pressing to develop more powerful atomic-resolution imaging technique to intuitively “observe” isolated metal centers. (iii) Theoretical simulations and molecule models should conform to the tested systems as far as possible to acquire a rational explanation on experimental data. The pH effects and electrode potential effects should be considered in the calculation model. A well-defined active site structure is conducive to constructing the molecule model and predicting possible reaction mechanisms.

### Declaration of competing interest

The authors declare that they have no known competing financial interests or personal relationships that could have appeared to influence the work reported in this paper.

### Acknowledgments

This work was supported by the National Natural Science Foundation of China (22075099), Natural Science Foundation of Jilin Province (20180101291JC).

### References

- T. Sun, L. Xu, D. Wang, Y. Li, Metal organic frameworks derived single atom catalysts for electrocatalytic energy conversion, *Nano Res* 12 (2019) 2067–2080.
- B. Lu, Q. Liu, S. Chen, Electrocatalysis of single-atom sites: impacts of atomic coordination, *ACS Catal.* 10 (2020) 7584–7618.
- Y. Chen, S. Ji, Y. Wang, J. Dong, W. Chen, Z. Li, R. Shen, L. Zheng, Z. Zhuang, D. Wang, Y. Li, Isolated single iron atoms anchored on N-doped porous carbon as an efficient electrocatalyst for the oxygen reduction reaction, *Angew. Chem. Int. Ed.* 56 (2017) 6937–6941.
- C. Lei, H. Chen, J. Cao, J. Yang, M. Qiu, Y. Xia, C. Yuan, B. Yang, Z. Li, X. Zhang, L. Lei, J. Abbott, Y. Zhong, X. Xia, G. Wu, Q. He, Y. Hou, Fe-N<sub>4</sub> sites embedded into carbon nanofiber integrated with electrochemically exfoliated graphene for oxygen evolution in acidic medium, *Adv. Energy Mater.* 8 (2018) 1801912.
- Y. Cheng, S. Zhao, H. Li, S. He, J.-P. Veder, B. Johannessen, J. Xiao, S. Lu, J. Pan, M.F. Chisholm, S.-Z. Yang, C. Liu, J.G. Chen, S.P. Jiang, Unsaturated edge-anchored Ni single atoms on porous microwave exfoliated graphene oxide for electrochemical CO<sub>2</sub>, *Appl. Catal., B* 243 (2019) 294–303.
- J. Guan, Z. Duan, F. Zhang, S.D. Kelly, R. Si, M. Dupuis, Q. Huang, J.Q. Chen, C. Tang, C. Li, Water oxidation on a mononuclear manganese heterogeneous catalyst, *Nat. Catal.* 1 (2018) 870–877.
- H. Xu, D. Cheng, D. Cao, X.C. Zeng, A universal principle for a rational design of single-atom electrocatalysts, *Nat. Catal.* 1 (2018) 339–348.
- Y. Hou, M. Qiu, M.G. Kim, P. Liu, G. Nam, T. Zhang, X. Zhuang, B. Yang, J. Cho, M. Chen, C. Yuan, L. Lei, X. Feng, Atomically dispersed nickel–nitrogen–sulfur species anchored on porous carbon nanosheets for efficient water oxidation, *Nat. Commun.* 10 (2019) 1392.
- L. Zhang, J.M.T.A. Fischer, Y. Jia, X. Yan, W. Xu, X. Wang, J. Chen, D. Yang, H. Liu, L. Zhuang, M. Hankel, D.J. Searles, K. Huang, S. Feng, C.L. Brown, X. Yao, Coordination of atomic Co–Pt coupling species at carbon defects as active sites for oxygen reduction reaction, *J. Am. Chem. Soc.* 140 (2018) 10757–10763.
- L. Bai, C.-S. Hsu, D. Alexander, H.M. Chen, X. Hu, A cobalt–iron double-atom catalyst for the oxygen evolution reaction, *J. Am. Chem. Soc.* 141 (2019) 14190–14199.
- B.M. Hunter, H.B. Gray, A.M. Müller, Earth-abundant heterogeneous water oxidation catalysts, *Chem. Rev.* 116 (2016) 14120–14136.
- S.K. Kaiser, Z. Chen, D. Faust Akl, S. Mitchell, J. Pérez-Ramírez, Single-atom catalysts across the periodic table, *Chem. Rev.* 120 (2020) 11703–11809.
- B. Qiao, A. Wang, X. Yang, L.F. Allard, Z. Jiang, Y. Cui, J. Liu, J. Li, T. Zhang, Single-atom catalysis of CO oxidation using Pt1/FeOx, *Nat. Chem.* 3 (2011) 634–641.

- [14] H. Zhang, L. Yu, T. Chen, W. Zhou, X.W. Lou, Surface modulation of hierarchical MoS<sub>2</sub> nanosheets by Ni single atoms for enhanced electrocatalytic hydrogen evolution, *Adv. Funct. Mater.* 28 (2018) 1807086.
- [15] P. Liu, Y. Zhao, R. Qin, S. Mo, G. Chen, L. Gu, D.M. Chevrier, P. Zhang, Q. Guo, D. Zang, B. Wu, G. Fu, N. Zheng, Photochemical route for synthesizing atomically dispersed palladium catalysts, *Science* 352 (2016) 797–800.
- [16] L. Zhang, L. Han, H. Liu, X. Liu, J. Luo, Potential-cycling synthesis of single platinum atoms for efficient hydrogen evolution in neutral media, *Angew. Chem. Int. Ed.* 56 (2017) 13694–13698.
- [17] D. Deng, X. Chen, L. Yu, X. Wu, Q. Liu, Y. Liu, H. Yang, H. Tian, Y. Hu, P. Du, R. Si, J. Wang, X. Cui, H. Li, J. Xiao, T. Xu, J. Deng, F. Yang, P.N. Duchesne, P. Zhang, J. Zhou, L. Sun, J. Li, X. Pan, X. Bao, A single iron site confined in a graphene matrix for the catalytic oxidation of benzene at room temperature, *Sci. Adv.* 1 (2015), e1500462.
- [18] B. Pattengale, Y. Huang, X. Yan, S. Yang, S. Younan, W. Hu, Z. Li, S. Lee, X. Pan, J. Gu, J. Huang, Dynamic evolution and reversibility of single-atom Ni(II) active site in 1T-MoS<sub>2</sub> electrocatalysts for hydrogen evolution, *Nat. Commun.* 11 (2020) 4114.
- [19] H. Duan, C. Wang, G. Li, H. Tan, W. Hu, L. Cai, W. Liu, N. Li, Q. Ji, Y. Wang, Y. Lu, W. Yan, F. Hu, W. Zhang, Z. Sun, Z. Qi, L. Song, S. Wei, Single-atom-layer catalysis in a MoS<sub>2</sub> monolayer activated by long-range ferromagnetism for the hydrogen evolution reaction: beyond single-atom catalysis, *Angew. Chem. Int. Ed.* 60 (2021) 7251–7258.
- [20] N. Cheng, X. Sun, Single atom catalyst by atomic layer deposition technique, *Chin. J. Catal.* 38 (2017) 1508–1514.
- [21] M. Liu, L. Wang, K. Zhao, S. Shi, Q. Shao, L. Zhang, X. Sun, Y. Zhao, J. Zhang, Atomically dispersed metal catalysts for the oxygen reduction reaction: synthesis, characterization, reaction mechanisms and electrochemical energy applications, *Energy Environ. Sci.* 12 (2019) 2890–2923.
- [22] X. Wen, Q. Zhang, J. Guan, Applications of metal–organic framework-derived materials in fuel cells and metal-air batteries, *Coord. Chem. Rev.* 409 (2020) 213214.
- [23] D. Su, Advanced electron microscopy characterization of nanomaterials for catalysis, *Green Energy Environ.* 2 (2017) 70–83.
- [24] D. Liu, S. Ding, C. Wu, W. Gan, C. Wang, D. Cao, Z.u. Rehman, Y. Sang, S. Chen, X. Zheng, Y. Wang, B. Ge, L. Song, Synergistic effect of an atomically dual-metal doped catalyst for highly efficient oxygen evolution, *J. Mater. Chem. A* 6 (2018) 6840–6846.
- [25] S. Hwang, X. Chen, G. Zhou, D. Su, In situ transmission electron microscopy on energy-related catalysis, *Adv. Energy Mater.* (2019) 1902105, n/a.
- [26] X. Li, X. Yang, J. Zhang, Y. Huang, B. Liu, In situ/operando techniques for characterization of single-atom catalysts, *ACS Catal.* 9 (2019) 2521–2531.
- [27] J.F. Creemer, S. Helveg, G.H. Hoveling, S. Ullmann, A.M. Molenbroek, P.M. Sarro, H.W. Zandbergen, Atomic-scale electron microscopy at ambient pressure, *Ultramicroscopy* 108 (2008) 993–998.
- [28] J. Wang, Z. Huang, W. Liu, C. Chang, H. Tang, Z. Li, W. Chen, C. Jia, T. Yao, S. Wei, Y. Wu, Y. Li, Design of N-coordinated dual-metal sites: a stable and active Pt-free catalyst for acidic oxygen reduction reaction, *J. Am. Chem. Soc.* 139 (2017) 17281–17284.
- [29] D. Strmcnik, K. Kodama, D. van der Vliet, J. Greeley, V.R. Stamenkovic, N. M. Marković, The role of non-covalent interactions in electrocatalytic fuel-cell reactions on platinum, *Nat. Chem.* 1 (2009) 466–472.
- [30] J. Huang, Mixed quantum-classical treatment of electron transfer at electrocatalytic interfaces: theoretical framework and conceptual analysis, *J. Chem. Phys.* 153 (2020) 164707.
- [31] J. Huang, S. Chen, Interplay between covalent and noncovalent interactions in electrocatalysis, *J. Phys. Chem. C* 122 (2018) 26910–26921.
- [32] H. Ooka, R. Nakamura, Shift of the optimum binding energy at higher rates of catalysis, *J. Phys. Chem. Lett.* 10 (2019) 6706–6713.
- [33] L. Zhu, H. Lin, Y. Li, F. Liao, Y. Lifshitz, M. Sheng, S.-T. Lee, M. Shao, A rhodium/silicon co-electrocatalyst design concept to surpass platinum hydrogen evolution activity at high overpotentials, *Nat. Commun.* 7 (2016) 12272.
- [34] H. Liao, C. Wei, J. Wang, A. Fisher, T. Sritharan, Z. Feng, Z.J. Xu, A multisite strategy for enhancing the hydrogen evolution reaction on a nano-Pd surface in alkaline media, *Adv. Energy Mater.* 7 (2017) 1701129.
- [35] Y. Shao, Z. Jiang, Q. Zhang, J. Guan, Progress in nonmetal-doped graphene electrocatalysts for the oxygen reduction reaction, *Chemsuschem* 12 (2019) 2133–2146.
- [36] A. Nilsson, L. Pettersson, B. Hammer, T. Bligaard, C. Christensen, J.J.C.I. Nørskov, The Electronic Structure Effect in Heterogeneous Catalysis, 100, 2005, pp. 111–114.
- [37] D. Huang, Y. Luo, S. Li, L. Liao, Y. Li, H. Chen, J. Ye, Recent advances in tuning the electronic structures of atomically dispersed M-N-C materials for efficient gas-involving electrocatalysis, *Mater. Horiz.* 7 (2020) 970–986.
- [38] H. Fei, J. Dong, M.J. Arellano-Jiménez, G. Ye, N. Dong Kim, E.L.G. Samuel, Z. Peng, Z. Zhu, F. Qin, J. Bao, M.J. Yacaman, P.M. Ajayan, D. Chen, J.M. Tour, Atomic cobalt on nitrogen-doped graphene for hydrogen generation, *Nat. Commun.* 6 (2015) 8668.
- [39] L. Cao, Q. Luo, W. Liu, Y. Lin, X. Liu, Y. Cao, W. Zhang, Y. Wu, J. Yang, T. Yao, S. Wei, Identification of single-atom active sites in carbon-based cobalt catalysts during electrocatalytic hydrogen evolution, *Nat. Catal.* 2 (2019) 134–141.
- [40] T. Sun, S. Zhao, W. Chen, D. Zhai, J. Dong, Y. Wang, S. Zhang, A. Han, L. Gu, R. Yu, X. Wen, H. Ren, L. Xu, C. Chen, Q. Peng, D. Wang, Y. Li, Single-atomic cobalt sites embedded in hierarchically ordered porous nitrogen-doped carbon as a superior bifunctional electrocatalyst, *Proc. Natl. Acad. Sci. Unit. States Am.* 115 (2018) 12692.
- [41] X. Wen, L. Bai, M. Li, J. Guan, Atomically dispersed cobalt- and nitrogen-codoped graphene toward bifunctional catalysis of oxygen reduction and hydrogen evolution reactions, *ACS Sustain. Chem. Eng.* 7 (2019) 9249–9256.
- [42] X. Song, H. Zhang, Y. Yang, B. Zhang, M. Zuo, X. Cao, J. Sun, C. Lin, X. Li, Z. Jiang, Bifunctional nitrogen and cobalt codoped hollow carbon for electrochemical syngas production, *Adv. Sci.* 5 (2018) 1800177.
- [43] W. Zhao, G. Wan, C. Peng, H. Sheng, J. Wen, H. Chen, Key single-atom electrocatalysis in metal–organic framework (MOF)-Derived bifunctional catalysts, *ChemSusChem* 11 (2018) 3473–3479.
- [44] J.-D. Yi, R. Xu, G.-L. Chai, T. Zhang, K. Zang, B. Nan, H. Lin, Y.-L. Liang, J. Lv, J. Luo, R. Si, Y.-B. Huang, R. Cao, Cobalt single-atoms anchored on porphyrinic triazine-based frameworks as bifunctional electrocatalysts for oxygen reduction and hydrogen evolution reactions, *J. Mater. Chem. A* 7 (2019) 1252–1259.
- [45] T. Sharifi, E. Gracia-Espino, A. Chen, G. Hu, T. Wågberg, Oxygen reduction reactions on single- or few-atom discrete active sites for heterogeneous catalysis, *Adv. Energy Mater.* 0 (2019) 1902084.
- [46] D. Lyu, Y.B. Mollamahale, S. Huang, P. Zhu, X. Zhang, Y. Du, S. Wang, M. Qing, Z. Q. Tian, P.K. Shen, Ultra-high surface area graphitic Fe-N-C nanospheres with single-atom iron sites as highly efficient non-precious metal bifunctional catalysts towards oxygen redox reactions, *J. Catal.* 368 (2018) 279–290.
- [47] Y. Lin, P. Liu, E. Velasco, G. Yao, Z. Tian, L. Zhang, L. Chen, Fabricating single-atom catalysts from chelating metal in open frameworks, *Adv. Mater.* 31 (2019) 1808193.
- [48] Q. Gong, Y. Wang, Q. Hu, J. Zhou, R. Feng, P.N. Duchesne, P. Zhang, F. Chen, N. Han, Y. Li, C. Jin, Y. Li, S.T. Lee, Ultrasmall and phase-pure W2C nanoparticles for efficient electrocatalytic and photoelectrochemical hydrogen evolution, *Nat. Commun.* 7 (2016) 13216.
- [49] Y.-T. Xu, X. Xiao, Z.-M. Ye, S. Zhao, R. Shen, C.-T. He, J.-P. Zhang, Y. Li, X.-M. Chen, Cage-Confinement pyrolysis route to ultrasmall tungsten carbide nanoparticles for efficient electrocatalytic hydrogen evolution, *J. Am. Chem. Soc.* 139 (2017) 5285–5288.
- [50] Z. Chen, W. Gong, Z. Liu, S. Cong, Z. Zheng, Z. Wang, W. Zhang, J. Ma, H. Yu, G. Li, W. Lu, W. Ren, Z. Zhao, Coordination-controlled single-atom tungsten as a non-3d-metal oxygen reduction reaction electrocatalyst with ultrahigh mass activity, *Nano Energy* 60 (2019) 394–403.
- [51] Y. Wang, H. Su, Y. He, L. Li, S. Zhu, H. Shen, P. Xie, X. Fu, G. Zhou, C. Feng, D. Zhao, F. Xiao, X. Zhu, Y. Zeng, M. Shao, S. Chen, G. Wu, J. Zeng, C. Wang, Advanced electrocatalysts with single-metal-atom active sites, *Chem. Rev.* 120 (2020) 12217–12314.
- [52] Y. Wang, J. Mao, X. Meng, L. Yu, D. Deng, X. Bao, Catalysis with two-dimensional materials confining single atoms: concept, design, and applications, *Chem. Rev.* 119 (2019) 1806–1854.
- [53] M.D. Hossain, Z. Liu, M. Zhuang, X. Yan, G.-L. Xu, C.A. Gadre, A. Tyagi, I. H. Abidi, C.-J. Sun, H. Wong, A. Guda, Y. Hao, X. Pan, K. Amine, Z. Luo, Rational design of graphene-supported single atom catalysts for hydrogen evolution reaction, *Adv. Energy Mater.* 9 (2019) 1803689.
- [54] Y. Zhou, G. Gao, Y. Li, W. Chu, L.-W. Wang, Transition-metal single atoms in nitrogen-doped graphenes as efficient active centers for water splitting: a theoretical study, *Phys. Chem. Chem. Phys.* 21 (2019) 3024–3032.
- [55] R. Jasinski, A new fuel cell cathode catalyst, *Nature* 201 (1964) 1212–1213.
- [56] G. Wu, Z. Chen, K. Artyushkova, F.H. Garzon, P. Zelenay, Polyaniline-derived non-precious catalyst for the polymer electrolyte fuel cell cathode, *ECS Trans* 16 (2008) 159–170.
- [57] F. Jaouen, J. Herranz, M. Lefevre, J.-P. Dodelet, U.I. Kramm, I. Herrmann, P. Bogdanoff, J. Maruyama, T. Nagaoka, A. Garsuch, Cross-laboratory experimental study of non-noble-metal electrocatalysts for the oxygen reduction reaction, *ACS Appl. Mater. Interfaces* 1 (2009) 1623–1639.
- [58] S. Ma, G.A. Goenaga, A.V. Call, D.-J. Liu, Cobalt imidazolate framework as precursor for oxygen reduction reaction electrocatalysts, *Chem. Eur. J.* 17 (2011) 2063–2067.
- [59] H. Zhang, W. Zhou, T. Chen, B.Y. Guan, Z. Li, X.W. Lou, A modular strategy for decorating isolated cobalt atoms into multichannel carbon matrix for electrocatalytic oxygen reduction, *Energy Environ. Sci.* 11 (2018) 1980–1984.
- [60] P. Yin, T. Yao, Y. Wu, L. Zheng, Y. Lin, W. Liu, H. Ju, J. Zhu, X. Hong, Z. Deng, G. Zhou, S. Wei, Y. Li, Single cobalt atoms with precise N-coordination as superior oxygen reduction reaction catalysts, *Angew. Chem. Int. Ed.* 55 (2016) 10800–10805.
- [61] W. Zang, A. Sumbja, Y. Ma, H. Zhang, Y. Wu, S. Wu, H. Wu, Z. Liu, C. Guan, J. Wang, S.J. Pennycook, Single Co atoms anchored in porous N-doped carbon for efficient zinc-air battery cathodes, *ACS Catal.* 8 (2018) 8961–8969.
- [62] X. Han, X. Ling, Y. Wang, T. Ma, C. Zhong, W. Hu, Y. Deng, Generation of nanoparticle, atomic-cluster, and single-atom cobalt catalysts from zeolitic imidazolate frameworks by spatial isolation and their use in zinc–air batteries, *Angew. Chem. Int. Ed.* 131 (2019) 5413–5418.
- [63] H. Zhou, T. Yang, Z. Kou, L. Shen, Y. Zhao, Z. Wang, X. Wang, Z. Yang, J. Du, J. Xu, M. Chen, L. Tian, W. Guo, Q. Wang, H. Lv, W. Chen, X. Hong, J. Luo, D. He, Y. Wu, Negative pressure pyrolysis induced highly accessible single sites dispersed on 3D graphene frameworks for enhanced oxygen reduction, *Angew. Chem. Int. Ed.* 59 (2020) 20465–20469.
- [64] G. Wan, P. Yu, H. Chen, J. Wen, C.-j. Sun, H. Zhou, N. Zhang, Q. Li, W. Zhao, B. Xie, T. Li, J. Shi, Engineering single-atom cobalt catalysts toward improved electrocatalysis, *Small* 14 (2018) 1704319.
- [65] X.X. Wang, D.A. Cullen, Y.-T. Pan, S. Hwang, M. Wang, Z. Feng, J. Wang, M. H. Engelhard, H. Zhang, Y. He, Y. Shao, D. Su, K.L. More, J.S. Spendelow, G. Wu, Nitrogen-coordinated single cobalt atom catalysts for oxygen reduction in proton exchange membrane fuel cells, *Adv. Mater.* 30 (2018) 1706758.

- [66] Y. He, S. Hwang, D.A. Cullen, M.A. Uddin, L. Langhorst, B. Li, S. Karakalos, A. J. Kropf, E.C. Wegener, J. Sokolowski, M. Chen, D. Myers, D. Su, K.L. More, G. Wang, S. Litster, G. Wu, Highly active atomically dispersed CoN<sub>4</sub> fuel cell cathode catalysts derived from surfactant-assisted MOFs: carbon-shell confinement strategy, *Energy Environ. Sci.* 12 (2019) 250–260.
- [67] F. Wu, C. Pan, C.-T. He, Y. Han, W. Ma, H. Wei, W. Ji, W. Chen, J. Mao, P. Yu, D. Wang, L. Mao, Y. Li, Single-atom Co-N<sub>4</sub> electrocatalyst enabling four-electron oxygen reduction with enhanced hydrogen peroxide tolerance for selective sensing, *J. Am. Chem. Soc.* 142 (2020) 16861–16867.
- [68] X. Xie, C. He, B. Li, Y. He, D.A. Cullen, E.C. Wegener, A.J. Kropf, U. Martinez, Y. Cheng, M.H. Engelhard, M.E. Bowden, M. Song, T. Lemmon, X.S. Li, Z. Nie, J. Liu, D.J. Myers, P. Zelenay, G. Wang, G. Wu, V. Ramani, Y. Shao, Performance enhancement and degradation mechanism identification of a single-atom Co-N-C catalyst for proton exchange membrane fuel cells, *Nat. Catal.* 3 (2020) 1044–1054.
- [69] J. Gao, H.b. Yang, X. Huang, S.-F. Hung, W. Cai, C. Jia, S. Miao, H.M. Chen, X. Yang, Y. Huang, T. Zhang, B. Liu, Enabling direct H<sub>2</sub>O<sub>2</sub> production in acidic media through rational design of transition metal single atom catalyst, *Chem* 6 (3) (2020) 674–658.
- [70] L. Yang, L. Shi, D. Wang, Y. Lv, D. Cao, Single-atom cobalt electrocatalysts for foldable solid-state Zn-air battery, *Nano Energy* 50 (2018) 691–698.
- [71] X. Sun, S. Sun, S. Gu, Z. Liang, J. Zhang, Y. Yang, Z. Deng, P. Wei, J. Peng, Y. Xu, C. Fang, Q. Li, J. Han, Z. Jiang, Y. Huang, High-performance single atom bifunctional oxygen catalysts derived from ZIF-67 superstructures, *Nano Energy* 61 (2019) 245–250.
- [72] Q. Zhang, Z. Duan, M. Li, J. Guan, Atomic cobalt catalysts for the oxygen evolution reaction, *Chem. Commun.* 56 (2019) 794–797.
- [73] J. Wu, H. Zhou, Q. Li, M. Chen, J. Wan, N. Zhang, L. Xiong, S. Li, B.Y. Xia, G. Feng, M. Liu, L. Huang, Densely populated isolated single Co-N site for efficient oxygen electrocatalysis, *Adv. Energy Mater.* 9 (2019) 1900149.
- [74] H.T. Chung, D.A. Cullen, D. Higgins, B.T. Sneed, E.F. Holby, K.L. More, P. Zelenay, Direct atomic-level insight into the active sites of a high-performance PGM-free ORR catalyst, *Science* 357 (2017) 479–484.
- [75] W. Wei, X. Shi, P. Gao, S. Wang, W. Hu, X. Zhao, Y. Ni, X. Xu, Y. Xu, W. Yan, H. Ji, M. Cao, Well-elaborated, mechanochemically synthesized Fe-TPP<sub>c</sub>ZIF precursors (Fe-TPP = tetraphenylporphine iron) to atomically dispersed iron–nitrogen species for oxygen reduction reaction and Zn-air batteries, *Nano Energy* 52 (2018) 29–37.
- [76] J.-C. Li, F. Xiao, H. Zhong, T. Li, M. Xu, L. Ma, M. Cheng, D. Liu, S. Feng, Q. Shi, H.-M. Cheng, C. Liu, D. Du, S.P. Beckman, X. Pan, Y. Lin, M. Shao, Secondary-atom-Assisted synthesis of single iron atoms anchored on N-doped carbon nanowires for oxygen reduction reaction, *ACS Catal.* 9 (2019) 5929–5934.
- [77] Z. Yang, Y. Wang, M. Zhu, Z. Li, W. Chen, W. Wei, T. Yuan, Y. Qu, Q. Xu, C. Zhao, X. Wang, P. Li, Y. Li, Y. Wu, Y. Li, Boosting oxygen reduction catalysis with Fe-N<sub>4</sub> sites decorated porous carbons toward fuel cells, *ACS Catal.* 9 (2019) 2158–2163.
- [78] Y. Deng, B. Chi, X. Tian, Z. Cui, E. Liu, Q. Jia, W. Fan, G. Wang, D. Dang, M. Li, K. Zang, J. Luo, Y. Hu, S. Liao, X. Sun, S. Mukerjee, g-C<sub>3</sub>N<sub>4</sub> promoted MOF derived hollow carbon nanopolyhedra doped with high density/fraction of single Fe atoms as an ultra-high performance non-precious catalyst towards acidic ORR and PEM fuel cells, *J. Mater. Chem. A* 7 (2019) 5020–5030.
- [79] X. Wan, X. Liu, Y. Li, R. Yu, L. Zheng, W. Yan, H. Wang, M. Xu, J. Shui, Fe–N–C electrocatalyst with dense active sites and efficient mass transport for high-performance proton exchange membrane fuel cells, *Nat. Catal.* 2 (2019) 259–268.
- [80] Y. Chen, S. Ji, S. Zhao, W. Chen, J. Dong, W.-C. Cheong, R. Shen, X. Wen, L. Zheng, A.I. Rykov, S. Cai, H. Tang, Z. Zhuang, C. Chen, Q. Peng, D. Wang, Y. Li, Enhanced oxygen reduction with single-atomic-site iron catalysts for a zinc-air battery and hydrogen-air fuel cell, *Nat. Commun.* 9 (2018) 5422.
- [81] L. Yang, D. Cheng, X. Zeng, X. Wan, J. Shui, Z. Xiang, D. Cao, Unveiling the high-activity origin of single-atom iron catalysts for oxygen reduction reaction, *Proc. Natl. Acad. Sci. U.S.A.* 115 (2018) 6626–6631.
- [82] G. Wu, K.L. More, C.M. Johnston, P. Zelenay, High-performance electrocatalysts for oxygen reduction derived from polyaniline, iron, and cobalt, *Science* 332 (2011) 443–447.
- [83] M. Lefevre, E. Proietti, F. Jaouen, J.-P. Dodelet, Iron-based catalysts with improved oxygen reduction activity in polymer electrolyte fuel cells, *Science* 324 (2009) 71–74.
- [84] A. Zitolo, V. Goellner, V. Armel, M.-T. Sougrati, T. Mineva, L. Stievano, E. Fonda, F. Jaouen, Identification of catalytic sites for oxygen reduction in iron- and nitrogen-doped graphene materials, *Nat. Mater.* 14 (2015) 937–942.
- [85] X. Qiu, X. Yan, H. Pang, J. Wang, D. Sun, S. Wei, L. Xu, Y. Tang, Isolated Fe single atomic sites anchored on highly steady hollow graphene nanospheres as an efficient electrocatalyst for the oxygen reduction reaction, *Adv. Sci.* 6 (2019) 1801103.
- [86] H. Yang, X. Chen, W.-T. Chen, Q. Wang, N.C. Cuello, A. Nafady, A.M. Al-Enizi, G. I.N. Waterhouse, G.A. Goenaga, T.A. Zawodzinski, P.E. Kruger, J.E. Clements, J. Zhang, H. Tian, S.G. Telfer, S. Ma, Tunable synthesis of hollow metal–nitrogen–carbon capsules for efficient oxygen reduction catalysis in proton exchange membrane fuel cells, *ACS Nano* 13 (2019) 8087–8098.
- [87] Y. Qu, L. Wang, Z. Li, P. Li, Q. Zhang, Y. Lin, F. Zhou, H. Wang, Z. Yang, Y. Hu, M. Zhu, X. Zhao, X. Han, C. Wang, Q. Xu, L. Gu, J. Luo, L. Zheng, Y. Wu, Ambient synthesis of single-atom catalysts from bulk metal via trapping of atoms by surface dangling bonds, *Adv. Mater.* 31 (2019) 1904496.
- [88] C. Wang, H. Zhan, J. Wang, Z. Zhao, J. Wang, Y. Zhang, M. Cheng, H. Zhao, J. Wang, Atomic Fe embedded in carbon nanoshells-graphene nanomeshes with enhanced oxygen reduction reaction performance, *Chem. Mater.* 29 (2017) 9915–9922.
- [89] Z.K. Yang, C.-Z. Yuan, A.-W. Xu, A rationally designed Fe-tetrapyridophenazine complex: a promising precursor to a single-atom Fe catalyst for an efficient oxygen reduction reaction in high-power Zn–air cells, *Nanoscale* 10 (2018) 16145–16152.
- [90] F. Xiao, G.-L. Xu, C.-J. Sun, M. Xu, W. Wen, Q. Wang, M. Gu, S. Zhu, Y. Li, Z. Wei, X. Pan, J. Wang, K. Amine, M. Shao, Nitrogen-coordinated single iron atom catalysts derived from metal organic frameworks for oxygen reduction reaction, *Nano Energy* 61 (2019) 60–68.
- [91] Z. Zhang, J. Sun, F. Wang, L. Dai, Efficient oxygen reduction reaction (ORR) catalysts based on single iron atoms dispersed on a hierarchically structured porous carbon framework, *Angew. Chem. Int. Ed.* 57 (2018) 9038–9043.
- [92] G. Chen, P. Liu, Z. Liao, F. Sun, Y. He, H. Zhong, T. Zhang, E. Zschech, M. Chen, G. Wu, J. Zhang, X. Feng, Zinc-mediated template synthesis of Fe-N-C electrocatalysts with densely accessible Fe-N-x active sites for efficient oxygen reduction, *Adv. Mater.* 32 (2020) 1907399.
- [93] R. Jiang, L. Li, T. Sheng, G. Hu, Y. Chen, L. Wang, Edge-site engineering of atomically dispersed Fe-N<sub>4</sub> by selective C–N bond cleavage for enhanced oxygen reduction reaction activities, *J. Am. Chem. Soc.* 140 (2018) 11594–11598.
- [94] Y. Cheng, S. He, S. Lu, J.-P. Veder, B. Johannessen, L. Thomsen, M. Saunders, T. Becker, R. De Marco, Q. Li, S.-z. Yang, S.P. Jiang, Iron single atoms on graphene as nonprecious metal catalysts for high-temperature polymer electrolyte membrane fuel cells, *Adv. Sci.* 6 (2019) 1802066.
- [95] M.-X. Chen, M. Zhu, M. Zuo, S.-Q. Chu, J. Zhang, Y. Wu, H.-W. Liang, X. Feng, Identification of catalytic sites for oxygen reduction in metal/nitrogen-doped carbons with encapsulated metal nanoparticles, *Angew. Chem. Int. Ed.* 59 (2020) 1627–1633.
- [96] M. Primbs, Y. Sun, A. Roy, D. Malko, A. Mahmood, M.-T. Sougrati, P.-Y. Blanchard, G. Granozzi, T. Kosmala, G. Daniel, P. Atanassov, J. Sharman, C. Durante, A. Kucernak, D. Jones, F. Jaouen, P. Strasser, Establishing reactivity descriptors for platinum group metal (PGM)-free Fe-N-C catalysts for PEM fuel cells, *Energy Environ. Sci.* 13 (2020) 2480–2500.
- [97] L. Gao, M. Xiao, Z. Jin, C. Liu, J. Ge, W. Xing, Hydrogen etching induced hierarchical meso/micro-pore structure with increased active density to boost ORR performance of Fe-N-C catalyst, *J. Energy Chem.* 35 (2019) 17–23.
- [98] J.-C. Li, M. Cheng, T. Li, L. Ma, X. Ruan, D. Liu, H.-M. Cheng, C. Liu, D. Du, Z. Wei, Y. Lin, M. Shao, Carbon nanotube-linked hollow carbon nanospheres doped with iron and nitrogen as single-atom catalysts for the oxygen reduction reaction in acidic solutions, *J. Mater. Chem. A* 7 (2019) 14478–14482.
- [99] T. Marshall-Roth, N.J. Libretto, A.T. Wrobel, K.J. Anderton, M.L. Pegis, N. D. Ricke, T. Van Voorhis, J.T. Miller, Y. Surendranath, A pyridinic Fe-N<sub>4</sub> macrocycle models the active sites in Fe/N-doped carbon electrocatalysts, *Nat. Commun.* 11 (2020) 5283.
- [100] M. Qiao, Y. Wang, Q. Wang, G. Hu, X. Mamat, S. Zhang, S. Wang, Hierarchically ordered porous carbon with atomically dispersed FeN<sub>4</sub> for ultraefficient oxygen reduction reaction in proton-exchange membrane fuel cells, *Angew. Chem. Int. Ed.* 59 (2020) 2688–2694.
- [101] H. Zhang, S. Hwang, M. Wang, Z. Feng, S. Karakalos, L. Luo, Z. Qiao, X. Xie, C. Wang, D. Su, Y. Shao, G. Wu, Single atomic iron catalysts for oxygen reduction in acidic media: particle size control and thermal activation, *J. Am. Chem. Soc.* 139 (2017) 14143–14149.
- [102] Y. Qian, Q. Liu, E. Sarnello, C. Tang, M. Chng, J. Shui, T. Li, S.J. Pennycook, M. Han, D. Zhao, MOF-derived carbon networks with atomically dispersed Fe-N<sub>x</sub> sites for oxygen reduction reaction catalysis in acidic media, *Acs Mater. Lett.* 1 (2019) 37–43.
- [103] F. Dionigi, Z. Zeng, I. Sinev, T. Merzdorf, S. Deshpande, M.B. Lopez, S. Kunze, I. Zegkinoglou, H. Sarodnik, D. Fan, A. Bergmann, J. Drnec, J.F. de Araujo, M. Gleich, D. Teschner, J. Zhu, W.-X. Li, J. Greeley, B. Roldan Cuena, P. Strasser, In-situ structure and catalytic mechanism of NiFe and CoFe layered double hydroxides during oxygen evolution, *Nat. Commun.* 11 (2020) 2522.
- [104] L. Ma, S. Chen, Z. Pei, Y. Huang, G. Liang, F. Mo, Q. Yang, J. Su, Y. Gao, J. A. Zapien, C. Zhi, Single-site active iron-based bifunctional oxygen catalyst for a compressible and rechargeable zinc-air battery, *ACS Nano* 12 (2018) 1949–1958.
- [105] P. Chen, T. Zhou, L. Xing, K. Xu, Y. Tong, H. Xie, L. Zhang, W. Yan, W. Chu, C. Wu, Y. Xie, Atomically dispersed iron–nitrogen species as electrocatalysts for bifunctional oxygen evolution and reduction reactions, *Angew. Chem. Int. Ed.* 56 (2017) 610–614.
- [106] L. Bai, Z. Duan, X. Wen, J. Guan, Bifunctional atomic iron-based catalyst for oxygen electrode reactions, *J. Catal.* 378 (2019) 353–362.
- [107] X. Su, X.-F. Yang, Y. Huang, B. Liu, T. Zhang, Single-atom catalysis toward efficient CO<sub>2</sub> conversion to CO and formate products, *Acc. Chem. Res.* 52 (2019) 656–664.
- [108] H. Zhang, J. Wang, Z. Zhao, H. Zhao, M. Cheng, A. Li, C. Wang, J. Wang, J. Wang, The synthesis of atomic Fe embedded in bamboo-CNTs grown on graphene as a superior CO<sub>2</sub> electrocatalyst, *Green Chem.* 20 (2018) 3521–3529.
- [109] X. Li, G. Chai, X. Xu, J. Liu, Z. Zhong, A. Cao, Z. Tao, W. You, L. Kang, Electrocatalytic reduction of CO<sub>2</sub> to CO over iron phthalocyanine-modified graphene nanocomposites, *Carbon* 167 (2020) 658–667.
- [110] J. Tuo, Y. Lin, Y. Zhu, H. Jiang, Y. Li, L. Cheng, R. Pang, J. Shen, L. Song, C. Li, Local structure tuning in Fe-N-C catalysts through support effect for boosting CO<sub>2</sub> electroreduction, *Appl. Catal., B* 272 (2020) 118960.
- [111] J. Zhao, J. Deng, J. Han, S. Imhanria, K. Chen, W. Wang, Effective tunable syngas generation via CO<sub>2</sub> reduction reaction by non-precious Fe-N-C electrocatalyst, *Chem. Eng. J.* 389 (2020) 124323.
- [112] Q. Zhang, J. Guan, Single-atom catalysts for electrocatalytic applications, *Adv. Funct. Mater.* 30 (2020) 2000768.

- [113] C. Zhang, S. Yang, J. Wu, M. Liu, S. Yazdi, M. Ren, J. Sha, J. Zhong, K. Nie, A. S. Jalilov, Z. Li, H. Li, B.I. Yakobson, Q. Wu, E. Ringe, H. Xu, P.M. Ajayan, J. M. Tour, Electrochemical CO<sub>2</sub> reduction with atomic iron-dispersed on nitrogen-doped graphene, *Adv. Energy Mater.* 8 (2018) 1703487.
- [114] T.N. Huan, N. Ranjbar, G. Rousse, M. Sougrati, A. Zitolo, V. Mougel, F. Jaouen, M. Fontecave, Electrochemical reduction of CO<sub>2</sub> catalyzed by Fe-N-C materials: a structure-selectivity study, *ACS Catal.* 7 (2017) 1520–1525.
- [115] Y. Chen, L. Zou, H. Liu, C. Chen, Q. Wang, M. Gu, B. Yang, Z. Zou, J. Fang, H. Yang, Fe and N Co-doped porous carbon nanospheres with high density of active sites for efficient CO<sub>2</sub> electroreduction, *J. Phys. Chem. C* 123 (2019) 16651–16659.
- [116] W. Ju, A. Bagger, X. Wang, Y. Tsai, F. Luo, T. Möller, H. Wang, J. Rossmeisl, A. S. Varela, P. Strasser, Unraveling mechanistic reaction pathways of the electrochemical CO<sub>2</sub> reduction on Fe–N–C single-site catalysts, *ACS Energy Lett.* 4 (2019) 1663–1671.
- [117] N. Mohd Adli, W. Shan, S. Hwang, W. Samarakoon, S. Karakalos, Y. Li, D. A. Cullen, D. Su, Z. Feng, G. Wang, G. Wu, Engineering atomically dispersed FeN<sub>4</sub> active sites for CO<sub>2</sub> electroreduction, *Angew. Chem. Int. Ed.* 60 (2021) 1022–1032.
- [118] Y. Qiu, X. Peng, F. Lü, Y. Mi, L. Zhuo, J. Ren, X. Liu, J. Luo, Single-atom catalysts for the electrocatalytic reduction of nitrogen to ammonia under ambient conditions, *Chem. Asian J.* 14 (2019) 2770–2779.
- [119] F. Lü, S. Zhao, R. Guo, J. He, X. Peng, H. Bao, J. Fu, L. Han, G. Qi, J. Luo, X. Tang, X. Liu, Nitrogen-coordinated single Fe sites for efficient electrocatalytic N<sub>2</sub> fixation in neutral media, *Nano Energy* 61 (2019) 420–427.
- [120] M. Wang, S. Liu, T. Qian, J. Liu, J. Zhou, H. Ji, J. Xiong, J. Zhong, C. Yan, Over 56.55% Faradaic efficiency of ambient ammonia synthesis enabled by positively shifting the reaction potential, *Nat. Commun.* 10 (2019) 341.
- [121] M.D. Hossain, Y. Huang, T.H. Yu, W.A. Goddard III, Z. Luo, Reaction mechanism and kinetics for CO<sub>2</sub> reduction on nickel single atom catalysts from quantum mechanics, *Nat. Commun.* 11 (2020) 2256.
- [122] X. Li, W. Bi, M. Chen, Y. Sun, H. Ju, W. Yan, J. Zhu, X. Wu, W. Chu, C. Wu, Y. Xie, Exclusive Ni–N<sub>4</sub> sites realize near-unity CO selectivity for electrochemical CO<sub>2</sub> reduction, *J. Am. Chem. Soc.* 139 (2017) 14889–14892.
- [123] H.B. Yang, S.-F. Hung, S. Liu, K. Yuan, S. Miao, L. Zhang, X. Huang, H.-Y. Wang, W. Cai, R. Chen, J. Gao, X. Yang, W. Chen, Y. Huang, H.M. Chen, C.M. Li, T. Zhang, B. Liu, Atomically dispersed Ni(i) as the active site for electrochemical CO<sub>2</sub> reduction, *Nat. Energy* 3 (2018) 140–147.
- [124] X. Wang, Y. Wang, X. Sang, W. Zheng, S. Zhang, L. Shuai, B. Yang, Z. Li, J. Chen, L. Lei, N.M. Adli, M.K.H. Leung, M. Qiu, G. Wu, Y. Hou, Dynamic activation of adsorbed intermediates via axial traction for the promoted electrochemical CO<sub>2</sub> reduction, *Angew. Chem. Int. Ed.* 60 (2021) 4192–4198.
- [125] W. Xiong, H. Li, H. Wang, J. Yi, H. You, S. Zhang, Y. Hou, M. Cao, T. Zhang, R. Cao, Hollow mesoporous carbon sphere loaded Ni-N(4)Single-atom: support structure study for CO(2)Electrocatalytic reduction catalyst, *Small* 16 (2020) 2003943.
- [126] S. Liu, H.B. Yang, S.-F. Hung, J. Ding, W. Cai, L. Liu, J. Gao, X. Li, X. Ren, Z. Kuang, Y. Huang, T. Zhang, B. Liu, Elucidating the electrocatalytic CO<sub>2</sub> reduction reaction over a model single-atom nickel catalyst, *Angew. Chem. Int. Ed.* 59 (2020) 798–803.
- [127] H. Fei, J. Dong, Y. Feng, C.S. Allen, C. Wan, B. Voloskiy, M. Li, Z. Zhao, Y. Wang, H. Sun, P. An, W. Chen, Z. Guo, C. Lee, D. Chen, I. Shakir, M. Liu, T. Hu, Y. Li, A. I. Kirkland, X. Duan, Y. Huang, General synthesis and definitive structural identification of MN4C4 single-atom catalysts with tunable electrocatalytic activities, *Nat. Catal.* 1 (2018) 63–72.
- [128] Q. Deng, J. Zhao, T. Wu, G. Chen, H.A. Hansen, T. Vegge, 2D transition metal-TCNQ sheets as bifunctional single-atom catalysts for oxygen reduction and evolution reaction (ORR/OER), *J. Catal.* 370 (2019) 378–384.
- [129] G. Gao, S. Bottle, A. Du, Understanding the activity and selectivity of single atom catalysts for hydrogen and oxygen evolution via ab initio study, *Catal. Sci. Technol.* 8 (2018) 996–1001.
- [130] H. Zhang, Y. Liu, T. Chen, J. Zhang, J. Zhang, X.W. Lou, Unveiling the activity origin of electrocatalytic oxygen evolution over isolated Ni atoms supported on a N-doped carbon matrix, *Adv. Mater.* 31 (2019) 1904548.
- [131] J. Li, M. Chen, D.A. Cullen, S. Hwang, M. Wang, B. Li, K. Liu, S. Karakalos, M. Lucero, H. Zhang, C. Lei, H. Xu, G.E. Sterbinsky, Z. Feng, D. Su, K.L. More, G. Wang, Z. Wang, G. Wu, Atomically dispersed manganese catalysts for oxygen reduction in proton-exchange membrane fuel cells, *Nat. Catal.* 1 (2018) 935–945.
- [132] L. Bai, Z. Duan, X. Wen, R. Si, J. Guan, Atomically dispersed manganese-based catalysts for efficient catalysis of oxygen reduction reaction, *Appl. Catal., B* 257 (2019) 117930.
- [133] M. Chen, X. Li, F. Yang, B. Li, T. Stracensky, S. Karakalos, S. Mukerjee, Q. Jia, D. Su, G. Wang, G. Wu, H. Xu, Atomically dispersed MnN<sub>4</sub> catalysts via environmentally Benign aqueous synthesis for oxygen reduction: mechanistic understanding of activity and stability improvements, *ACS Catal.* 10 (2020) 10523–10534.
- [134] G. Zhu, F. Liu, Y. Wang, Z. Wei, W. Wang, Systematic exploration of N,C coordination effects on the ORR performance of Mn–N<sub>x</sub> doped graphene catalysts based on DFT calculations, *Phys. Chem. Chem. Phys.* 21 (2019) 12826–12836.
- [135] X. Han, T. Zhang, W. Chen, B. Dong, G. Meng, L. Zheng, C. Yang, X. Sun, Z. Zhuang, D. Wang, A. Han, J. Liu, Mn-N<sub>4</sub> oxygen reduction electrocatalyst: operando investigation of active sites and high performance in zinc–air battery, *Adv. Energy Mater.* 11 (2020) 2002753.
- [136] H. Xu, D. Wang, P. Yang, A. Liu, R. Li, Y. Li, L. Xiao, J. Zhang, M. An, A theoretical study of atomically dispersed MN4/C (M = Fe or Mn) as a high-activity catalyst for the oxygen reduction reaction, *Phys. Chem. Chem. Phys.* 22 (2020) 28297–28303.
- [137] M. Busch, N.B. Halck, U.I. Kramm, S. Siahrostami, P. Krttil, J. Rossmeisl, Beyond the top of the volcano? - a unified approach to electrocatalytic oxygen reduction and oxygen evolution, *Nano Energy* 29 (2016) 126–135.
- [138] W. Zhang, K. Mao, X.C. Zeng, B-doped MnN<sub>4</sub>-G nanosheets as bifunctional electrocatalysts for both oxygen reduction and oxygen evolution reactions, *ACS Sustain. Chem. Eng.* 7 (2019) 18711–18717.
- [139] Y. Qu, Z. Li, W. Chen, Y. Lin, T. Yuan, Z. Yang, C. Zhao, J. Wang, C. Zhao, X. Wang, F. Zhou, Z. Zhuang, Y. Wu, Y. Li, Direct transformation of bulk copper into copper single sites via emitting and trapping of atoms, *Nat. Catal.* 1 (2018) 781–786.
- [140] L. Cui, L. Cui, Z. Li, J. Zhang, H. Wang, S. Lu, Y. Xiang, A copper single-atom catalyst towards efficient and durable oxygen reduction for fuel cells, *J. Mater. Chem. A* 7 (2019) 16690–16695.
- [141] A. Guan, Z. Chen, Y. Quan, C. Peng, Z. Wang, T.-K. Sham, C. Yang, Y. Ji, L. Qian, X. Xu, G. Zheng, Boosting CO<sub>2</sub> electroreduction to CH<sub>4</sub> via tuning neighboring single-copper sites, *ACS Energy Lett.* 5 (2020) 1044–1053.
- [142] E. Luo, H. Zhang, X. Wang, L. Gao, L. Gong, T. Zhao, Z. Jin, J. Ge, Z. Jiang, C. Liu, W. Xing, Single-atom Cr–N<sub>4</sub> sites designed for durable oxygen reduction catalysis in acid media, *Angew. Chem. Int. Ed.* (2019) 0.
- [143] S. Liu, K. Mase, C. Bouger, S.D. Hicks, M.M. Abu-Omar, S. Fukuzumi, High-valent chromium-oxo complex acting as an efficient catalyst precursor for selective two-electron reduction of dioxygen by a ferrocene derivative, *Inorg. Chem.* 53 (2014) 7780–7788.
- [144] P. Song, M. Luo, X. Liu, W. Xing, W. Xu, Z. Jiang, L. Gu, Zn single atom catalyst for highly efficient oxygen reduction reaction, *Adv. Funct. Mater.* 27 (2017) 1700802.
- [145] J. Li, S. Chen, N. Yang, M. Deng, S. Ibraheem, J. Deng, J. Li, L. Li, Z. Wei, Ultrahigh-loading zinc single-atom catalyst for highly efficient oxygen reduction in both acidic and alkaline media, *Angew. Chem. Int. Ed.* 58 (2019) 7035–7039.
- [146] L. Bai, Z. Duan, X. Wen, R. Si, Q. Zhang, J. Guan, Highly dispersed ruthenium-based multifunctional electrocatalyst, *ACS Catal.* 9 (2019) 9897–9904.
- [147] C. Zhang, J. Sha, H. Fei, M. Liu, S. Yazdi, J. Zhang, Q. Zhong, X. Zou, N. Zhao, H. Yu, Z. Jiang, E. Ringe, B.I. Yakobson, J. Dong, D. Chen, J.M. Tour, Single-atomic ruthenium catalytic sites on nitrogen-doped graphene for oxygen reduction reaction in acidic medium, *ACS Nano* 11 (2017) 6930–6941.
- [148] M. Xiao, L. Gao, Y. Wang, X. Wang, J. Zhu, Z. Jin, C. Liu, H. Chen, G. Li, J. Ge, Q. He, Z. Wu, Z. Chen, W. Xing, Engineering energy level of metal center: Ru single-atom site for efficient and durable oxygen reduction catalysis, *J. Am. Chem. Soc.* 141 (2019) 19800–19806.
- [149] Q. Zhang, Z. Duan, Y. Wang, L. Li, B. Nan, J. Guan, Atomically dispersed iridium catalysts for multifunctional electrocatalysis, *J. Mater. Chem. A* 8 (2020) 19665–19673.
- [150] M. Xiao, J. Zhu, G. Li, N. Li, S. Li, Z.P. Cano, L. Ma, P. Cui, P. Xu, G. Jiang, H. Jin, S. Wang, T. Wu, J. Lu, A. Yu, D. Su, Z. Chen, A single-atom iridium heterogeneous catalyst in oxygen reduction reaction, *Angew. Chem. Int. Ed.* 58 (2019) 9640–9645.
- [151] E. Zhang, T. Wang, K. Yu, J. Liu, W. Chen, A. Li, H. Rong, R. Lin, S. Ji, X. Zheng, Y. Wang, L. Zheng, C. Chen, D. Wang, J. Zhang, Y. Li, Bismuth single atoms resulting from transformation of metal–organic frameworks and their use as electrocatalysts for CO<sub>2</sub> reduction, *J. Am. Chem. Soc.* 141 (2019) 16569–16573.
- [152] S. Back, A.R. Kulkarni, S. Siahrostami, Single metal atoms anchored in two-dimensional materials: bifunctional catalysts for fuel cell applications, *ChemCatChem* 10 (2018) 3034–3039.
- [153] J. Guan, X. Wen, Q. Zhang, Z. Duan, Atomic rhodium catalysts for hydrogen evolution and oxygen reduction reactions, *Carbon* 164 (2020) 121–128.
- [154] T. Li, J. Liu, Y. Song, F. Wang, Photochemical solid-phase synthesis of platinum single atoms on nitrogen-doped carbon with high loading as bifunctional catalysts for hydrogen evolution and oxygen reduction reactions, *ACS Catal.* 8 (2018) 8450–8458.
- [155] X.-F. Li, Q.-K. Li, J. Cheng, L. Liu, Q. Yan, Y. Wu, X.-H. Zhang, Z.-Y. Wang, Q. Qiu, Y. Luo, Conversion of dinitrogen to ammonia by FeN<sub>3</sub>-embedded graphene, *J. Am. Chem. Soc.* 138 (2016) 8706–8709.
- [156] S. Ma, Z. Han, K. Leng, X. Liu, Y. Wang, Y. Qu, J. Bai, Ionic exchange of metal–organic frameworks for constructing unsaturated copper single-atom catalysts for boosting oxygen reduction reaction, *Small* 16 (2020) 2001384.
- [157] P. Ou, X. Zhou, F. Meng, C. Chen, Y. Chen, J. Song, Single molybdenum center supported on N-doped black phosphorus as an efficient electrocatalyst for nitrogen fixation, *Nanoscale* 11 (2019) 13600–13611.
- [158] Z. Geng, Y. Liu, X. Kong, P. Li, K. Li, Z. Liu, J. Du, M. Shu, R. Si, J. Zeng, Achieving a record-high yield rate of 120.9 for N<sub>2</sub> electrochemical reduction over Ru single-atom catalysts, *Adv. Mater.* 30 (2018) 1803498.
- [159] X. Wang, Z. Chen, X. Zhao, T. Yao, W. Chen, R. You, C. Zhao, G. Wu, J. Wang, W. Huang, J. Yang, X. Hong, S. Wei, Y. Wu, Y. Li, Regulation of coordination number over single Co sites: triggering the efficient electroreduction of CO<sub>2</sub>, *Angew. Chem. Int. Ed.* 130 (2018) 1962–1966.
- [160] C. Yan, H. Li, Y. Ye, H. Wu, F. Cai, R. Si, J. Xiao, S. Miao, S. Xie, F. Yang, Y. Li, G. Wang, X. Bao, Coordinatively unsaturated nickel–nitrogen sites towards selective and high-rate CO<sub>2</sub> electroreduction, *Energy Environ. Sci.* 11 (2018) 1204–1210.
- [161] P. Song, Y. Wang, J. Pan, W. Xu, L. Zhuang, Structure-activity relationship in high-performance iron-based electrocatalysts for oxygen reduction reaction, *J. Power Sources* 300 (2015) 279–284.

- [162] F. Jaouen, S. Marcotte, J.P. Dodelet, G. Lindbergh, Oxygen reduction catalysts for polymer electrolyte fuel cells from the pyrolysis of iron acetate adsorbed on various carbon supports, *J. Phys. Chem. B* 107 (2003) 1376–1386.
- [163] H. Shen, E. Gracia-Espino, J. Ma, H. Tang, X. Mamat, T. Wagberg, G. Hu, S. Guo, Atomically FeN<sub>2</sub> moieties dispersed on mesoporous carbon: a new atomic catalyst for efficient oxygen reduction catalysis, *Nano Energy* 35 (2017) 9–16.
- [164] C. Zhu, Q. Shi, B.Z. Xu, S. Fu, G. Wan, C. Yang, S. Yao, J. Song, H. Zhou, D. Du, S. P. Beckman, D. Su, Y. Lin, Hierarchically porous M–N–C (M = Co and Fe) single-atom electrocatalysts with robust MN<sub>x</sub> active moieties enable enhanced ORR performance, *Adv. Energy Mater.* 8 (2018) 1801956.
- [165] H. Wu, H. Li, X. Zhao, Q. Liu, J. Wang, J. Xiao, S. Xie, R. Si, F. Yang, S. Miao, X. Guo, G. Wang, X. Bao, Highly doped and exposed Cu(i)–N active sites within grapheme towards efficient oxygen reduction for zinc-air batteries, *Energy Environ. Sci.* 9 (2016) 3736–3745.
- [166] F. Li, G.-F. Han, H.-J. Noh, S.-J. Kim, Y. Lu, H.Y. Jeong, Z. Fu, J.-B. Baek, Boosting oxygen reduction catalysis with abundant copper single atom active sites, *Energy Environ. Sci.* 11 (2018) 2263–2269.
- [167] D. Wang, C. Ao, X. Liu, S. Fang, Y. Lin, W. Liu, W. Zhang, X. Zheng, L. Zhang, T. Yao, Coordination-engineered Cu–nx single-site catalyst for enhancing oxygen reduction reaction, *ACS Appl. Energy Mater.* 2 (2019) 6497–6504.
- [168] X. Xie, J. Liu, T. Li, Y. Song, F. Wang, Post-formation copper-nitrogen species on carbon black: their chemical structures and active sites for oxygen reduction reaction, *Chem. Eur. J.* 24 (2018) 9968–9975.
- [169] W. Zang, T. Yang, H. Zou, S. Xi, H. Zhang, X. Liu, Z. Kou, Y. Du, Y.P. Feng, L. Shen, L. Duan, J. Wang, S.J. Pennycook, Copper single atoms anchored in porous nitrogen-doped carbon as efficient pH-universal catalysts for the nitrogen reduction reaction, *ACS Catal.* 9 (2019) 10166–10173.
- [170] F. Li, Y. Bu, G.-F. Han, H.-J. Noh, S.-J. Kim, I. Ahmad, Y. Lu, P. Zhang, H.Y. Jeong, Z. Fu, Q. Zhong, J.-B. Baek, Identifying the structure of Zn-N<sub>2</sub> active sites and structural activation, *Nat. Commun.* 10 (2019) 2623.
- [171] X. Wen, Z. Duan, L. Bai, J. Guan, Atomic scandium and nitrogen-codoped graphene for oxygen reduction reaction, *J. Power Sources* 431 (2019) 265–273.
- [172] H. Tao, C. Choi, L.-X. Ding, Z. Jiang, Z. Han, M. Jia, Q. Fan, Y. Gao, H. Wang, A. W. Robertson, S. Hong, Y. Jung, S. Liu, Z. Sun, Nitrogen fixation by Ru single-atom electrocatalytic reduction, *Inside Chem.* 5 (2019) 204–214.
- [173] T. He, S.K. Matta, A. Du, Single tungsten atom supported on N-doped graphyne as a high-performance electrocatalyst for nitrogen fixation under ambient conditions, *Phys. Chem. Chem. Phys.* 21 (2019) 1546–1551.
- [174] J. Zhang, Y. Zhao, C. Chen, Y.-C. Huang, C.-L. Dong, C.-J. Chen, R.-S. Liu, C. Wang, K. Yan, Y. Li, G. Wang, Tuning the coordination environment in single-atom catalysts to achieve highly efficient oxygen reduction reactions, *J. Am. Chem. Soc.* 141 (2019) 20118–20126.
- [175] L. Omann, C.D.F. Koenigs, H.F.T. Klare, M. Oestreich, Cooperative catalysis at metal-sulfur bonds, *Acc. Chem. Res.* 50 (2017) 1258–1269.
- [176] Y. Wang, F. Chu, J. Zeng, Q. Wang, T. Naren, Y. Li, Y. Cheng, Y. Lei, F. Wu, Single atom catalysts for fuel cells and rechargeable batteries: principles, advances, and opportunities, *ACS Nano* 15 (2021) 210–239.
- [177] J. Yang, A.R. Mohmad, Y. Wang, R. Fullon, X. Song, F. Zhao, I. Bozkurt, M. Augustin, E.J.G. Santos, H.S. Shin, W. Zhang, D. Voiry, H.Y. Jeong, M. Chhowalla, Ultrahigh-current-density niobium disulfide catalysts for hydrogen evolution, *Nat. Mater.* 18 (2019), 1309–.
- [178] W. Chen, H. Wang, Y. Li, Y. Liu, J. Sun, S. Lee, J.-S. Lee, Y. Cui, In situ electrochemical oxidation tuning of transition metal disulfides to oxides for enhanced water oxidation, *ACS Cent. Sci.* 1 (2015) 244–251.
- [179] D. Xiong, Q. Zhang, W. Li, J. Li, X. Fu, M.F. Cerqueira, P. Alpuim, L. Liu, Atomic-layer-deposited ultrafine MoS<sub>2</sub> nanocrystals on cobalt foam for efficient and stable electrochemical oxygen evolution, *Nanoscale* 9 (2017) 2711–2717.
- [180] J. Guo, N. Xu, Y. Wang, X. Wang, H. Huang, J. Quo, Bimetallic sulfide with controllable Mg substitution anchored on CNTs as hierarchical bifunctional catalyst toward oxygen catalytic reactions for rechargeable zinc-air batteries, *ACS Appl. Mater. Interfaces* 12 (2020) 37164–37172.
- [181] Y. Liang, Q. Gong, X. Sun, N. Xu, P. Gong, J. Qiao, Rational fabrication of thin-layered NiCo<sub>2</sub>S<sub>4</sub> loaded graphene as bifunctional non-oxide catalyst for rechargeable zinc-air batteries, *Electrochim. Acta* 342 (2020).
- [182] Y. Xiao, L. Tang, High-throughput approach exploitation: two-dimensional double-metal sulfide (M2S2) of efficient electrocatalysts for oxygen reduction reaction in fuel cells, *Energy Fuels* 34 (2020) 5006–5015.
- [183] P.-Y. Liu, K. Shi, W.-Z. Chen, R. Gao, Z.-L. Liu, H. Hao, Y.-Q. Wang, Enhanced electrocatalytic nitrogen reduction reaction performance by interfacial engineering of MOF-based sulfides FeNi<sub>2</sub>S<sub>4</sub>/NiS hetero-interface, *Appl. Catal., B* 287 (2021) 119956.
- [184] Z. Han, Q. Hu, Z. Cheng, G. Li, X. Huang, Z. Wang, H. Yang, X. Ren, Q. Zhang, J. Liu, C. He, High-performance overall CO<sub>2</sub> splitting on hierarchical structured cobalt disulfide with partially removed sulfur edges, *Adv. Funct. Mater.* 30 (2020) 2000154.
- [185] C.H. Choi, M. Kim, H.C. Kwon, S.J. Cho, S. Yun, H.-T. Kim, K.J.J. Mayrhofer, H. Kim, M. Choi, Tuning selectivity of electrochemical reactions by atomically dispersed platinum catalyst, *Nat. Commun.* 7 (2016) 10922.
- [186] J. Xu, R. Li, C.-Q. Xu, R. Zeng, Z. Jiang, B. Mei, J. Li, D. Meng, J. Chen, Underpotential-deposition synthesis and in-line electrochemical analysis of single -atom copper electrocatalysts, *Appl. Catal., B* 289 (2021) 120028.
- [187] H.B. Wu, B.Y. Xia, L. Yu, X.-Y. Yu, X.W. Lou, Porous molybdenum carbide nano-octahedrons synthesized via confined carburization in metal-organic frameworks for efficient hydrogen production, *Nat. Commun.* 6 (2015) 6512.
- [188] H. Cheng, L.X. Ding, G.F. Chen, L. Zhang, J. Xue, H. Wang, Molybdenum carbide nanodots enable efficient electrocatalytic nitrogen fixation under ambient conditions, *Adv. Mater.* 30 (2018) 1803694.
- [189] C. Ling, Y. Ouyang, Q. Li, X. Bai, X. Mao, A. Du, J. Wang, A general two-step strategy-based high-throughput screening of single atom catalysts for nitrogen fixation, *Small Methods* 3 (2019) 1800376.
- [190] Y. Wang, Z. Chen, P. Han, Y. Du, Z. Gu, X. Xu, G. Zheng, Single-atomic Cu with multiple oxygen vacancies on ceria for electrocatalytic CO<sub>2</sub> reduction to CH<sub>4</sub>, *ACS Catal.* 8 (2018) 7113–7119.
- [191] S. Ma, W. Song, B. Liu, H. Zheng, J. Deng, W. Zhong, J. Liu, X.-Q. Gong, Z. Zhao, Elucidation of the high CO<sub>2</sub> reduction selectivity of isolated Rh supported on TiO<sub>2</sub>: a DFT study, *Catal. Sci. Technol.* 6 (2016) 6128–6136.
- [192] S. Zhang, M. Jin, T. Shi, M. Han, Q. Sun, Y. Lin, Z. Ding, L.R. Zheng, G. Wang, Y. Zhang, H. Zhang, H. Zhao, Electrocatalytically active Fe-(O-C-2)(4) single-atom sites for efficient reduction of nitrogen to ammonia, *Angew. Chem. Int. Ed.* 59 (2020) 13423–13429.
- [193] W. Liu, Q. Xu, P. Yan, J. Chen, Y. Du, S. Chu, J. Wang, Fabrication of a single-atom platinum catalyst for the hydrogen evolution reaction: a new protocol by utilization of HxMoO<sub>3</sub>-x with plasmon resonance, *ChemCatChem* 10 (2018) 946–950.
- [194] S. Dou, C.-L. Dong, Z. Hu, Y.-C. Huang, J.-L. Chen, L. Tao, D. Yan, D. Chen, S. Shen, S. Chou, S. Wang, Atomic-Scale CoOx species in metal-organic frameworks for oxygen evolution reaction, *Adv. Funct. Mater.* 27 (2017) 1702546.
- [195] C. Liu, J. Qian, Y. Ye, H. Zhou, C.-J. Sun, C. Sheehan, Z. Zhang, G. Wan, Y.-S. Liu, J. Guo, S. Li, H. Shin, S. Hwang, T.B. Gunnoe, W.A. Goddard III, S. Zhang, Oxygen evolution reaction over catalytic single-site Co in a well-defined brookite TiO<sub>2</sub> nanorod surface, *Nat. Catal.* 4 (2021) 36–45.
- [196] W. Ye, S. Chen, Y. Lin, L. Yang, S. Chen, X. Zheng, Z. Qi, C. Wang, R. Long, M. Chen, J. Zhu, P. Gao, L. Song, J. Jiang, Y. Xiong, Precisely tuning the number of Fe atoms in clusters on N-doped carbon toward acidic oxygen reduction reaction, *Inside Chem.* 5 (2019) 2865–2878.
- [197] I.D. Young, M. Ibrahim, R. Chatterjee, S. Gul, F.D. Fuller, S. Koroidov, A. S. Brewster, R. Tran, R. Alonso-Mori, T. Kroll, T. Michels-Clark, H. Laksmono, R. G. Sierra, C.A. Stan, R. Hussein, M. Zhang, L. Douthit, M. Kubin, C. de Lichtenberg, P. Long Vo, H. Nilsson, M.H. Cheah, D. Shevela, C. Saracini, M. A. Bean, I. Seuffert, D. Sokaras, T.-C. Weng, E. Pastor, C. Weninger, T. Fransson, L. Lassalle, P. Braeuer, P. Aller, P.T. Docker, B. Andi, A.M. Orville, J.M. Glowina, S. Nelson, M. Sikorski, D. Zhu, M.S. Hunter, T.J. Lane, A. Aquila, J.E. Koglin, J. Robinson, M. Liang, S. Boutet, A.Y. Lyubimov, M. Uervirojanaengkoorn, N. Moriarty, D. Liebschner, P.V. Afonine, D.G. Waterman, G. Evans, P. Wernet, H. Dobke, W.I. Weis, A.T. Brunger, P.H. Zwart, P.D. Adams, A. Zouni, J. Messinger, U. Bergmann, N.K. Sauter, J. Kern, V.K. Yachandra, J. Yano, Structure of photosystem II and substrate binding at room temperature, *Nature* 540 (2016) 453–457.
- [198] S. Gong, C. Wang, P. Jiang, L. Hu, H. Lei, Q. Chen, Designing highly efficient dual-metal single-atom electrocatalysts for the oxygen reduction reaction inspired by biological enzyme systems, *J. Mater. Chem. A* 6 (2018) 13254–13262.
- [199] G. Zhang, Y. Jia, C. Zhang, X. Xiong, K. Sun, R. Chen, W. Chen, Y. Kuang, L. Zheng, H. Tang, W. Liu, J. Liu, X. Sun, W.-F. Lin, H. Dai, A general route via formamide condensation to prepare atomically dispersed metal–nitrogen–carbon electrocatalysts for energy technologies, *Energy Environ. Sci.* 12 (2019) 1317–1325.
- [200] C. Wu, X. Zhang, Z. Xia, M. Shu, H. Li, X. Xu, R. Si, A.I. Rykov, J. Wang, S. Yu, S. Wang, G. Sun, Insight into the role of Ni–Fe dual sites in the oxygen evolution reaction based on atomically metal-doped polymeric carbon nitride, *J. Mater. Chem. A* 7 (2019) 14001–14010.
- [201] X. Zhao, X. Liu, B. Huang, P. Wang, Y. Pei, Hydroxyl group modification improves the electrocatalytic ORR and OER activity of graphene supported single and bi-metal atomic catalysts (Ni, Co, and Fe), *J. Mater. Chem. A* 7 (2019) 24583–24593.
- [202] J. Chen, H. Li, C. Fan, Q. Meng, Y. Tang, X. Qiu, G. Fu, T. Ma, Dual single-atomic Ni-N(4)and Fe-N(4)Sites constructing Janus hollow graphene for selective oxygen electrocatalysis, *Adv. Mater.* 32 (2020) 2003134.
- [203] S. Sarkar, A. Biswas, T. Purkait, M. Das, N. Kamboj, R.S. Dey, Unravelling the role of Fe–Mn binary active sites electrocatalyst for efficient oxygen reduction reaction and rechargeable Zn-air batteries, *Inorg. Chem.* 59 (2020) 5194–5205.
- [204] C. Du, Y. Gao, H. Chen, P. Li, S. Zhu, J. Wang, Q. He, W. Chen, A Cu and Fe dual-atom nanzyme mimicking cytochrome c oxidase to boost the oxygen reduction reaction, *J. Mater. Chem. A* 8 (2020) 16994–17001.
- [205] X. Wang, S. Qiu, J. Feng, Y. Tong, F. Zhou, Q. Li, L. Song, S. Chen, P. Su, S. Ye, F. Hou, S.X. Dou, H.K. Liu, G.Q. Lu, C. Sun, J. Liu, J. Liang, K.-H. Wu, Confined Fe–Cu clusters as sub-nanometer reactors for efficiently regulating the electrochemical nitrogen reduction reaction, *Adv. Mater.* 32 (2020) 2004382.
- [206] Y. Zhou, E. Song, W. Chen, C.U. Segre, J. Zhou, Y.-C. Lin, C. Zhu, R. Ma, P. Liu, S. Chu, T. Thomas, M. Yang, Q. Liu, K. Suenaga, Z. Liu, J. Liu, J. Wang, Dual-metal interbonding as the chemical facilitator for single-atom dispersions, *Adv. Mater.* 32 (2020) 2003484.
- [207] H. Li, Z. Zhao, Q. Cai, L. Yin, J. Zhao, Nitrogen electroreduction performance of transition metal dimers embedded into N-doped graphene: a theoretical prediction, *J. Mater. Chem. A* 8 (2020) 4533–4543.
- [208] Z. Li, H. He, H. Cao, S. Sun, W. Diao, D. Gao, P. Lu, S. Zhang, Z. Guo, M. Li, R. Liu, D. Ren, C. Liu, Y. Zhang, Z. Yang, J. Jiang, G. Zhang, Atomic Co/Ni dual sites and Co/Ni alloy nanoparticles in N-doped porous Janus-like carbon frameworks for bifunctional oxygen electrocatalysis, *Appl. Catal., B* 240 (2019) 112–121.

- [209] H. Yan, Y. Lin, H. Wu, W. Zhang, Z. Sun, H. Cheng, W. Liu, C. Wang, J. Li, X. Huang, T. Yao, J. Yang, S. Wei, J. Lu, Bottom-up precise synthesis of stable platinum dimers on graphene, *Nat. Commun.* 8 (2017) 1070.
- [210] Y. Pan, S. Liu, K. Sun, X. Chen, B. Wang, K. Wu, X. Cao, W.-C. Cheong, R. Shen, A. Han, Z. Chen, L. Zheng, J. Luo, Y. Lin, Y. Liu, D. Wang, Q. Peng, Q. Zhang, C. Chen, Y. Li, A bimetallic Zn/Fe polyphthalocyanine-derived single-atom Fe-N<sub>4</sub> catalytic site: A superior trifunctional catalyst for overall water splitting and Zn-air batteries, *Angew. Chem. Int. Ed.* 57 (2018) 8614–8618.
- [211] L. Bai, Z. Duan, X. Wen, R. Si, Q. Zhang, J. Guan, Highly dispersed ruthenium-based multifunctional electrocatalyst, *ACS Catal.* (2019) 9897–9904.
- [212] B. Lu, L. Guo, F. Wu, Y. Peng, J.E. Lu, T.J. Smart, N. Wang, Y.Z. Finfrock, D. Morris, P. Zhang, N. Li, P. Gao, Y. Ping, S. Chen, Ruthenium atomically dispersed in carbon outperforms platinum toward hydrogen evolution in alkaline media, *Nat. Commun.* 10 (2019) 631.
- [213] W. Chen, J. Pei, C.T. He, J. Wan, H. Ren, Y. Zhu, Y. Wang, J. Dong, S. Tian, W. C. Cheong, S. Lu, L. Zheng, X. Zheng, W. Yan, Z. Zhuang, C. Chen, Q. Peng, D. Wang, Y. Li, Rational design of single molybdenum atoms anchored on N-doped carbon for effective hydrogen evolution reaction, *Angew. Chem. Int. Ed. Engl.* 56 (2017) 16086–16090.
- [214] W. Chen, J. Pei, C.T. He, J. Wan, H. Ren, Y. Wang, J. Dong, K. Wu, W.C. Cheong, J. Mao, X. Zheng, W. Yan, Z. Zhuang, C. Chen, Q. Peng, D. Wang, Y. Li, Single tungsten atoms supported on MOF-derived N-doped carbon for robust electrochemical hydrogen evolution, *Adv. Mater.* 30 (2018), e1800396.
- [215] H. Wei, K. Huang, D. Wang, R. Zhang, B. Ge, J. Ma, B. Wen, S. Zhang, Q. Li, M. Lei, C. Zhang, J. Irawan, L.-M. Liu, H. Wu, Iced photochemical reduction to synthesize atomically dispersed metals by suppressing nanocrystal growth, *Nat. Commun.* 8 (2017).
- [216] J. Zhang, M. Zhang, Y. Zeng, J. Chen, L. Qiu, H. Zhou, C. Sun, Y. Yu, C. Zhu, Z. Zhu, Single Fe atom on hierarchically porous S, N-codoped nanocarbon derived from porphyrin enable boosted oxygen catalysis for rechargeable Zn-air batteries, *Small* 15 (2019) 1900307.
- [217] S. Dilpazir, H. He, Z. Li, M. Wang, P. Lu, R. Liu, Z. Xie, D. Gao, G. Zhang, Cobalt single atoms immobilized N-doped carbon nanotubes for enhanced bifunctional catalysis toward oxygen reduction and oxygen evolution reactions, *ACS Appl. Energy Mater.* 1 (2018) 3283–3291.
- [218] L. Liu, H. Su, F. Tang, X. Zhao, Q. Liu, Confined organometallic Au1Nx single-site as an efficient bifunctional oxygen electrocatalyst, *Nano Energy* 46 (2018) 110–116.
- [219] N. Jia, Q. Xu, F. Zhao, H.-X. Gao, J. Song, P. Chen, Z. An, X. Chen, Y. Chen, Fe/N codoped carbon nanocages with single-atom feature as efficient oxygen reduction reaction electrocatalyst, *ACS Appl. Energy Mater.* 1 (2018) 4982–4990.
- [220] Y. Chen, Z. Li, Y. Zhu, D. Sun, X. Liu, L. Xu, Y. Tang, Atomic Fe dispersed on N-doped carbon hollow nanospheres for high-efficiency electrocatalytic oxygen reduction, *Adv. Mater.* 31 (2019) 1806312.
- [221] S. Wang, M. Qiao, Y. Wang, Q. Wang, G. Hu, X. Mamat, S. Zhang, Hierarchically ordered porous carbon with atomically dispersed FeN<sub>4</sub> for ultra-efficient oxygen reduction reaction in PEMFC, *Angew. Chem.* 59 (7) (2020) 2688–2694.
- [222] Y. Wang, M. Wang, Z. Zhang, Q. Wang, Z. Jiang, M. Lucero, X. Zhang, X. Li, M. Gu, Z. Feng, Y. Liang, Phthalocyanine precursors to construct atomically dispersed iron electrocatalysts, *ACS Catal.* 9 (2019) 6252–6261.
- [223] E. Li, F. Yang, Z. Wu, Y. Wang, M. Ruan, P. Song, W. Xing, W. Xu, A bifunctional highly efficient FeNx/C electrocatalyst, *Small* 14 (2018) 1702827.
- [224] L. Bai, C. Hou, X. Wen, J. Guan, Catalysis of oxygen reduction reaction on atomically dispersed copper- and nitrogen-codoped graphene, *ACS Appl. Energy Mater.* 2 (2019) 4755–4762.
- [225] E. Luo, H. Zhang, X. Wang, L. Gao, L. Gong, T. Zhao, Z. Jin, J. Ge, Z. Jiang, C. Liu, W. Xing, Single-atom Cr–N<sub>4</sub> sites designed for durable oxygen reduction catalysis in acid media, *Angew. Chem. Int. Ed.* 58 (2019) 12469–12475.
- [226] M. Xiao, J. Zhu, G. Li, N. Li, S. Li, Z.P. Cano, L. Ma, P. Cui, P. Xu, G. Jiang, H. Jin, S. Wang, T. Wu, J. Lu, A. Yu, D. Su, Z. Chen, A single-atom iridium heterogeneous catalyst in oxygen reduction reaction, *Angew. Chem.* 131 (2019) 9742–9747.
- [227] M. Xiao, Y. Chen, J. Zhu, H. Zhang, X. Zhao, L. Gao, X. Wang, J. Zhao, J. Ge, Z. Jiang, S. Chen, C. Liu, W. Xing, Climbing the apex of the ORR volcano plot via binuclear site construction: electronic and geometric engineering, *J. Am. Chem. Soc.* 141 (2019) 17763–17770.
- [228] R. Zhang, L. Jiao, W. Yang, G. Wan, H.-L. Jiang, Single-atom catalysts templated by metal-organic frameworks for electrochemical nitrogen reduction, *J. Mater. Chem. A* 7 (2019) 26371–26377.
- [229] Y. Wang, X. Cui, J. Zhao, G. Jia, L. Gu, Q. Zhang, L. Meng, Z. Shi, L. Zheng, C. Wang, Z. Zhang, W. Zheng, Rational design of Fe-N/C hybrid for enhanced nitrogen reduction electrocatalysis under ambient conditions in aqueous solution, *ACS Catal.* 9 (2019) 336–344.
- [230] A.S. Varela, N. RanjbarSahraie, J. Steinberg, W. Ju, H.-S. Oh, P. Strasser, Metal-doped nitrogenated carbon as an efficient catalyst for direct CO<sub>2</sub> electroreduction to CO and hydrocarbons, *Angew. Chem. Int. Ed.* 54 (2015) 10758–10762.
- [231] Z. Zhang, C. Ma, Y. Tu, R. Si, J. Wei, S. Zhang, Z. Wang, J.-F. Li, Y. Wang, D. Deng, Multiscale carbon foam confining single iron atoms for efficient electrocatalytic CO<sub>2</sub> reduction to CO, *Nano Res.* 12 (2019) 2313–2317.
- [232] J. Gu, C.-S. Hsu, L. Bai, H.M. Chen, X. Hu, Atomically dispersed Fe<sup>3+</sup> sites catalyze efficient CO<sub>2</sub> electroreduction to CO, *Science* 364 (2019) 1091–1094.
- [233] X. Qin, S. Zhu, F. Xiao, L. Zhang, M. Shao, Active sites on heterogeneous single-iron-atom electrocatalysts in CO<sub>2</sub> reduction reaction, *ACS Energy Lett.* 4 (2019) 1778–1783.
- [234] H. Zhang, J. Li, S. Xi, Y. Du, X. Hai, J. Wang, H. Xu, G. Wu, J. Zhang, J. Lu, J. Wang, A graphene-supported single-atom FeN<sub>5</sub> catalytic site for efficient electrochemical CO<sub>2</sub> reduction, *Angew. Chem. Int. Ed.* 58 (2019) 14871–14876.
- [235] Y. Pan, R. Lin, Y. Chen, S. Liu, W. Zhu, X. Cao, W. Chen, K. Wu, W.-C. Cheong, Y. Wang, L. Zheng, J. Luo, Y. Lin, Y. Liu, C. Liu, J. Li, Q. Lu, X. Chen, D. Wang, Q. Peng, C. Chen, Y. Li, Design of single-atom Co-N<sub>5</sub> catalytic site: a robust electrocatalyst for CO<sub>2</sub> reduction with nearly 100% CO selectivity and remarkable stability, *J. Am. Chem. Soc.* 140 (2018) 4218–4221.
- [236] N. Han, Y. Wang, L. Ma, J. Wen, J. Li, H. Zheng, K. Nie, X. Wang, F. Zhao, Y. Li, J. Fan, J. Zhong, T. Wu, D.J. Miller, J. Lu, S.-T. Lee, Y. Li, Supported cobalt polyphthalocyanine for high-performance electrocatalytic CO<sub>2</sub> reduction, *Inside Chem.* 3 (2017) 652–664.
- [237] Y. Wu, Z. Jiang, X. Lu, Y. Liang, H. Wang, Domino electroreduction of CO<sub>2</sub> to methanol on a molecular catalyst, *Nature* 575 (2019) 639–642.
- [238] E. Boutin, M. Wang, J.C. Lin, M. Mesnage, D. Mendoza, B. Lassalle-Kaiser, C. Hahn, T.F. Jaramillo, M. Robert, Aqueous electrochemical reduction of carbon dioxide and carbon monoxide into methanol with cobalt phthalocyanine, *Angew. Chem. Int. Ed.* 58 (2019) 16172–16176.
- [239] P. Su, K. Iwase, T. Harada, K. Kamiya, S. Nakanishi, Covalent triazine framework modified with coordinatively-unsaturated Co or Ni atoms for CO<sub>2</sub> electrochemical reduction, *Chem. Sci.* 9 (2018) 3941–3947.
- [240] K. Jiang, S. Siahrostami, T. Zheng, Y. Hu, S. Hwang, E. Stavitski, Y. Peng, J. Dynes, M. Gangisetty, D. Su, K. Attenkofer, H. Wang, Isolated Ni single atoms in graphene nanosheets for high-performance CO<sub>2</sub> reduction, *Energy Environ. Sci.* 11 (2018) 893–903.
- [241] T. Zheng, K. Jiang, N. Ta, Y. Hu, J. Zeng, J. Liu, H. Wang, Large-Scale and highly selective CO<sub>2</sub> electrocatalytic reduction on nickel single-atom catalyst, *Joule* 3 (2019) 265–278.
- [242] W. Zheng, J. Yang, H. Chen, Y. Hou, Q. Wang, M. Gu, F. He, Y. Xia, Z. Xia, Z. Li, B. Yang, L. Lei, C. Yuan, Q. He, M. Qiu, X. Feng, Atomically defined undercoordinated active sites for highly efficient CO<sub>2</sub> electroreduction, *Adv. Funct. Mater.* 30 (2020) 1907658.
- [243] H. Yang, Y. Wu, G. Li, Q. Lin, Q. Hu, Q. Zhang, J. Liu, C. He, Scalable production of efficient single-atom copper decorated carbon membranes for CO<sub>2</sub> electroreduction to methanol, *J. Am. Chem. Soc.* 141 (2019) 12717–12723.